Department of Electrical and Computer Engineering

A Study into the Design of Steerable Microphones Arrays

Lai Chiong Ching

This thesis is presented for the Degree of

Doctor of Philosophy

of

Curtin University

December 2012

Declaration

To the best of my knowledge and belief this thesis contains no material previously published by any other person except where due acknowledgment has been made.

This thesis contains no material which has been accepted for the award of any other degree or diploma in any university.

Signature : .....

Date : .....

Abstract

Array signal processing techniques, which offer both spatial and frequency selective signal processing, have been found to outperform single channel signal processing in most commercial applications. Array signal processing captures the spatial information of the received signal, which can be useful in acoustic source localisation or rejecting signals based on their spatial locations.

The research presented in this thesis covers the designs of steerable broadband beamformers. The discussion starts with 2-dimensional[1] beamformer design, where the aim is to achieve beamformers that can be steered around the azimuth plane while maintaining their frequency invariant response as well as the shape of their spatial main-beam. A viable beamformer structure that allows these desired characteristics is the Farrow filter structure. It consists of a bank of finite impulse response filters to achieve frequency and spatial invariant response and a single real parameter to steer the main beam.

Similar to other broadband beamformers, the proposed steerable broadband beamformer also behaves like superdirective beamformers, which are known to be very susceptible to slight perturbations, especially at low frequencies. Hence, for the proposed method to be applicable, robustness against perturbations in practical environments is required. A robust design method based on a stochastic model of the sensors' characteristics is investigated. This design method is in contrast to conventional methods which constrain the white noise gain or the absolute value of the beamformer's weights. In the proposed approach, perturbations or errors such as sensor position errors, mismatches between sensors and the non-ideal characteristics of the sensors are translated into the perturbations

[1]It is effectively 1D in spherical coordinate system, as only the azimuthal dimension is considered.

in the sensors' gain and phase, which are modelled as random variables. The stochastic mean of the perturbed design models then forms the basic of the optimum design formulation. The main feature of the proposed method is that it provides a more direct connection between the actual perturbations or errors to the design model.

The robust design model, together with the steerable design formulation, is further extended into the design of steerable robust mixed nearfield-farfield broadband beamformers. Mixed nearfield-farfield beamformers have responses that are invariant to the source radial distance (from the array). The invariant response with respect to the source distance is achieved by designing the beamformer over a range of distances covering both nearfield and farfield distances. However, due to the decreasing variation in the curvature of the wavefront as a source moves into the farfield region, it is not necessary to extend the design range far into the farfield region. This property can be exploited to design beamformers within a short finite range and yet be operable for farfield sources beyond the design range.

The final part of this thesis extends the steerable beamformer design to 3-dimension[2] using spherical arrays. The designs are formulated under the spherical harmonic framework. The existing spherical harmonic beamformer (also known as modal beamformer) structures are modified by moving the filtering block towards the sensor end. This allows the sensors to be placed flexibly on a spherical array housing as well as reduces the number of sensors required. Other properties, such as computational complexity, of the proposed modal beamformers due to such modification are also investigated and compared to the existing designs.

[2]It is effectively 2D in spherical coordinate system, as only the azimuthal and elevation dimensions are considered.

Acknowledgment

First of all, I would like to express my deepest gratitude to both my supervisors Professor Sven Nordholm and Dr. Yee Hong Leung for their continuous supervision, guidance and support throughout my research. They have generously shared their technical expertise and inspires new ideas with me which are essential towards the success of this thesis. They have also provided me a great employment opportunity as a research assistant to work alongside them. This greatly enhance my research experience as well as my expertise in the research field. Apart from technical supervision, they have also supported me relentlessly during my PhD studies. Their patience in helping me to develop the required research and technical writing skills is deeply appreciated.

Sincere gratitude is also due to postgraduates colleagues and friends for the frequent discussions that keep both my research environment and spirit lively. This tremendously adds fun and joy into my research process, and at the same time, encourages and inspires new ideas in my research.

I would like to convey my gratitude towards my mum (Kho Pei Ying), my dad (Lai Eng Hui) and sister (Lai Kim Fong) for their unrelenting supports and encouragements to keep pushing me on my PhD studies without quitting. Their unending love and cheering have made the completion of this PhD thesis a reality.

Special thanks to my friend John Tsai Tze Hui for lending his ears, either voluntarily or by force, for my complaints and stresses in my research. We shared the same hobbies and always have fantastic nonsensical talks. He would try to make me have some rest from my research, after which I can resume my research afresh.

Publications

This thesis is supported by the following publications.

1. C. C. Lai, S. Nordholm, and Y. H. Leung, "Design of Steerable Spherical Broadband Beamformers with Flexible Sensor Configurations," accepted for publication in *IEEE Trans. Audio, Speech, Language Process.*

2. C. C. Lai, S. Nordholm, and Y. H. Leung, "Design of robust steerable broadband beamformers incorporating microphone gain and phase error characteristics," in *Proc. IEEE International Conference Acoustics, Speech, and Signal Processing*, Prague, 22-27 May 2011.

3. C. C. Lai, S. Nordholm, and Y. H. Leung, "Design of robust steerable broadband beamformers with spiral arrays and the farrow filter structure," in *Proceedings International Workshop Acoustics Echo and Noise Control*, Tel Aviv, Israel, 30 Aug-2 Sep 2010.

Acronyms

1D	one dimensional
2D	two dimensional
3D	three dimensional
DI	directivity index
FIR	finite impulse response
LS	least squares
PDF	probability density function
SBBF	steerable broadband beamformer
SVD	singular value decomposition
TLS	total least squares
WNG	white noise gain

Contents

List of Figures

List of Tables

Chapter 1

Introduction

1.1 Motivation

As technology continues to advance, people are becoming more and more reliant on machines for technological solutions to uplift their quality of life and security [1–5]. Examples include hands-free in-vehicles communication systems, conference telephony systems and automatic speech recording for conferences. In such systems, the ultimate aim is to allow the user to be completely free from wearing or holding any part of the communication equipment in order to use them, and yet have a signal reception quality similar to that as if the microphone is close to the user's mouth such as in traditional systems. The main challenge in these situations is that such signal acquisition need to be done without constraining the movement of the user. This leads to time-varying signal models due to the dynamics of the user as the signal source. Furthermore, as the distance between the user and the microphones increases, the ratio between the speech strength and the strength of the background noise and other interferences decreases, causing additional challenges to the problem.

In addition to improved reception quality of the acoustic signal of interest, another challenge is to have location based selectivity in the aforementioned applications. The idea is that the system is required to respond only to the signal of interest originating from some active region, thus allowing different set of processing algorithms to be performed on signals originating from other regions, if

necessary. As an example, a voice command acquisition system in a smart television may have an active area only at the front of the television, where viewers normally sit. This can prevent any false voice command being issued from non-viewers at the sides and back of the television set.

Countless speech enhancement techniques had been proposed over the years to solve these problems. Single channel approaches include spectral suppression techniques [6, 7] and Wiener filtering techniques [8–10], both of which may require noise spectrum estimation and tracking such as in [11–13]. Although these single channel approaches are simple and cost effective in practice, their signal-to-noise improvement is limited. More complex methods such as multi-channel blind signal separation (BSS) has been shown to provide significant improvement on the signal-to-noise ratio [14–16]. Nevertheless, all these techniques do not allow for location based selectivity in the sense that they cannot pinpoint to a particular active region and only operate on the signal of interest originating from that region.

A viable solution to the above problems is beamforming, which provides spatially selective signal processing capabilities. Beamforming is an array signal processing technique where received signals, which are sampled both temporally and spatially at several sensors, are processed at the same time [17, 18]. Due to the spatial sampling of the received signals, the sampled data contains the spatial information regarding the received signals, in addition to their temporal information. Hence, spatial-temporal selective signal processings are possible. In this context, a pass region or main-beam is normally placed at a particular direction (or active region) in order to acquire the speech signal originating from that direction while rejecting unwanted signals coming from other directions, thus effectively provides spatially dependent characteristics (see Fig. 1.1). In addition, the main-beam of the beamformer can be made steerable, either manually or automatically using source tracking algorithms to cater for audio surveillance and conference recording applications mentioned above [19–25]. Moreover, beamforming techniques can be integrated to work side by side with other complex multi-channel algorithms such as distant speech recognition, speech separation, speaker tracking and localisation in order to further improve their performances

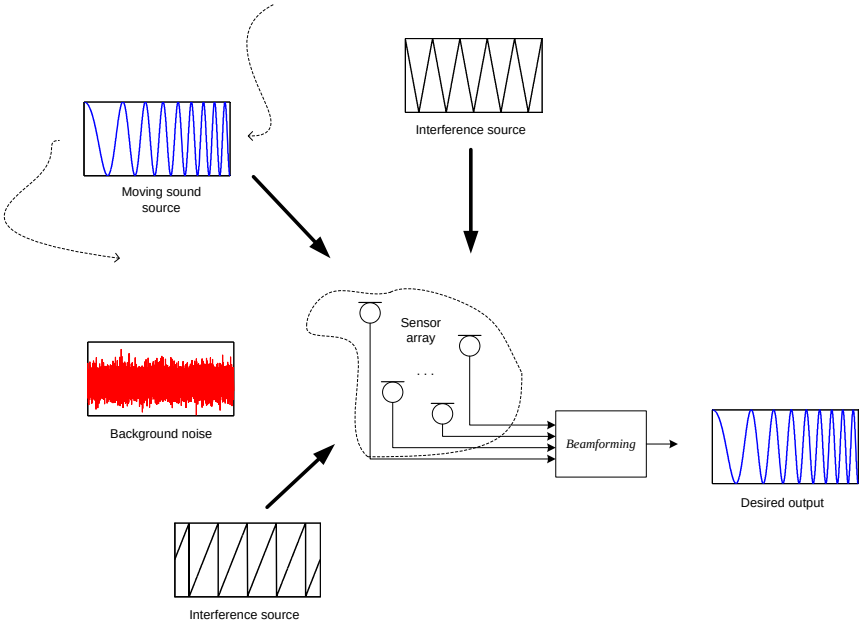

Figure 1.1: General steerable beamformer system.

[26].

Essentially, the aim of this thesis is on the design of broadband beamformers with a simple steering mechanism. The steering mechanism should allow the main-beam of the beamformers to be steered to any direction in a straightforward manner without needing to redesign the beamformers. In addition, the simple steering mechanism should also accommodate for seamless integration with other systems, such as source tracking system (which is beyond the scope of this thesis) for extended functionalities. Apart from this steering capability, the secondary aim of this thesis is to design beamformers that are robust against practical imperfections in order for them to be applicable in practical environments.

1.2 Objectives

The objectives of this thesis are to investigate and design broadband beamformers that can be steered electronically and are robust against perturbations. Ideally the resulting beamformers should have unity magnitude response with constant phase delay in the look direction (pass region) and zero response in the stop region to completely suppress signals coming from other directions. In other words, the beamformers should have the following traits:

- electronically steerable main-beam, without requiring any mechanical movement of the physical array,
- simple steering mechanism of the main-beam without needing to redesign the beamformer weights for different steering directions,
- steering invariant spatial-temporal response, i.e. only the direction of the main-beam changes with the steering direction. Other properties such as main-beam width and sidelobes remain invariant for different steering directions,
- frequency invariant response throughout the frequency range of interest and for all steering directions,
- robust to errors and perturbation, such as sensor mismatch and sensor position errors, and
- ability to operate for both nearfield and farfield source models.

1.3 Scope

The scope of the beamformer designs in this thesis is limited to a single main-beam designs, which correspond to applications for reception of a single broadband signal source. The source considered is a point source with its wavefront propagating radially outwards. The designs are only focused on data-independent or non-adaptive beamformers. The propagation medium of the sound wave is assumed to be homogenous, isotropic, non-dispersive and time-invariant with discrete sensors placed in space. No reverberation is considered in the signal environment since reverberation is a huge research topic by itself. Comprehensive studies on reverberation can be found in [27–29]. For non-robust designs, both azimuth-only and azimuth-elevation beamformer designs are presented. However, the discussion on robust designs are limited to azimuth-only beamformers.

1.4 Contribution of the thesis

The original contributions of this dissertation are as follows.

- propsosed a spiral arm array geometry, including the analysis on selecting its array parameters,
- introduced a beamformer design model that includes both multiplicative and additive complex errors for robust beamformer designs,
- proposed the design of steerable robust mixed nearfield-farfield beamformer, and
- proposed an azimuth-elevation beamformer design that utilises steering mechanism from spherical beamforming technique while allowing for arbitrary sensor placements.

1.5 Overview of the thesis

The primary aim of this thesis is to design steerable broadband beamformers (SBBFs) that are robust against perturbations and mismatches caused by the differences between the ideal model and the practical setup.

Preliminary studies and background information relating to beamformer designs are presented in Chapter 2. These include discussions on the spatial distribution of sensors, source models, beamformer structures as well as important design considerations that can affect the performance of a beamformer.

In Chapter 3, the discussion starts with an investigation of a spiral arm array pattern which possesses some desirable characteristics for SBBFs. The selection of the array parameters is also investigated in order to exploit the features of the array geometry which can further improve the performance of a SBBF. This is followed by a discussion on different non-robust design formulations for SBBFs.

These design formulations are extended in Chapter 4 to include a stochastic error model in the array response for robustness. This stochastic model provides a better representation of practical perturbations which are normally only known

probabilistically. The stochastic error model is formulated as multiplicative error, additive error and both, where each formulation fits into different types of perturbations in practical environments.

In Chapter 5, the design formulation is further extended to design steerable robust mixed nearfield-farfield beamformers, which have invariant response over a wide range of source radial distance, covering both nearfield and farfield distances. The extension follows closely from the design formulation in Chapter 3 and can be seamlessly incorporated into the robust design formulations discussed in Chapter 4. Apart from achieving operability for both nearfield and farfield sources, the steerability and robustness properties in the existing formulations are maintained.

Chapter 6 covers the design of azimuth-elevation spherical SBBFs. The design is achieved by implementing the steering capability of spherical harmonic beamforming into the conventional filter-and-sum beamformers. This design method admits arbitrary sensor configurations and yet achieves steering and frequency invariant responses. The ability to admit arbitrary sensor configuration stems from the conventional filter-and-sum design approach where there is no assumption on the orthonormality of the sensor positions as in the existing spherical harmonic beamforming. In contrast, the steering invariant response property comes from spherical harmonic beamforming where steering is done by means of modulation. In addition to these, the proposed method requires less sensors, and yet yields performance similar to the existing spherical harmonic beamformers.

Chapter 2

Background

2.1 Introduction

Beamforming is a spatial filtering technique to receive a signal radiating from a certain direction while attenuating signals from other directions. One of the main purposes of beamforming is to separate a desired signal from interference signals originating from separate, non-overlapping spatial locations, but may occupy the same spectral bands.

The basic concept behind beamforming is the relative difference in the phase shift and gain attenuation of the impinging wavefronts as seen by each sensor element. This difference contains useful spatial information about the received signals and their propagation medium, which can be used to design beamformers with desired responses. In the simplest sense, beamforming is similar to temporal filtering except that filtering is done on spatially sampled data (as opposed to temporally sampled data). For broadband beamforming, a joint spatial-temporal filtering is employed instead, in order to provide both spatial and spectral selectivity at the same time.

The design of beamformers involves a number of design considerations such as the choice of spatial sampling scheme, which is related to the array geometry, signal propagation model as well as the beamformer structure. There is no single generic design formulation or model that has the best performance under all circumstances. Usually the design model needs to be changed to suit its target

applications.

This chapter reviews the preliminaries design considerations required for broadband beamformer designs. It only provides brief and concise background information and further details can be found in the references cited. The discussion starts off by introducing the different categories of sensor array geometries that can be used for beamforming, including the sensor placement criteria to avoid spatial aliasing. This is followed by the analysis of two main signal models, namely nearfield and farfield signal models, together with their merits and drawbacks. A number of existing beamformer structures that can be extended for designing steerable broadband beamformers are also discussed.

2.2 Sensor array

2.2.1 Array geometries

The placement of sensors in space to form a sensor array is entirely a design decision. The sensors can either be placed arbitrarily or follow a known geometry shape. Regardless, the choice of array geometry is important in beamformer designs as it plays a major role in the performance of the beamformers. This is because certain array geometry has advantages and limitations over the others [30, 31]. For example, a uniform linear array (see Fig. 2.1) has the best spatial resolution either at broadside or endfire, depending on the target application, whereas a uniform circular array (see Fig. 2.2a) has a uniform spatial resolution for the whole azimuth range.

In general, array geometries can be categorised into three main categories, namely one dimensional (1D), two dimensional (2D) and three dimensional (3D) arrays. 1D arrays comprise of placing sensors in a line as shown in Fig. 2.1. Its variants include uniform or non-uniform spaced array element, and broadside or endfire configuration type. 2D arrays consist of placing sensors on a plane, which can either be along the perimeter of or fill up an enclosed area. Some commonly used 2D arrays include planar, circular and multi-ring concentric circular array patterns as shown in Fig. 2.2. In the case of 3D arrays, the sensors can be

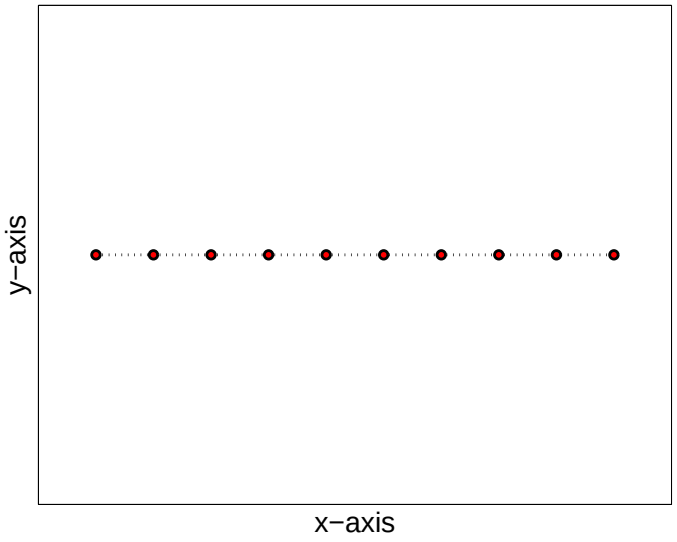

Figure 2.1: Example of 1D array pattern.

placed on the surface of 3D solids, or they can be placed on frames to fill up the volume of 3D solids, such as cylinder or sphere (see Fig. 2.3). The choice of array patterns depends heavily on the target applications.

2.2.2 Spatial aliasing

In beamforming or spatial filtering, sensors placed in space play the role of spatially sampling the received wave. Hence, similar to Nyquist rate in spectral sampling, the smallest distance between adjacent sensors must at most equal to half the smallest wavelength in order to avoid spatial aliasing, i.e. [17]

$$d_{min} \leq \frac{\lambda_{min}}{2} \tag{2.1}$$

where d_{min} is the minimum distance between adjacent sensors and λ_{min} is the smallest wavelength, which corresponds to the highest frequency component in a broadband signal. The wavelength and the frequency of the wave is related by

$$c = f\lambda \tag{2.2}$$

where the constant c is the speed of the wave in the propagating medium (e.g. $c = 343\text{ms}^{-1}$ in air) and f is the frequency of the wave. As an example, consider an endfire linear array with 6 elements and inter-element spacing of 4cm. The highest signal frequency that it can resolve before spatial aliasing occurs is

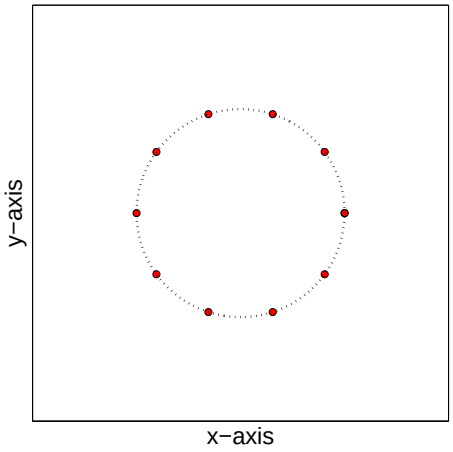

(a) Circular array.

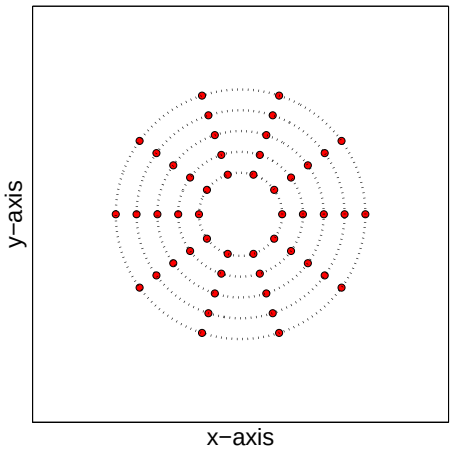

(b) Concentric circular array.

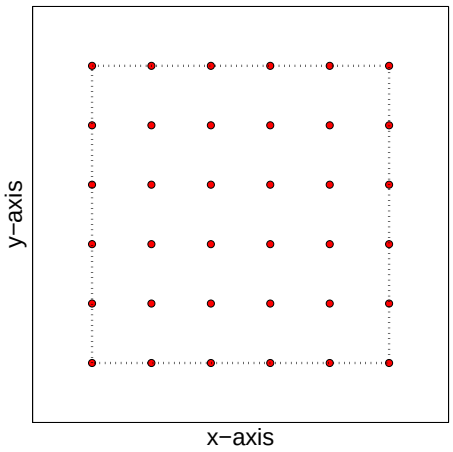

(c) Rectangular planar array.

Figure 2.2: Examples of 2D array patterns.

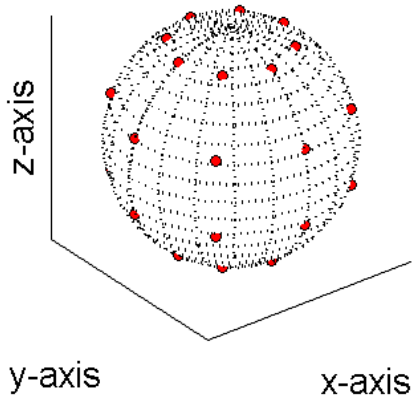

(a) Spherical surface array.

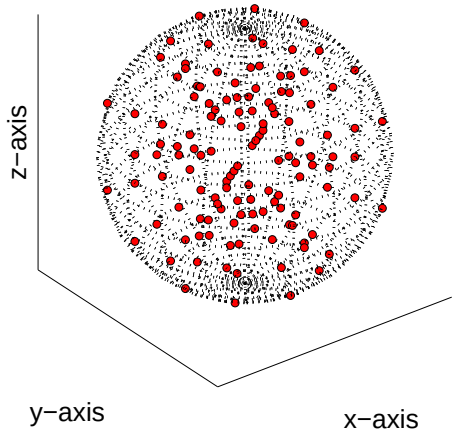

(b) Spherical volume array.

Figure 2.3: Examples of 3D array patterns.

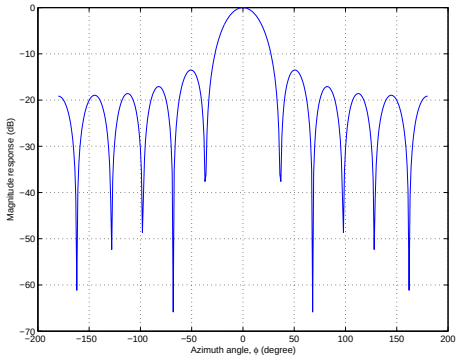

(a) No spatial aliasing.

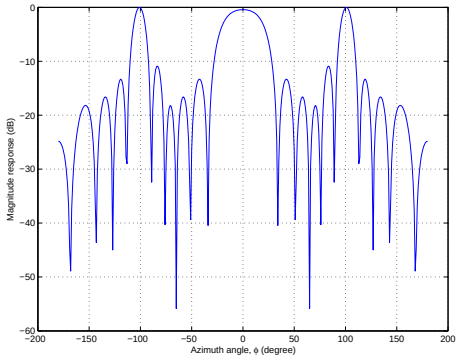

(b) Spatial aliasing occurs.

Figure 2.4: Endfire linear array with inter-element spacing of 4cm.

$f_{max} \approx 4.3$kHz. The beampatterns of a weight-and-sum beamformer designed for frequency $f = 3$kHz and 7kHz using this array are shown in Fig. 2.4. The figure clearly demonstrates the occurrence of spatial aliasing when (2.1) is violated.

2.3 Source model

2.3.1 Nearfield source model

For a wave traveling in a homogeneous, isotropic, non-dispersive and time invariant medium (see Fig. 2.5), the signal received at a sensor (or receiver) is phase delayed and attenuated by its propagation response (also known as array element response or Green function) which is given by [32]

$$a_{near}\left(\mathbf{r}_k, \omega, \mathbf{r}_s\right) = \frac{1}{4\pi \left\|\mathbf{r}_k - \mathbf{r}_s\right\|} \exp\left(-j\frac{\omega}{c}\left\|\mathbf{r}_k - \mathbf{r}_s\right\|\right) \tag{2.3}$$

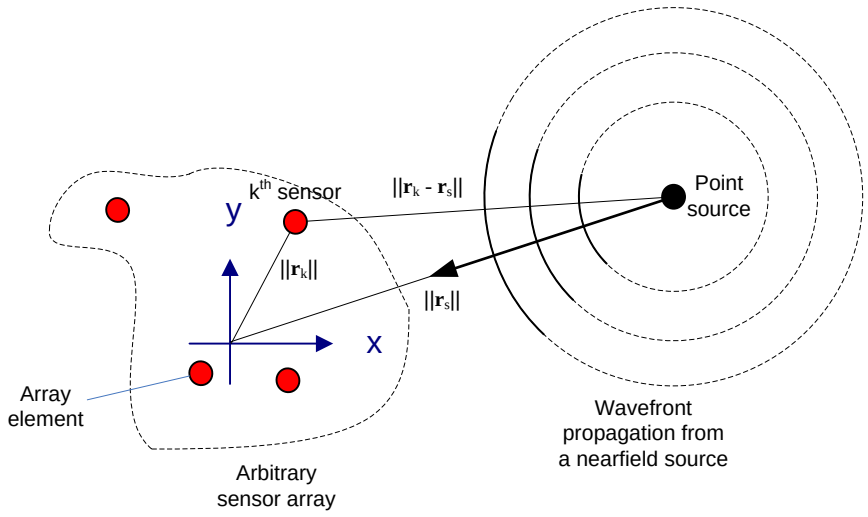

Figure 2.5: Nearfield source model.

where ω is the frequency of the sound, $\mathbf{r}_s$ is the position of the source, $\mathbf{r}_k$ is the position of the k^{th} sensor, and $\|\cdot\|$ denotes Cartesian distance. The attenuation in (2.3) is due to the decay of signal amplitude as it propagates outwards from its source. The constant 4π can be dropped for convenience since only the relative gain and phase difference between the sensors are important. Suppose that $S_0(\omega)$ is the original source signal, using (2.3), the signal as received by the k^{th} sensor is

$$X_k(\omega) = a_{near}(\mathbf{r}_k, \omega, \mathbf{r}_s) S_0(\omega). \tag{2.4}$$

A more elaborate expression which includes a general propagation medium is also possible by solving the wave equations [33].

2.3.2 Farfield source model

Although (2.3) gives a generic frequency response from an arbitrarily located signal source to an arbitrarily located sensor, the non-linear Cartesian distance in the equation may complicate beamformer designs. A simplified source model can be obtained by considering the source to be at infinite distance from the sensor array, i.e. $\|\mathbf{r}_s\| \to \infty$. The reason for this is that when the source is far enough from the sensor array, the wavefront impinging on the array becomes planar (as opposed to curved), which can simplify the propagation model. However, in this

farfield source model, a reference point is required and is normally taken as the origin of the coordinate system or the center of mass of the sensor array. Suppose the origin of the coordinate system is taken to be the reference point. The array element response for the k^{th} sensor is then given by

$$a_0\left(\mathbf{r}_k, \omega, \mathbf{r}_s\right) = \frac{\|\mathbf{r}_s\|}{\|\mathbf{r}_k - \mathbf{r}_s\|} \exp\left(-j\frac{\omega}{c}\left(\|\mathbf{r}_k - \mathbf{r}_s\| - \|\mathbf{r}_s\|\right)\right). \tag{2.5}$$

Observe that as $\|\mathbf{r}_s\| \to \infty$,

$$\lim_{\|\mathbf{r}_s\|\to\infty} \frac{\|\mathbf{r}_s\|}{\|\mathbf{r}_k - \mathbf{r}_s\|} = 1 \tag{2.6}$$

and

$$\lim_{\|\mathbf{r}_s\|\to\infty} \|\mathbf{r}_k - \mathbf{r}_s\| - \|\mathbf{r}_s\| = \|\mathbf{r}_k\| \cos\left(\triangle\phi_k\right) = \mathbf{r}_k \cdot \vec{\mathbf{r}}_s \tag{2.7}$$

where $\triangle\phi_k$ is the angle between the direction to the k^{th} sensor and the source and $\vec{\mathbf{r}}_s$ is the normalised source position. Hence, the array element response for a farfield source is given by [32]

$$\begin{aligned} a_{far}\left(\mathbf{r}_k, \omega, \mathbf{r}_s\right) &= \lim_{\|\mathbf{r}_s\|\to\infty} a_0\left(\mathbf{r}_k, \omega, \mathbf{r}_s\right) \\ &= \exp\left(-j\frac{\omega}{c}\mathbf{r}_k \cdot \vec{\mathbf{r}}_s\right). \end{aligned} \tag{2.8}$$

For commonly used array geometries such as the uniform linear array and circular array (shown with their variables in Fig. 2.6), the farfield array element responses are respectively

$$a_k^{(lin)}\left(\omega, \phi_s\right) = \exp\left(-j\frac{\omega}{c}kd\cos\left(\phi_s\right)\right) \tag{2.9}$$

$$a_k^{(cir)}\left(\phi_k, \omega, \phi_s\right) = \exp\left(-j\frac{\omega r}{c}\cos\left(\phi_s - \phi_k\right)\right). \tag{2.10}$$

Although the farfield source model gives a simpler expression for the array element response (compare (2.8) with (2.3)), the model is only valid for open space environment (e.g. outdoor empty field) and not for enclosed environment, such as small rooms due to its requirement of $\|\mathbf{r}_s\| \to \infty$. However, some researchers have supported the validity of this source model at reduced range $\|\mathbf{r}_s\|$ (e.g. in medium-sized office and indoor stadium, depending on the array size). One of

the widely used quantitative lower bounds as a practical criterion for the farfield source model to be valid is [34–36]

$$r_s > \frac{2L_a^2}{\lambda} \tag{2.11}$$

where r_s is radial distance between the source and the center of mass of the array, L_a is the largest array aperture and λ is the operating signal's wavelength. This criterion is based on the acceptable quadratic phase error and its detailed discussion can be found in [37–40]. Due to the simplicity of the farfield source model, various nearfield beamforming solutions are derived from this model, such as radial transformation [32], nearfield compensation [34], and the radial reciprocity method [41].

2.4 Basic beamformer structure

2.4.1 Weight-and-sum beamformer

A beamformer structure describes how filtering can be applied to the received signal at each sensor in order to achieve a desired overall response. The simplest beamformer structure is the weight-and-sum beamformer depicted in Fig. 2.7. In this structure, a complex weight is applied to the received signal at each sensor, after which they are summed to produce a single output signal. These complex weights scale the received signals such that they are constructively summed if they come from a certain desired direction and destructively summed otherwise, thus resulting in spatial selectivity [17]. Weight-and-sum beamformer is normally used for narrowband beamforming, where the bandwidth of the signal is much smaller than its centre frequency. The output of a weight-and-sum beamformer is given by

$$Y(\omega) = \sum_{k=1}^{K} X_k(\omega) W_k \tag{2.12}$$

where $X_k(\omega)$ is the received narrowband signal and W_k is the complex weight at the k^{th} sensor.

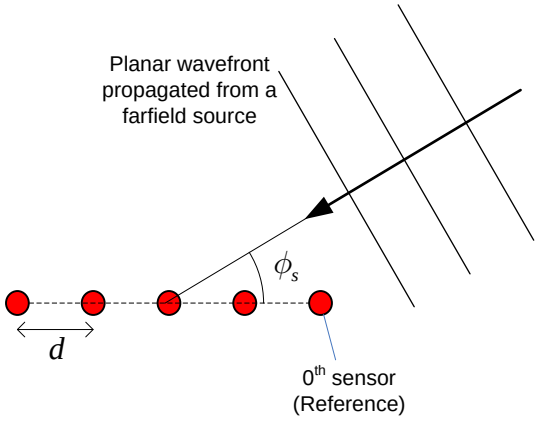

(a) Uniform linear array.

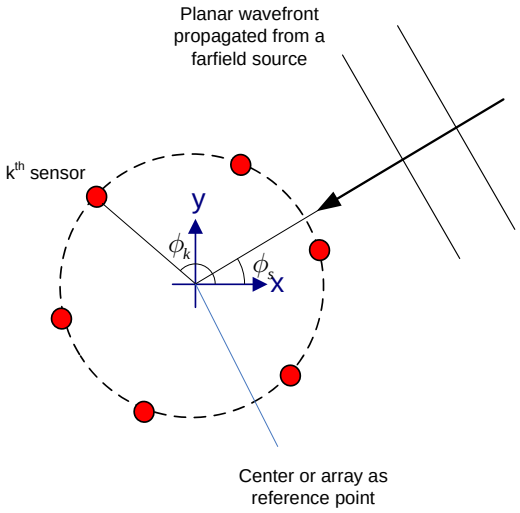

(b) Uniform circular array.

Figure 2.6: Farfield source model for uniform linear and circular arrays.

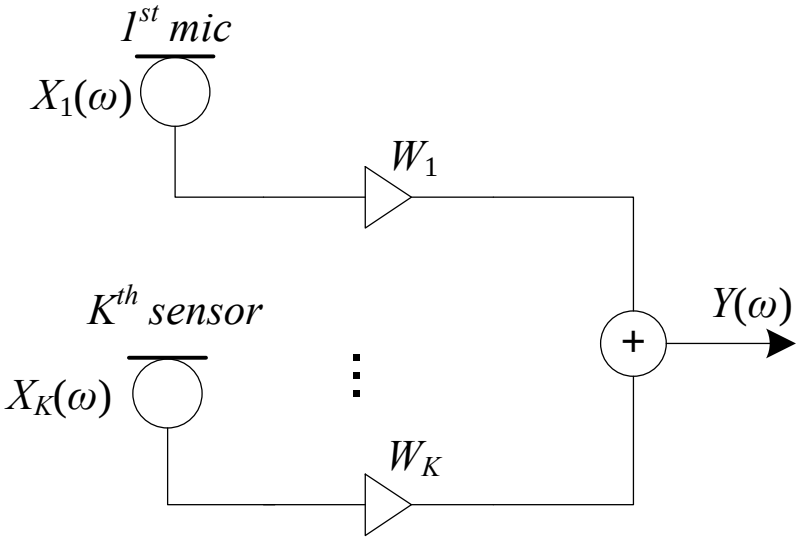

Figure 2.7: Weight-and-sum beamformer structure.

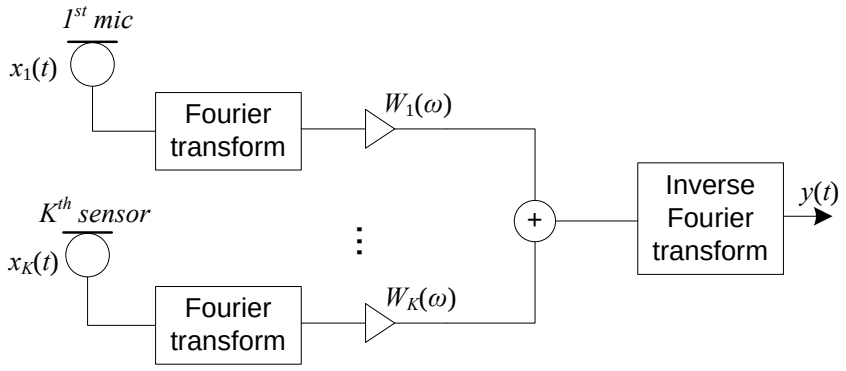

Figure 2.8: Frequency domain broadband beamformer structure.

The weight-and-sum beamformer structure can be extended to frequency domain broadband beamforming by means of Fourier transform and frequency dependent complex weights $W_k(\omega)$ (see Fig. 2.8). In such a structure, a broadband signal is decomposed into its individual frequency components and a weight-and-sum beamformer with frequency dependent complex weights is then applied to the corresponding components in order to achieve broadband beamforming. The output signal is given by

$$y(t) = F^{-1}\{Y(\omega)\} \tag{2.13}$$

where

$$Y(\omega) = \sum_{k=1}^{K} X_k(\omega) W_k(\omega), \tag{2.14}$$

$X_k(\omega) = F\{x_k(t)\}$ and $F\{\cdot\}$ is the Fourier transform.

2.4.2 Filter-and-sum beamformer

Another broadband beamformer structure that is widely used is the filter-and-sum beamformer structure depicted in Fig. 2.9. In this structure, a filter, such as the finite impulse response (FIR) filter is attached to each of the sensor for broadband filtering capability. The output signal of filter-and-sum beamformers is given by

$$y(\omega) = \sum_{k=1}^{K} w_k(t) \star x_k(t) \tag{2.15}$$

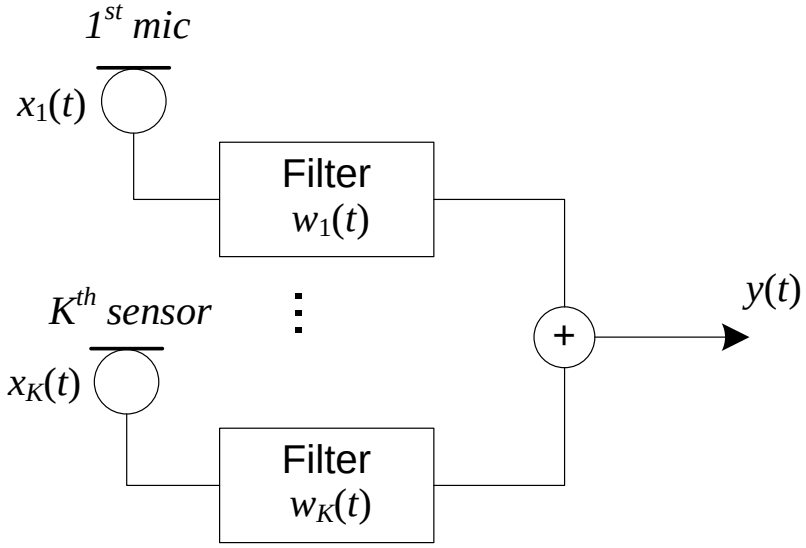

Figure 2.9: Filter-and-sum beamformer structure.

where $w_k(t)$ is the impulse response of the filter attached to the k^{th} sensor and $\star$ denotes convolution.

In general, the design problem of broadband beamformers using the filter-and-sum structure is larger and more challenging. This is because the trade-offs between conflicting requirements such as robustness, low frequency response, spatial aliasing at high frequency and array aperture size need to be systematically addressed. Furthermore, unlike the frequency domain broadband beamformer (see Fig. 2.8), its design problem cannot be broken down into smaller design problems based on the individual frequency components of the signal.

2.4.3 Modal beamformer

Another notable beamformer structure, which is scalable, is the modal beamformer structure shown in Fig. 2.10 [42, 43]. In this structure, the received signals are first decomposed into orthogonal components using orthogonal basis functions such as spherical harmonics. Filtering (either in frequency domain or through FIR filters) is then performed on these components for frequency response and beampattern shaping, before they are summed together into a single output signal.

The modal beamformer structure is normally attractive since it is computa-

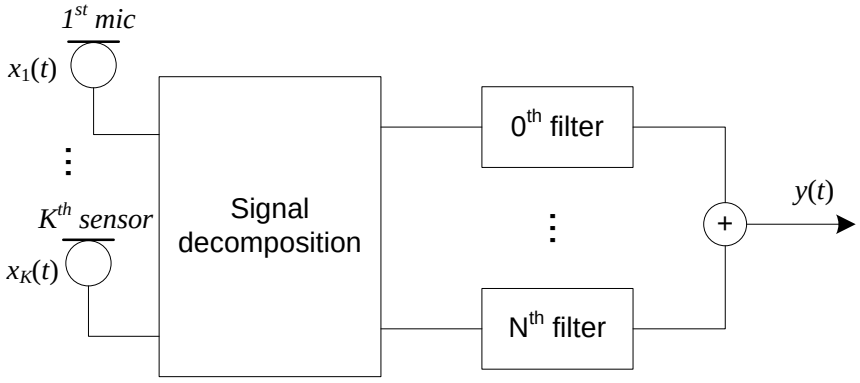

Figure 2.10: General modal beamformer structure.

tionally less complex compared to the weight-and-sum and filter-and-sum beamformer structures. Computation counts in the filtering stage is reduced when the maximum number N of orthogonal components decomposed is less than the number of sensors K, i.e. $N < K$, which is normally the case in practise.

Another attractive property of the modal beamformer structure is that mainbeam steering can be achieved simply by means of modulation [42]. The modal beamformer structure is also favourable especially when the basis functions chosen for the decomposition or transform is mathematically matched to the physical array geometry and the propagation model used, which can simplify the overall design formulation.

2.5 Conclusion

The preliminaries involved in the design formulation for beamformers (including steerable broadband beamformers) consist of carefully selecting the signal model, array geometry and beamformer structure. Within each category, different models or structures have their own merits and drawbacks. There is no single best combination that can fit perfectly for all applications. As such, in order to maximise the performance of beamformers, different combinations of array geometries and beamformer structures are matched to the target application. Even so, there may still be conflicting design decisions where careful considerations are required to optimise the trade-offs.

Chapter 3

2D Steerable Broadband Beamformer Design

3.1 Introduction

Fixed beamformers, though simple, have only a fixed response. They are limited therefore to applications where the signal source is fixed. If the signal source moves to a new position, then the fixed beamformers will need to be redesigned to cater for such a change. In contrast, SBBFs are able to steer their main-beams on-the-fly, without the need to redesign their weights. This steering capability offers dynamic beamforming which is extremely useful in applications that involve moving sources. Some examples include audio-video conferencing, hands-free communication systems, audio surveillance systems, and human-machine interface systems where the human speaker (or signal source) is likely to move around. In these cases, acoustic signal reception using fixed beamformers is not feasible and SBBFs provide a better fit since they can be steered readily to track of the moving source.

In light of these demands, SBBFs have attracted much research attention. One of the existing attempts to design SBBFs involves using a polynomial finite impulse response (FIR) filters or the Farrow structure [44] to provide non-linear mixing of the FIR filters to achieve steerability [45, 46]. Another method of achieving steerability is proposed by Parra, where the spatial-temporal depend-

ency of the broadband beamformer is separated and steering is achieved by using the Wigner rotation matrix [47]. Other methods include designing the beamformers as modal beamformers, where the received signals are first decomposed into orthogonal modes, and then, linearly combined to achieve a desired response [42]. For these modal beamformers, steerability is achieved by means of modulating the modes.

This chapter discusses the design of 2D SBBFs, which includes the design of the array geometry as well as the beamformer weights. The choice of array geometry is equally important as the design of the beamformer weights since they both have significant influence on the achievable desired response. In the formulation discussed, the Farrow structure is used to provide simple and straightforward main-beam steering.

This chapter is organised as follows. In Section 3.2, the spiral arm array geometry is discussed in details, including the selection of its parameters. This geometry is proposed as a candidate for SBBFs since it possesses some desirable properties which can be exploited for SBBFs. Section 3.3 discusses the Farrow structure used for the SBBF design, followed in Section 3.4 by its design formulation under both the weighted least squares (LS) and weighted total least squares (TLS) criteria. A number of design examples are provided in Section 3.5 together with their performances. Section 3.6 concludes the chapter.

3.2 Spiral arm array geometry

3.2.1 Characteristics and properties

In element space beamformer design, the sensor array itself, in addition to the beamformer structure (see Section 3.3), plays a major role in the beamformer's performances. Hence, the choice of array geometry and sensors placement are important and require careful consideration. Consider a spiral arm array geometry shown in Fig. 3.1, which is a variant of the spiral arm arrays in [48, 49] and the wheel array in [50]. It consists of P concentric rings, indexed by $p = 0, ..., P-1$, with sensors uniformly spaced along the circumference of each ring. The p^{th} ring

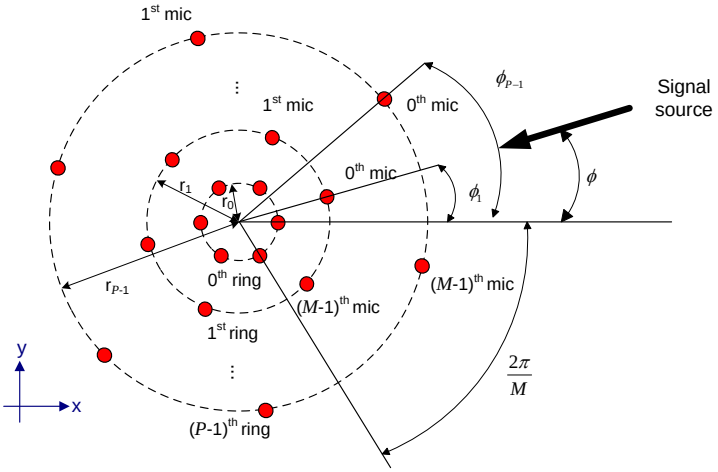

Figure 3.1: Proposed spiral arm array geometry.

is further rotated by an angle ϕ_p.

The positions (in cylindrical coordinate system) of the array elements are given by

$$\mathbf{r}_k = \left[r_p, \frac{2\pi m}{M} + \phi_p \right] \tag{3.1}$$

where $k = pM+m$, M is the number of sensors per ring indexed by $m = 0, ..., M-1$, and the centre of the array is taken as the origin of the coordinate system. The radius r_p and the rotation angle ϕ_p of the p^{th} ring are design parameters. Its array element response (with the center of array taken as the reference point) to a farfield source impinging the array from azimuth angle ϕ_s is given by

$$a\left(\mathbf{r}_k, \omega, \mathbf{r}_s\right) = \exp\left(-i \frac{\omega r_p}{c} \cos\left(\phi_s - \frac{2\pi m}{M} - \phi_p \right) \right). \tag{3.2}$$

This spiral arm array geometry possesses a few desirable characteristics that make it an attractive candidate for broadband beamforming. Firstly, its multi-ring nature allows each ring to compensate for separate frequency bands in a cooperative manner to achieve larger bandwidth for broadband beamforming [51]. Besides, since it is a 2D array, it provides full 360°coverage of the azimuthal dimension, without any ambiguity (e.g. linear array).

Secondly, having a circular symmetry means the array geometry has uniform resolution throughout the entire azimuthal dimension [30]. Therefore, there is no issue of it exhibiting biased response to a particular azimuth angle as compared to array geometry such as the rectangular or triangular array geometries. This

also ensures that the beamformer response is symmetry about its look direction. Besides, this circular symmetric property can be exploited in the design of SBBFs to provide full 360°steerability when their steerability only needs to be realised over a sector. This is done by appropriately permuting the beamformer weights (see Section 3.5).

Thirdly, each ring of the spiral arm array geometry has undergone a slight rotation (c.f. Fig. 2.2b). This rotation introduces irregularity and reduces the periodicity in its geometry, thus providing irregular spatial sampling of the received signals, which can slightly suppress spatial aliasing [50, 52]. This property can be exploited in broadband beamforming problems where the sensor array needs to be balanced between avoiding spatial aliasing for high frequency components as well as having aperture size large enough for low frequency components.

3.2.2 Parameters selection

3.2.2.1 Ring radii

For the proposed spiral arm array shown in Fig. 3.1, there are two main design parameters, namely ring radii and ring rotation angle. From Nyquist sampling theorem, the spacing between adjacent sensors must not be larger than half the wavelength of the highest operating frequency in order to avoid spatial aliasing. In contrast, the array aperture need to be sufficiently large to provide the required spatial resolution for the low frequency components. In order to satisfy these contrasting requirements, the concept of narrowband signal processing is employed, where each concentric ring from the proposed multi-ring array is designed to handle a single frequency component. Under this scheme, each ring radius is then selected to satisfy the Nyquist criterion for its corresponding operating frequency given by

$$r_p \leq \frac{c}{4f_{p,max}\sin\left(\frac{\pi}{M}\right)} \tag{3.3}$$

where $f_{p,max} \in \Omega_{pb}$ is the maximum operating frequency for the p^{th} ring, and Ω_{pb} is the spectral passband. As an example, for a spectral passband of $\Omega_{pb} = [200, 3800]$Hz and $P = 5$, one possible choice (following linear discretisation) is $f_{0,max} = 3800$Hz, $f_{1,max} = 2900$Hz, $f_{2,max} = 2000$Hz, $f_{3,max} = 1100$Hz and

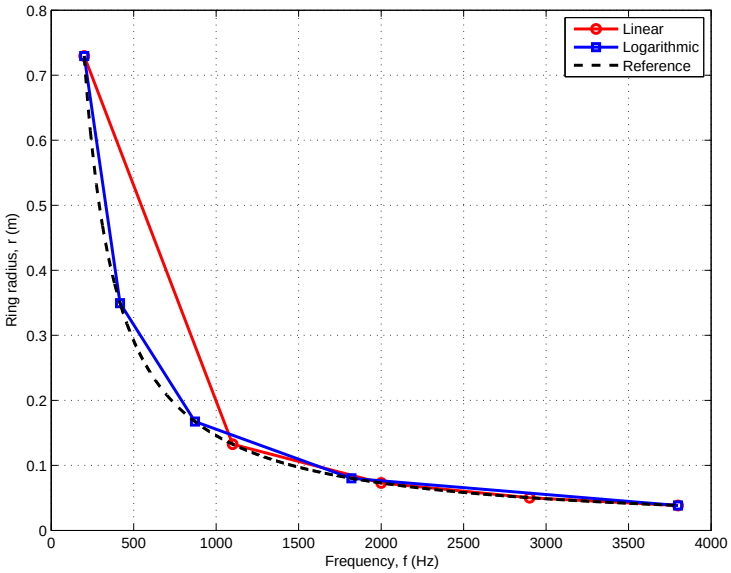

Figure 3.2: Discretisation of ring radii.

$f_{4,max} = 200$Hz.

However, with the finite number of rings covering a broadband signal, (3.3) results in the discretisation of the broadband frequency range into $P-1$ bands. Judging from (3.3), which involves an inverse relationship between r_p and f_p, the logarithmic discretisation of f_p will outperform the linear discretisation. This is because the uniform step size in linear discretisation does not provide sufficient resolution at low frequencies where the value of the function (3.3) changes more rapidly than at high frequencies. On the other hand, the logarithmic discretisation with non-uniform step size fits nicely for the changes of (3.3), both at low and high frequencies.

This observation is clearly shown in Fig. 3.2, where $f_p \in [200, 3800]$Hz is discretised into $P-1=4$ bands using both the logarithmic and linear discretisation schemes. To further highlight this observation, the beampatterns for a fixed beamformer with linear and logarithmic ring radii sampling are shown in Fig. 3.3. The beamformers are designed using the parameters in Table 3.1, with $r_p = \{0.0365, 0.0771, 0.1631, 0.3449, 0.7294\}$m for logarithmic discretisation and $r_p = \{0.0365, 0.2097, 0.3830, 0.5562, 0.7294\}$m for linear discretisation.

Table 3.1: Design parameters for fixed beamformer to illustrate different ring radii discretisation.

Parameter	**Value**
Number of rings, P	5
Number of sensors per ring, M	5
Ring rotation angle, ϕ_a	0^{o}
Sampling frequency, f_S	8 kHz
Spectral passband, Ω_{pb}	$[0.2, 3.8]$ kHz
Spectral stopband, Ω_{sb}	$[0, 0.1] \cup [3.95, 4]$ kHz
Spatial pass region, $\Phi_{pb}(\psi)$	$\lvert\phi - \psi\rvert \leq 15^{\text{o}}$
Spatial stop region, $\Phi_{sb}(\psi)$	$\lvert\phi - \psi\rvert \geq 25^{\text{o}}$
Steering angle range, Ψ	0^{o} (No steering)
Order of Farrow structure, $N-1$	0
FIR filter length, L	64
Speed of propagating wave, c	343 m/s

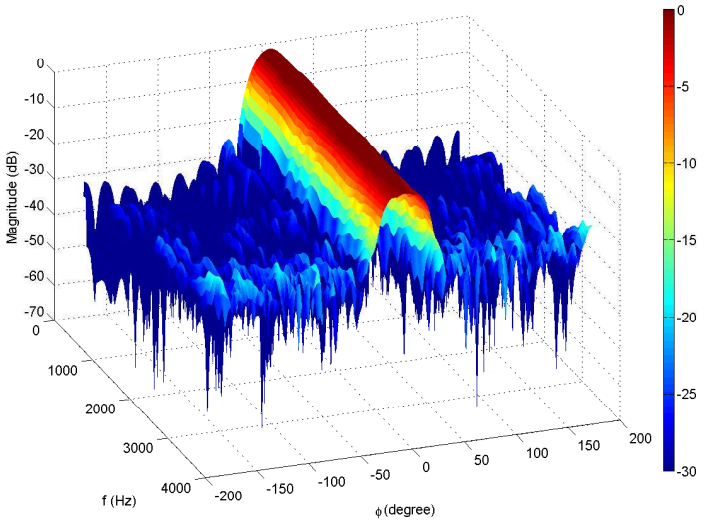

(a) Logarithmic discretisation.

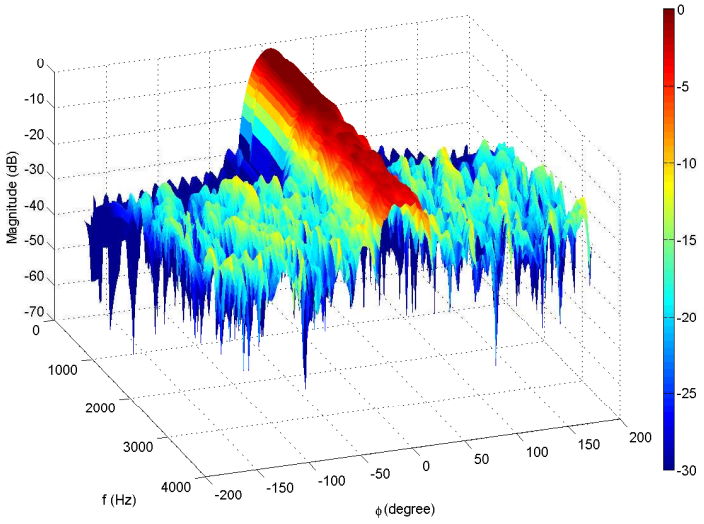

(b) Linear discretisation.

Figure 3.3: Beampatterns for fixed beamformer using logarithmic and linear discretisation of ring radii.

3.2.2.2 Ring rotation angle

Unfortunately the selection of the ring rotation angle is not as straightforward as for the ring radii. The amount of rotation for each ring can be different and independent of one another. However, if ϕ_p is a multiple of $2\pi/M$, then the spiral arm array will be similar to the array in Fig. 2.2b.

In order to simplify the selection of ϕ_p, each ring rotation is restricted to be a multiple of a scalar rotation ϕ_a, i.e.

$$\phi_p = p\phi_a. \tag{3.4}$$

Then, a simple line search algorithm can be used to find the optimal candidate for ϕ_a, which is highly dependent on the overall beamformer design formulation and specification. Fig. 3.4 shows the cost (3.33) for the LS SBBF designs in Section 3.5 with $\phi_a \in [-36°, 36°]$ for $P = 4$ and 5. Other design parameters are as given in Tables 3.2 and 3.3. From Fig. 3.4 and due to the symmetry of the spiral arm array geometry, the optimal values for $P = 4$ is $\phi_a = \pm\left(12° + {}^{180°k}/_{M}\right)$ and for $P = 5$ is $\phi_a = \pm\left(14.4° + {}^{180°k}/_{M}\right)$, where k is a non-negative integer.

Note that (3.4) is only one of many possible choices for ϕ_p and results in the proposed spiral arm array shown in Fig. 3.1. Other choices will result in different variants of spiral arm array geometries.

3.3 Beamformer structure

In the design of SBBFs, a beamformer structure having both broadband beamforming capability as well as ease of main-beam steering is desired. One structure having such characteristics is the time domain Farrow FIR filter structure shown in Fig. 3.5. The FIR filters provide broadband signal processing capability, whereas the real scalar $\tilde{\psi}$, which provide a non-linear mixing of the FIR filters, can be used for main-beam steering. The response of this beamformer structure is given by

$$B\left(\tilde{\psi}, \omega, \mathbf{r}_s\right) = \sum_{k=0}^{PM-1} a\left(\mathbf{r}_k, \omega, \mathbf{r}_s\right) \sum_{n=0}^{N-1} \tilde{\psi}^n \sum_{l=0}^{L-1} w_{p,m,n}\left(l\right) \exp\left(-i\omega T_S l\right) \tag{3.5}$$

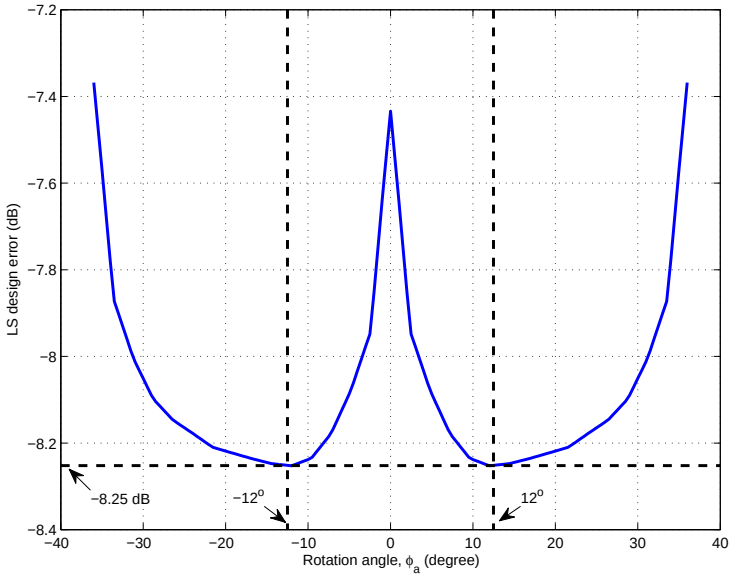

(a) $P = 4$.

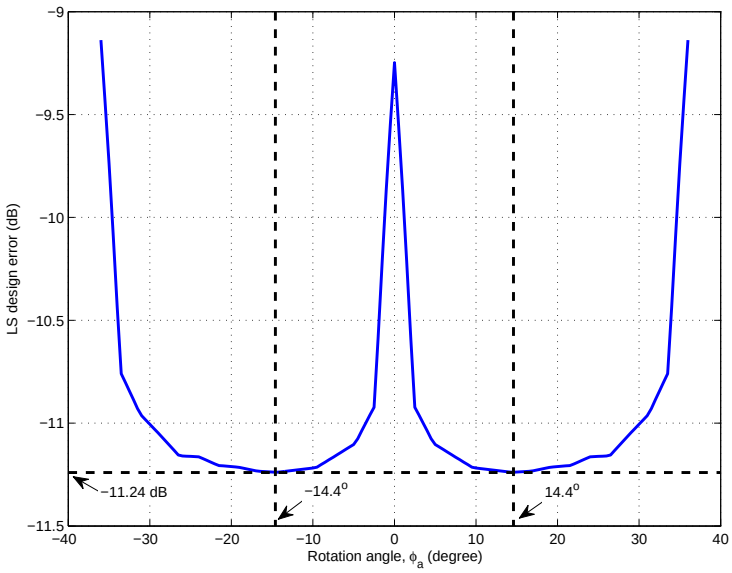

(b) $P = 5$.

Figure 3.4: Plot of weighted LS design errors versus ϕ_a for $P = 4$ and 5.

where $N-1$ is the order of Farrow structure, L is the length of each FIR filter, T_S is the sampling period, $w(\cdot)$ are the FIR filter weights, and $\tilde{\psi}$ is the Farrow parameter. The array element response, $w(\cdot)$ can take the form of (2.3) for a nearfield source, (2.5) for a nearfield source normalised with respect to a reference point or (2.8) for a farfield source. For the design of SBBFs, $\tilde{\psi}$ is related to the steering direction by

$$\tilde{\psi} = \frac{\psi}{\alpha} \tag{3.6}$$

where ψ is the steering direction and α is the normalising constant such that $\tilde{\psi} \in [-0.5, 0.5]$. Let

$$\tilde{\boldsymbol{\psi}} = \left[\tilde{\psi}^0, ..., \tilde{\psi}^{N-1}\right]^{\mathrm{T}} \tag{3.7}$$

$$\mathbf{e}(\omega) = \left[1, ..., \exp\left(-i\omega T_S (L-1)\right)\right]^{\mathrm{H}} \tag{3.8}$$

and $\mathbf{a}(\omega, \mathbf{r}_s)$ and $\mathbf{w}$ be column vectors with their elements given by

$$\left[\mathbf{a}(\omega, \mathbf{r}_s)\right]_k = a^*(\mathbf{r}_k, \omega, \mathbf{r}_s) \tag{3.9}$$

$$\left[\mathbf{w}\right]_j = w_{p,m,n}(l) \tag{3.10}$$

where $j = pM + mN + nL + l$. Equation (3.5) can be written compactly in matrix form as follows

$$B\left(\tilde{\psi}, \omega, \mathbf{r}_s\right) = \mathbf{d}^{\mathrm{H}}(\psi, \omega, \mathbf{r}_s)\,\mathbf{w} \tag{3.11}$$

where

$$\mathbf{d}(\psi, \omega, \mathbf{r}_s) = \mathbf{a}(\omega, \mathbf{r}_s) \otimes \tilde{\boldsymbol{\psi}} \otimes \mathbf{e}(\omega) \tag{3.12}$$

and $\otimes$ is the Kronecker product.

The frequency domain or narrowband equivalent of the beamformer structure of Fig. 3.5 is shown in Fig. 3.6. Its response is given by

$$B\left(\tilde{\psi}, \omega, \mathbf{r}_s\right) = \sum_{k=0}^{PM-1} a(\mathbf{r}_k, \omega, \mathbf{r}_s) \sum_{n=0}^{N-1} \tilde{\psi}^n W_{p,m,n}(\omega) \tag{3.13}$$

where $W(\cdot)$ is a complex filter transfer function. Let $\mathbf{W}(\omega)$ be a column vector with its element given by

$$\left[\mathbf{W}(\omega)\right]_v = W_{p,m,n}(\omega) \tag{3.14}$$

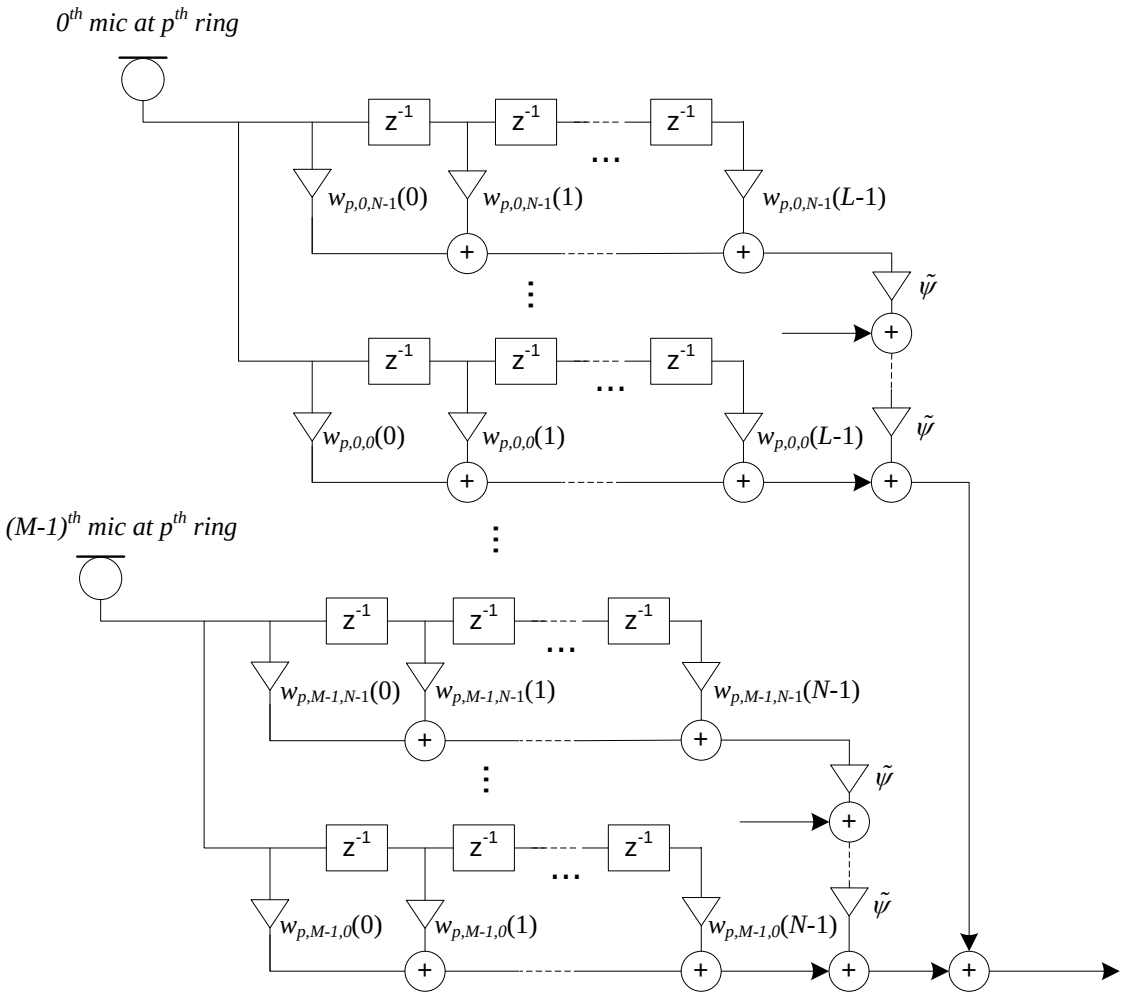

Figure 3.5: Time domain steerable broadband beamformer structure using the Farrow structure.

where $v = pM + mN + n$. Equation (3.13) can be written compactly as

$$B\left(\tilde{\psi}, \omega, \mathbf{r}_s\right) = \mathbf{d}_f^{\mathrm{H}}\left(\psi, \omega, \mathbf{r}_s\right) \mathbf{W}\left(\omega\right) \tag{3.15}$$

where

$$\mathbf{d}_f\left(\psi, \omega, \mathbf{r}_s\right) = \mathbf{a}\left(\omega, \mathbf{r}_s\right) \otimes \tilde{\boldsymbol{\psi}}. \tag{3.16}$$

Note that the beamformer responses have been derived using the nearfield source model. For farfield sources, the dependence of the beamformer response $B\left(\cdot\right)$ and array response $a\left(\cdot\right)$ on the source position $\mathbf{r}_s$ reduces to the direction of arrival ϕ_s of the source.

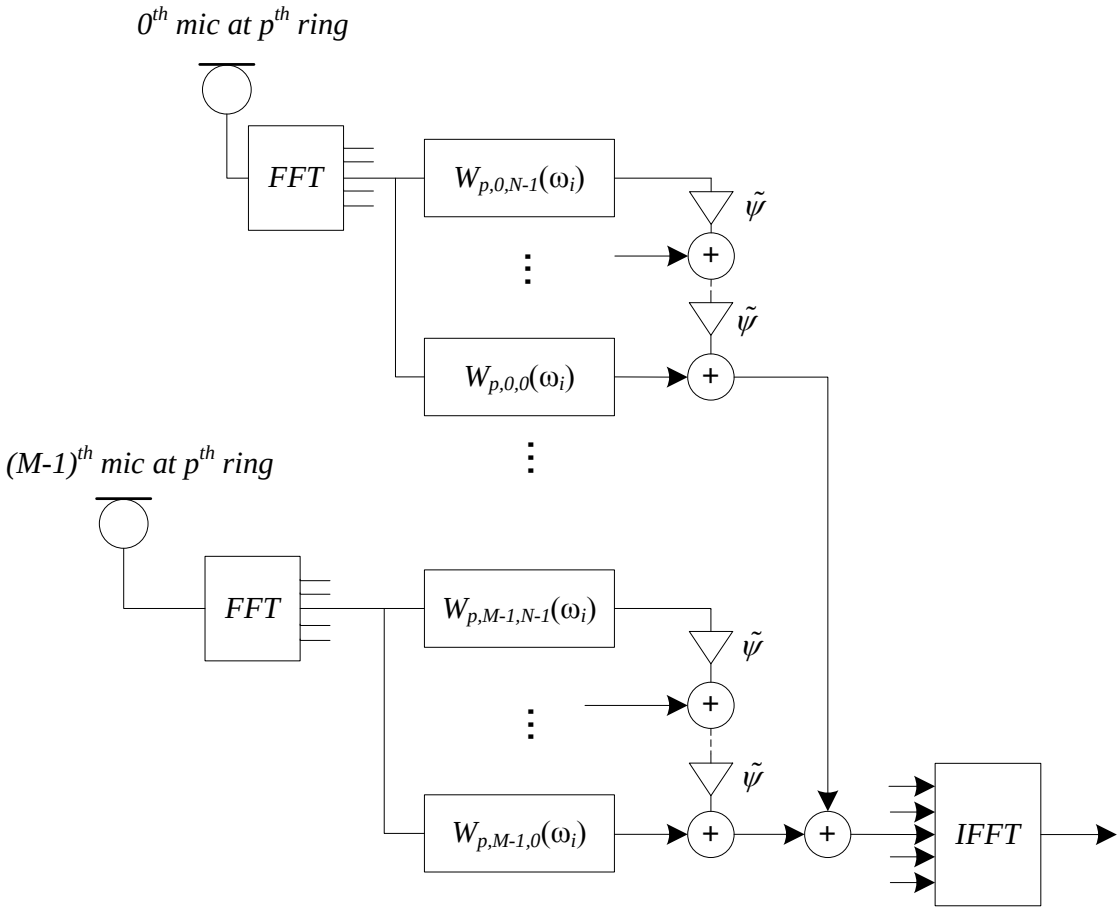

Figure 3.6: Frequency domain steerable broadband beamformer structure.

3.4 Design formulation

The design of SBBFs can be posed as an optimisation problem to minimise the error between the actual beamformer response $B\left(\tilde{\psi}, \omega, \phi_s\right)$ and a desired response $B_d\left(\psi, \omega, \phi_s\right)$. It should be noted that $B\left(\tilde{\psi}, \omega, \phi_s\right)$ in this section comes directly from (3.5) for time domain designs and (3.15) for frequency domain designs. However, r_s is dropped since the design formulations that follow are for beamformers operating for a particular source distance, instead of a range of source distances (see Chapter 5). Hence, the array element response in $B\left(\tilde{\psi}, \omega, \phi_s\right)$ can still be selected to be (2.3) or (2.5) for a nearfield source (with $\|\mathbf{r}_s\|$ fixed to a nearfield distance) or (2.8) for a farfield source.

3.4.1 Weighted least squares

3.4.1.1 Frequency domain design

Define an error function

$$\xi\left(\psi, \omega, \phi_s\right) = B\left(\tilde{\psi}, \omega, \phi_s\right) - B_d\left(\psi, \omega, \phi_s\right). \tag{3.17}$$

Its absolute error squared can then be expressed as

$$\begin{aligned}\left|\xi\left(\psi, \omega, \phi_s\right)\right|^2 = \mathbf{W}^{\mathrm{H}}\left(\omega\right)\mathbf{Q}\left(\psi, \omega, \phi_s\right)\mathbf{W}\left(\omega\right) - 2\mathrm{Re}\left\{\mathbf{q}^{\mathrm{H}}\left(\psi, \omega, \phi_s\right)\mathbf{W}\left(\omega\right)\right\} \\ + \left|B_d\left(\psi, \omega, \phi_s\right)\right|^2\end{aligned} \tag{3.18}$$

where

$$\mathbf{Q}_f\left(\psi, \omega, \phi_s\right) = \mathbf{d}_f\left(\psi, \omega, \phi_s\right)\mathbf{d}_f^{\mathrm{H}}\left(\psi, \omega, \phi_s\right), \tag{3.19}$$

$$\mathbf{q}_f\left(\psi, \omega, \phi_s\right) = \mathbf{d}_f\left(\psi, \omega, \phi_s\right)B_d\left(\psi, \omega, \phi_s\right) \tag{3.20}$$

and $\mathrm{Re}\left\{\cdot\right\}$ denotes the real part. The weighted LS complex, frequency dependent beamformer weights $\mathbf{W}\left(\omega\right)$ can be found by solving

$$\min_{\mathbf{W}(\omega)} J_{LS}\left(\omega\right) \qquad \forall\omega \in \Omega \tag{3.21}$$

with Ω represents the frequency range of interest, and

$$J_{LS}\left(\omega\right) = \int_{\Psi}\int_{\Phi} V\left(\psi, \omega, \phi_s\right)\left|\xi\left(\psi, \omega, \phi_s\right)\right|^2 d\phi_s d\psi \tag{3.22}$$

where $V(\cdot)$ is a weighting function, and Ψ and Φ are, respectively, the regions of interest for the steering angle and the azimuth angle. The weighted LS objective function $J_{LS}(\omega)$ in matrix form is as follows

$$J_{LS}(\omega) = \mathbf{W}^{\mathrm{H}}(\omega)\,\mathbf{Q}(\omega)\,\mathbf{W}(\omega) - 2\mathrm{Re}\left\{\mathbf{q}^{\mathrm{H}}(\omega)\,\mathbf{W}(\omega)\right\} + b(\omega) \tag{3.23}$$

where

$$\mathbf{Q}(\omega) = \int_{\Psi}\int_{\Phi} V(\psi,\omega,\phi_s)\,\mathbf{Q}_f(\psi,\omega,\phi_s)\,d\phi_s d\psi, \tag{3.24}$$

$$\mathbf{q}(\omega) = \int_{\Psi}\int_{\Phi} V(\psi,\omega,\phi_s)\,\mathbf{q}_f(\psi,\omega,\phi_s)\,d\phi_s d\psi, \tag{3.25}$$

$$b(\omega) = \int_{\Psi}\int_{\Phi} V(\psi,\omega,\phi_s)\,|B_d(\psi,\omega,\phi_s)|^2\,d\phi_s d\psi. \tag{3.26}$$

Minimising (3.23) with respect to $\mathbf{W}(\omega)$ results in the analytical solution

$$\mathbf{W}(\omega) = \mathbf{Q}^{-1}(\omega)\,\mathbf{q}(\omega). \tag{3.27}$$

3.4.1.2 Time domain design

The same formulation can be posed in the time domain where the absolute error squared is now given by

$$|\xi(\psi,\omega,\phi_s)|^2 = \mathbf{w}^{\mathrm{H}}\mathbf{Q}(\psi,\omega,\phi_s)\,\mathbf{w} - 2\mathrm{Re}\left\{\mathbf{q}^{\mathrm{H}}(\psi,\omega,\phi_s)\,\mathbf{w}\right\} + |B_d(\psi,\omega,\phi_s)|^2 \tag{3.28}$$

where

$$\mathbf{Q}(\psi,\omega,\phi_s) = \mathbf{d}(\psi,\omega,\phi_s)\,\mathbf{d}^{\mathrm{H}}(\psi,\omega,\phi_s), \tag{3.29}$$

$$\mathbf{q}(\psi,\omega,\phi_s) = \mathbf{d}(\psi,\omega,\phi_s)\,B_d(\psi,\omega,\phi_s). \tag{3.30}$$

The weighted LS objective function is given by

$$J_{LS} = \int_{\Psi}\int_{\Omega}\int_{\Phi} V(\psi,\omega,\phi_s)\,|\xi(\psi,\omega,\phi_s)|^2\,d\phi_s d\omega d\psi \tag{3.31}$$

and the real beamformer weights $\mathbf{w}$ can be found by solving

$$\min_{\mathbf{w}} J_{LS}. \tag{3.32}$$

Rewriting (3.31) in matrix form yields

$$J_{LS} = \mathbf{w}^{\mathrm{T}}\mathbf{Q}\mathbf{w} - 2\left(\mathrm{Re}\{\mathbf{q}\}\right)^{\mathrm{T}}\mathbf{w} + b \tag{3.33}$$

where

$$\mathbf{Q} = \int_{\Psi}\int_{\Omega}\int_{\Phi} V(\psi,\omega,\phi_s)\,\mathbf{Q}(\psi,\omega,\phi_s)\,d\phi_s d\omega d\psi, \tag{3.34}$$

$$\mathbf{q} = \int_{\Psi}\int_{\Omega}\int_{\Phi} V(\psi,\omega,\phi_s)\,\mathbf{q}(\psi,\omega,\phi_s)\,d\phi_s d\omega d\psi, \tag{3.35}$$

$$b = \int_{\Psi}\int_{\Omega}\int_{\Phi} V(\psi,\omega,\phi_s)\,|B_d(\psi,\omega,\phi_s)|^2\,d\phi_s d\omega d\psi. \tag{3.36}$$

Minimising (3.33) with respect to $\mathbf{w}$ and constraining $\mathbf{w}$ to be real gives the analytical solution

$$\mathbf{w} = (\mathrm{Re}\{\mathbf{Q}\})^{-1}\,\mathrm{Re}\{\mathbf{q}\}. \tag{3.37}$$

3.4.2 Weighted total least squares

In this section, the SBBFs design is reformulated in the weighted TLS sense [53]. The main advantage of this design formulation is that no matrix inversion is required to solve the design analytically [54] and the formulation is unbiased [55], as opposed to the weighted LS design formulation. The weighted TLS design formulation, which minimises the Rayleigh quotient, can be solved using singular value decomposition (SVD) which is numerically robust.

3.4.2.1 Frequency domain design

The error between $B\left(\tilde{\psi},\omega,\phi_s\right)$ and $B_d(\psi,\omega,\phi_s)$ in TLS sense is given by

$$\xi_{TLS}(\psi,\omega,\phi_s) = \frac{|\xi(\psi,\omega,\phi)|}{\sqrt{A(\omega)+1}} \tag{3.38}$$

where for broadband beamforming, $A(\omega)$ is given by [56]

$$A(\omega) = \int_{\Psi}\int_{-\pi}^{\pi} V(\psi,\omega,\phi_s)\left|B(\tilde{\psi},\omega,\phi_s)\right|^2 d\phi_s d\psi = \mathbf{W}^{\mathrm{H}}(\omega)\,\mathbf{Q}_T(\omega)\,\mathbf{W}(\omega) \tag{3.39}$$

with

$$\mathbf{Q}_T(\omega) = \int_{\Psi}\int_{-\pi}^{\pi} V(\psi,\omega,\phi_s)\,\mathbf{Q}_f(\psi,\omega,\phi_s)\,d\phi_s d\psi. \tag{3.40}$$

The detailed interpretation of (3.38) can be found in [53, 57]. Defining the weighted TLS objective function as

$$\begin{aligned} J_{TLS}(\omega) &= \int_{\Psi}\int_{\Phi} V(\psi,\omega,\phi_s)\xi_{TLS}^2(\psi,\omega,\phi_s)d\phi_s d\psi \\ &= \frac{\tilde{\mathbf{W}}^{\mathrm{H}}(\omega)\,\tilde{\mathbf{Q}}(\omega)\,\tilde{\mathbf{W}}(\omega)}{\tilde{\mathbf{W}}^{\mathrm{H}}(\omega)\,\tilde{\mathbf{Q}}_T(\omega)\,\tilde{\mathbf{W}}(\omega)} \end{aligned} \tag{3.41}$$

where

$$\tilde{\mathbf{Q}}(\omega) = \begin{bmatrix} \mathbf{Q}(\omega) & \mathbf{q}(\omega) \\ \mathbf{q}^{\mathrm{H}}(\omega) & b(\omega) \end{bmatrix}, \tag{3.42}$$

$$\tilde{\mathbf{Q}}_T(\omega) = \begin{bmatrix} \mathbf{Q}_T(\omega) & \mathbf{0} \\ \mathbf{0} & 1 \end{bmatrix}, \tag{3.43}$$

$$\tilde{\mathbf{W}}(\omega) = \begin{bmatrix} \mathbf{W}(\omega) \\ -1 \end{bmatrix}, \tag{3.44}$$

the weighted TLS design formulation is given by

$$\min_{\tilde{\mathbf{W}}(\omega)} J_{TLS}(\omega) \qquad \forall \omega \in \Omega. \tag{3.45}$$

Note that (3.41) is the Rayleigh-Ritz ratio whose minimum is given by the smallest generalised eigenvalue of $\tilde{\mathbf{Q}}(\omega)$ and $\tilde{\mathbf{Q}}_T(\omega)$. Hence, the minimisation problem (3.45) can be solved analytically since according to the Rayleigh-Ritz's principle, the solution vector $\tilde{\mathbf{W}}(\omega)$ is simply the generalised eigenvector of $\tilde{\mathbf{Q}}(\omega)$ and $\tilde{\mathbf{Q}}_T(\omega)$ that corresponds to their smallest generalised eigenvalue [53, 56, 58]. The beamformer coefficients vector $\mathbf{W}(\omega)$ is extracted from $\tilde{\mathbf{W}}(\omega)$ after scaling its last element to -1. Since the analytical solution of this design formulation is given by the eigenvector of its matrices, this formulation is also called the eigenfilter design method.

3.4.2.2 Time domain design

As for the time domain design, the TLS error function is given by

$$\xi_{TLS}(\psi, \omega, \phi_s) = \frac{|\xi(\psi, \omega, \phi_s)|}{\sqrt{A+1}} \tag{3.46}$$

where

$$A = \int_{\Psi} \int_{0}^{\pi} \int_{-\pi}^{\pi} V(\psi, \omega, \phi_s) \left| B(\tilde{\psi}, \omega, \phi_s) \right|^2 d\phi_s d\omega d\psi = \mathbf{w}^{\mathrm{H}} \mathbf{Q}_T \mathbf{w}, \tag{3.47}$$

$$\mathbf{Q}_T = \int_{\Psi} \int_{0}^{\pi} \int_{-\pi}^{\pi} V(\psi, \omega, \phi_s) \mathbf{Q}(\psi, \omega, \phi_s) d\phi_s d\omega d\psi. \tag{3.48}$$

Hence, the weighted TLS objective function is now

$$\begin{aligned} J_{TLS} &= \int_{\Psi}\int_{\Omega}\int_{\Phi} V(\psi,\omega,\phi_s)\xi_{TLS}^2(\psi,\omega,\phi_s)d\phi_s d\omega d\psi \\ &= \frac{\tilde{\mathbf{w}}^{\mathrm{T}}\tilde{\mathbf{Q}}\tilde{\mathbf{w}}}{\tilde{\mathbf{w}}^{\mathrm{T}}\tilde{\mathbf{Q}}_T\tilde{\mathbf{w}}} \end{aligned} \tag{3.49}$$

where

$$\tilde{\mathbf{Q}} = \mathrm{Re}\left\{\begin{bmatrix} \mathbf{Q} & \mathbf{q} \\ \mathbf{q}^{\mathrm{H}} & b \end{bmatrix}\right\}, \tag{3.50}$$

$$\tilde{\mathbf{Q}}_T = \mathrm{Re}\left\{\begin{bmatrix} \mathbf{Q}_T & \mathbf{0} \\ \mathbf{0} & 1 \end{bmatrix}\right\}, \tag{3.51}$$

$$\tilde{\mathbf{w}} = \begin{bmatrix} \mathbf{w} \\ -1 \end{bmatrix}. \tag{3.52}$$

The time domain weighted TLS design formulation is given by

$$\min_{\tilde{\mathbf{w}}} J_{TLS}. \tag{3.53}$$

Similarly, from the Rayleigh-Ritz's principle, the analytical solution vector $\tilde{\mathbf{w}}$ that minimises (3.49) is given by the generalised eigenvector of $\tilde{\mathbf{Q}}$ and $\tilde{\mathbf{Q}}_T$ that corresponds to the smallest generalised eigenvalue. The beamformer coefficients vector $\mathbf{w}$ is extracted from $\tilde{\mathbf{w}}$ after scaling its last element to -1.

3.5 Design examples and discussion

3.5.1 Design specifications and evaluation quantities

In order to illustrate the design formulations of Section 3.4, a number of design examples in the time domain are presented and evaluated. For farfield beamformer designs, (2.8) is used as the array element response. For nearfield beamformer designs, (2.3) is used instead, with $\|\mathbf{r}_s\| = 1$m. Other design parameters are listed in Table 3.2 and 3.3, where appropriate 2π wrapping has been considered for the spatial pass region and stop region. For simplicity, the weighting function is chosen to be $V(\psi,\omega,\phi_s) = 1$.

Note that the steering range Ψ is limited to a sector, i.e. $\Psi \in [-36°, 36°]$. This reduces the design problem size and improves the steering performance since the steering range is now limited to only a sector rather than the entire 360°. However, a full 360°steering is still possible with this design specification due to the circular symmetry of the sensor array. Main-beam steering outside the steering range can be achieved by rotating the Farrow filters with respect to the sensor positions, followed by main-beam steering with the steering parameter ψ.

The triple integrals in the design formulation is approximated by discrete sum, where the ranges Ψ, Ω and Φ are uniformly discretised into 8, 128 and 180 points respectively. As the designs involve three independent variables ψ, ω and ϕ, it is difficult to increase their number of discretisation points as the problem can easily become huge and unmanageable.

The desired beamformer response is defined by

$$B_d(\psi, \omega, \phi_s) = \begin{cases} \exp\left(-i\omega T_S \frac{L-1}{2}\right) & , \ \omega \in \Omega_{pb}, \phi_s \in \Phi_{pb}(\psi) \\ 0 & , \ \omega \in \Omega_{sb}, \phi_s \in \Phi_{sb}(\psi). \end{cases} \tag{3.54}$$

For evaluating the beamformers, two performance measures are used. The first one is the directivity index (DI) defined as [59]

$$D(\psi, \omega) = 10\log_{10}\left(\frac{2\pi |B(\psi, \omega, \psi)|^2}{\int_\Phi |B(\psi, \omega, \phi_s)|^2 d\phi_s}\right). \tag{3.55}$$

The second quantitative measure is the performance error function defined as

$$\xi_{LS}(\psi) = \int_\Omega \int_\Psi |\xi(\psi, \omega, \phi_s)|^2 d\phi_s d\omega \tag{3.56}$$

for LS designs and

$$\xi_{TLS}(\psi) = \frac{\xi_{LS}(\psi)}{A_e(\psi) + 1} \tag{3.57}$$

for TLS design where $A_e(\psi)$ is defined by

$$A_e(\psi) = \int_\Omega \int_\Psi |B_d(\psi, \omega, \phi_s)|^2 d\phi_s d\omega. \tag{3.58}$$

Note that $A_e(\psi)$ in (3.58) is taken to be the total area under the desired beampattern rather than the actual beampattern (c.f. (3.47)) in order to avoid inappropriate scaling of the TLS performance error, which occurs when assessing the performance outside the design region.

Table 3.2: Design parameters for sensor array.

Parameter	**Value**
Number of rings, P	4
Number of sensors per ring, M	5
Ring radii, r_p	$\{0.033, 0.089, 0.242, 0.657\}$m
Ring rotation angle, ϕ_a	12^o

Table 3.3: Design parameters for beamformer.

Parameter	**Value**
Sampling frequency, f_S	8 kHz
Spectral passband, Ω_{pb}	$[0.2, 3.8]$ kHz
Spectral stopband, Ω_{sb}	$[0, 0.1] \cup [3.95, 4]$ kHz
Spatial pass region, $\Phi_{pb}(\psi)$	$\lvert\phi - \psi\rvert \leq 15^o$
Spatial stop region, $\Phi_{sb}(\psi)$	$\lvert\phi - \psi\rvert \geq 25^o$
Steering angle range, Ψ	$\left[-\frac{180^o}{M}, \frac{180^o}{M}\right]$
Order of Farrow structure, $N-1$	4
FIR filter length, L	64
Speed of propagating wave, c	343 m/s

3.5.2 Farfield beamformer designs

The performance error plots for both farfield LS and TLS designs are shown in Fig. 3.7. As can be seen, the low and constant performance error within the designed steering region Ψ indicates that in both the designs, their responses remain invariant when the main-beam is steered within the design region. This is further supported by their high and constant DI values (around 20dB) within the design region (between the dashed lines) shown in Fig. 3.8. Besides, it can be seen from Fig. 3.8 that there is a small region outside the steering range Ψ before the beamformers fail completely. In order to highlight the invariant response to different steering direction within the steering range Ψ, the beampatterns for the LS design steered to $\psi = -20^o$ and 30^o are shown in Fig. 3.9.

As discussed in Section 3.2.1, the circular symmetric nature of the spiral arm array geometry can be exploited to provide a full 360^o. In this case, the steering of the main-beam to any look direction can be achieved by appropriately rotating the Farrow structure with respect to the sensors, followed by the main-beam steering using the steering parameter. For example, in order to steer the main-beam to 150^o, which is outside of the design range Ψ (see Fig. 3.10), the Farrow structure is rotated twice in clockwise direction to steer the main-beam to 144^o. Then, the steering parameter is set to $\psi = 6^o$ to further steer the main-beam 6^o clockwise to reach the total desired look direction of 150^o. This implies the beamformer need to be designed only for a steering range covering a full sector $\Psi = [-\pi/M, \pi/M]$, thus reducing the design complexity, and yet a full 360^o steering range is achievable.

3.5.3 Nearfield beamformer designs

The performance error and DI plots for both the nearfield LS andTLS designs are shown in Figs. 3.11 and 3.12, respectively. The similarity to their farfield counterparts' performance in Section 3.5.2 shows that the same design formulations discussed in Section 3.4 can be employed for nearfield beamformer designs, by simply applying the nearfield array element response, instead. In addition, full 360^o steering capability is still present due to the symmetry of the array geometry,

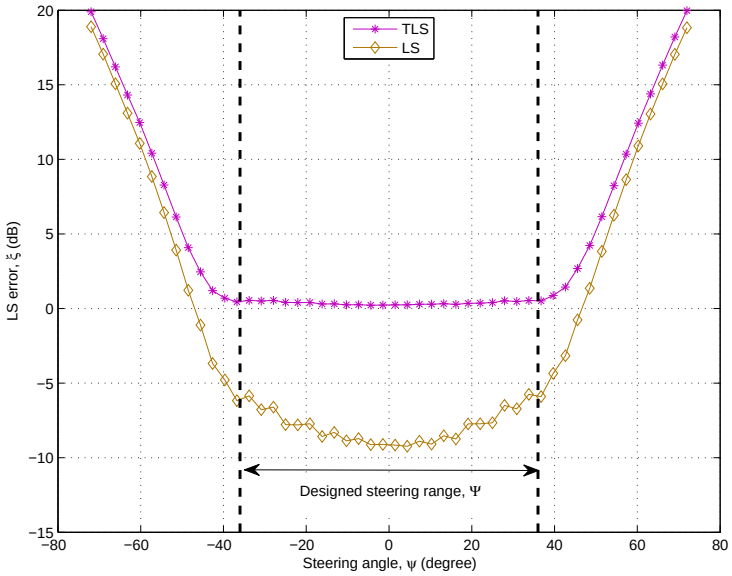

Figure 3.7: Performance error for farfield LS and TLS designs.

as shown by the beampattern for the nearfield LS design steered to $\psi = 150^o$ in Fig. 3.13.

For comparison purpose, Fig. 3.14 shows the beampatterns for both farfield and nearfield designs, plotted on top of the desired beampattern at 1kHz. Note that in these designs, the beamformer weights are optimised such that their beampatterns are matched as close as possible to the desired response. Hence, different choice of desired response (3.54) will result in different designs.

3.6 Conclusions

In this chapter, the design of 2D SBBFs realised with the Farrow structure has been established. The designs are formulated in both weighted LS and TLS sense and in the time and frequency domains. The major advantage of the Farrow structure is that the main-beam of the beamformer can be steered easily and directly with a single real parameter. Design examples show that the beamformer responses are invariant within the designed spectral and steering angle range, validating the broadband as well as the main-beam steering capability of the designs.

In addition, full 360^o steering range is possible by exploiting the circular sym-

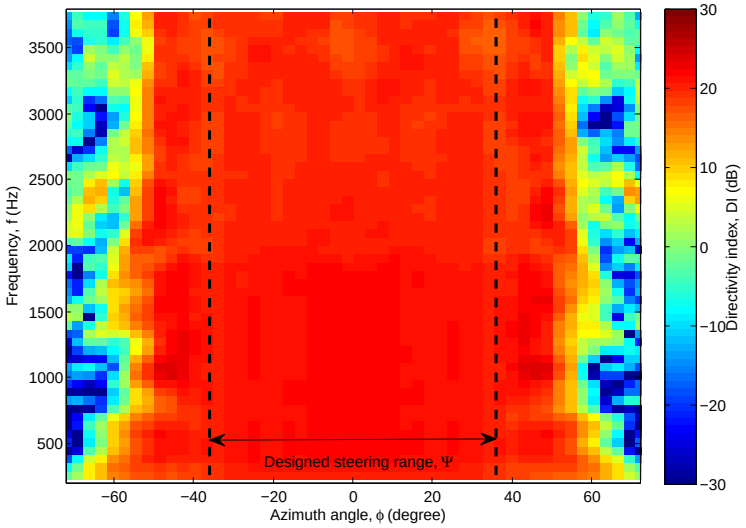

(a) LS design.

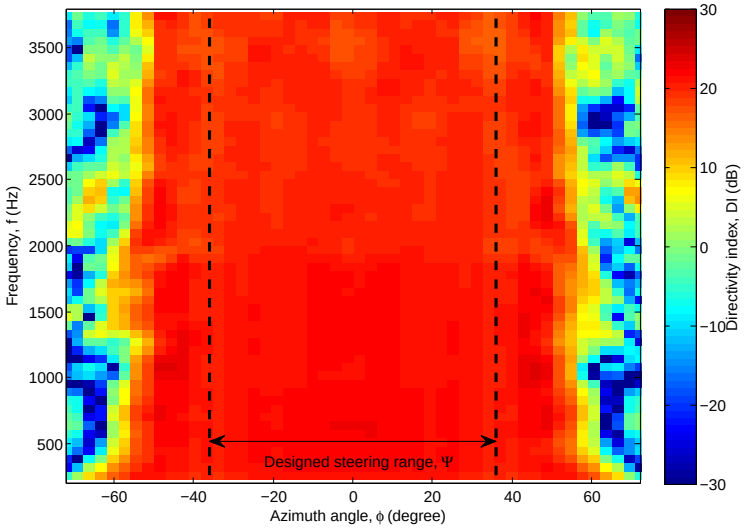

(b) TLS design.

Figure 3.8: Directivity index for farfield LS and TLS designs.

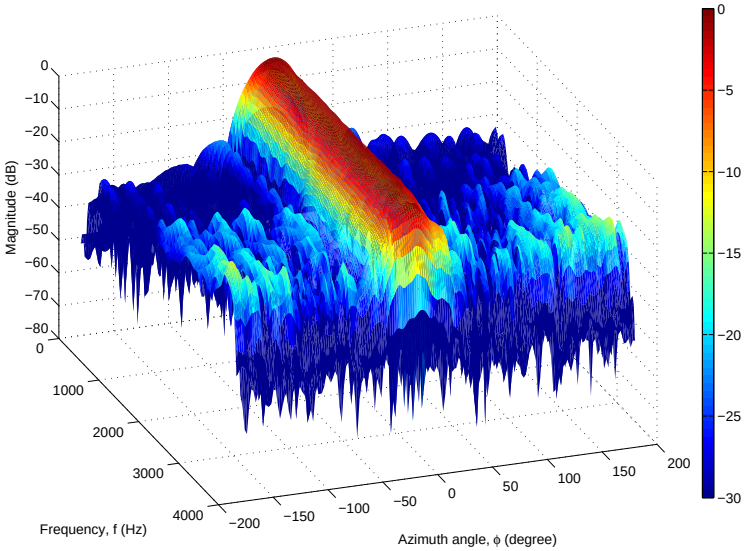

(a) $\psi = -20°$.

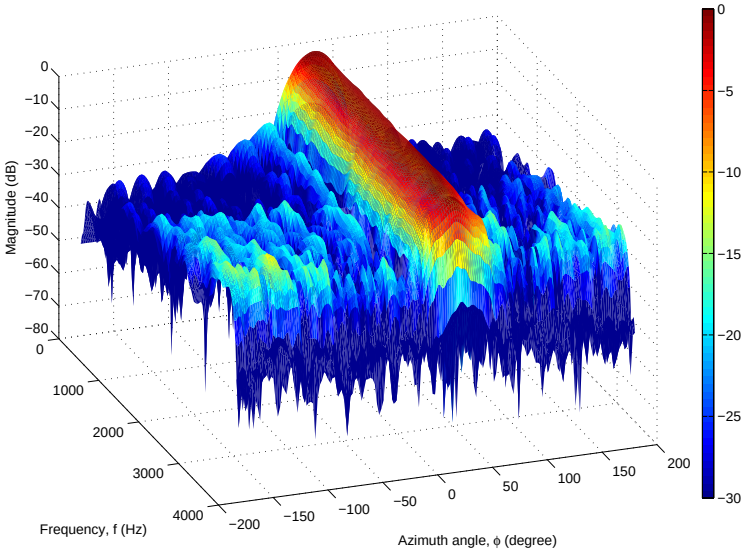

(b) $\psi = 30°$.

Figure 3.9: Beampatterns for farfield LS design steered to $\psi = -20°$and $30°$.

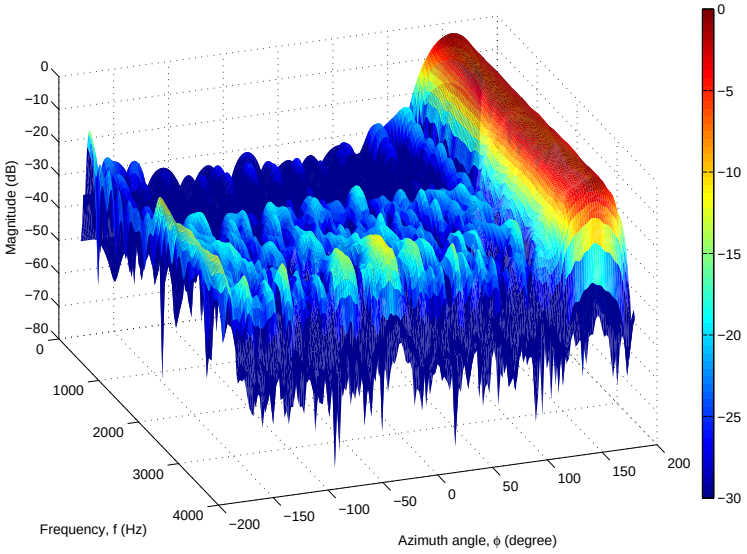

Figure 3.10: Beampattern for farfield LS design steered to $\psi = 150°$.

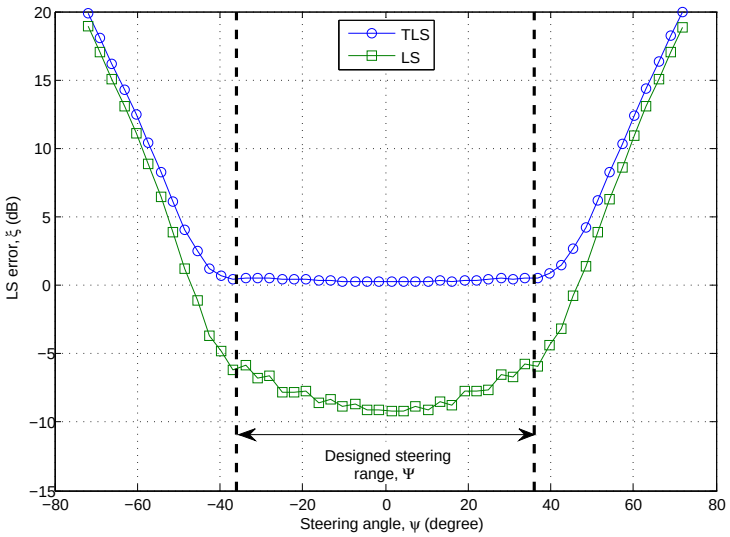

Figure 3.11: Performance error for nearfield LS and TLS designs.

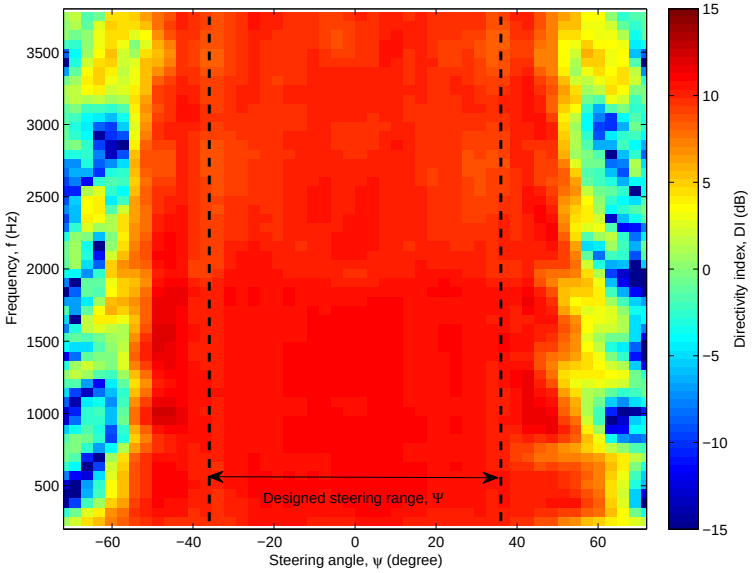

(a) LS design.

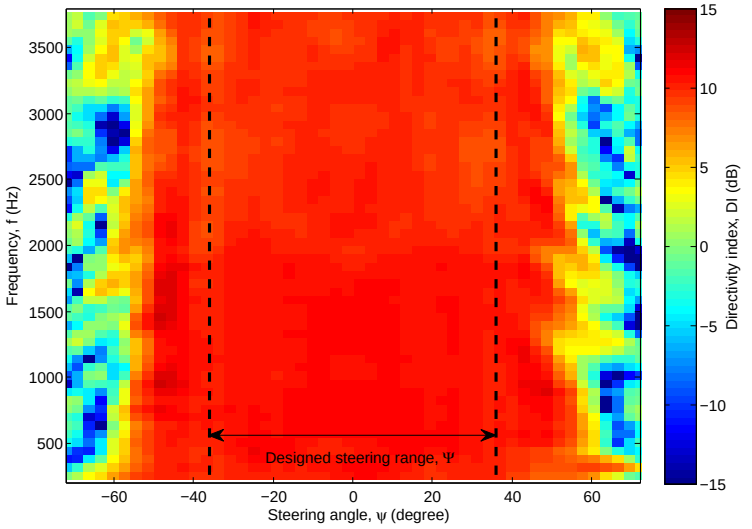

(b) TLS design.

Figure 3.12: Directivity index for nearfield LS and TLS designs.

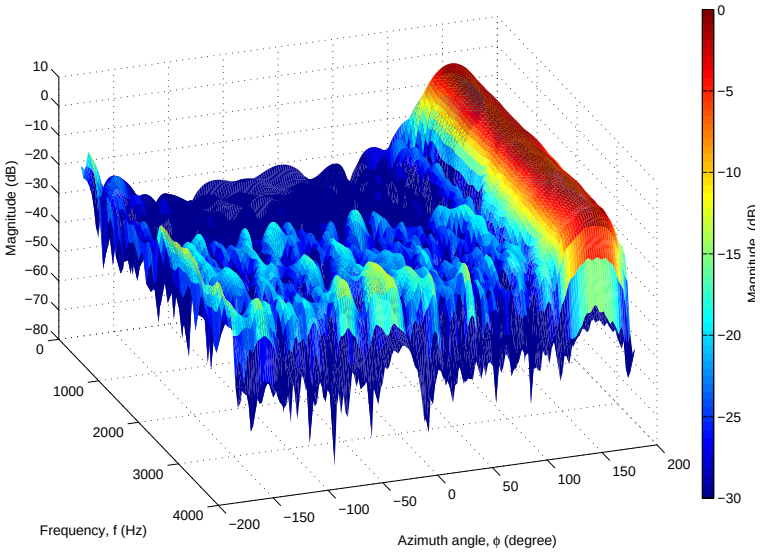

Figure 3.13: Beampattern for nearfield LS design steered to $\psi = 150°$.

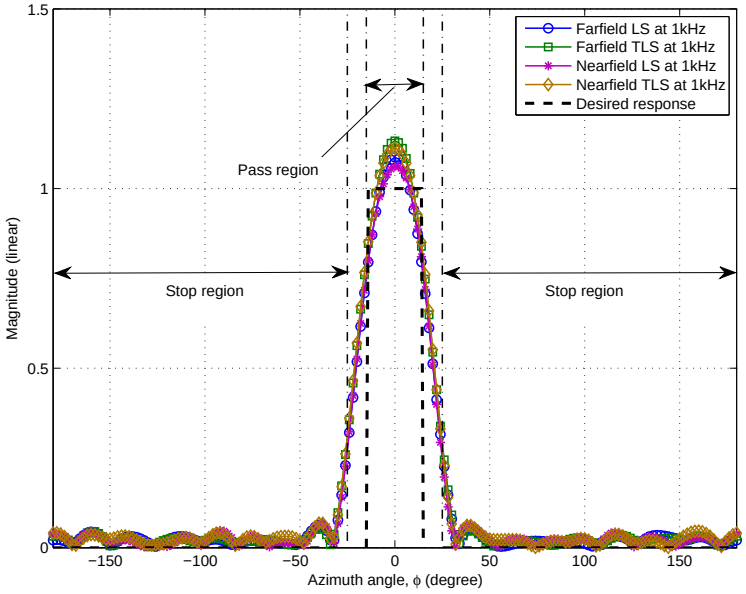

Figure 3.14: Desired and actual beampatterns at 1kHz.

metry nature of the array geometry. This is achieved by appropriately permuting the beamformer weights. This property can reduce the beamformer design complexity since the steering range needs only to cover a sector and yet a full 360^o steering range is possible. This shows that the choice of array geometry is equally important as beamformer weights in SBBF designs.

Chapter 4

Robust Formulation Using Stochastic Model

4.1 Introduction

In practice, it is impossible to have a completely error free model for designing beamformer. Hence, robustness to such errors is a major consideration in the design of practical beamformers. Beamformers, especially superdirective beamformers and small array beamformers, are known to be very sensitive to slight error and deviation between the presumed and actual model [59–63]. Any violation of the underlying assumptions can degrade significantly their performance. Causes for such violations can be due to mismatches between the presumed and actual array element characteristics [54], imperfect array calibration [64], error in the sensor positions [65], electronics self-noise, medium inhomogeneity [66], nearfield-farfield mismatch [67], mutual coupling between sensors [68], local scattering and source spreading [69–72], to name a few. The importance of these errors depends heavily on the type of sensor used in the sensor array as well as the area of application. For example, the effect of mutual coupling between sensors is often negligible in acoustic beamforming but not in wideband radio antenna beamforming [73].

A major issue in acoustic broadband beamformers is that at low frequencies, they behave like superdirective or small array beamformers. In these beam-

formers, the element spacings are normally small relative to the operating signal wavelength [59–63]. As a result, the array aperture size is not sufficient to provide good signal directivity and every array element essentially "sees" the same signal sample. In order to achieve high directivity in such beamformers, the dynamic range of the beamformer weights need to be very large. Although these large weights can increase the beamformer's gain theoretically, which is desired, it causes the beamformers to be extremely sensitive to errors and perturbations which exist in practise.

The most common method to introduce robustness to such errors is to include a white noise gain (WNG) constraint in the design of the beamformer weights. This is equivalent to the diagonal loading method if the designs are expressed in matrix form [46, 60–63, 74, 75]. Although perturbations and deviations from practical models can be translated to WNG, there is no clear link between the two. Hence, it is difficult to select an appropriate level of WNG for any given set of errors in practice. This is the main limitation of the WNG method, though it does provide a quick and simple method to achieve robustness.

The other method to achieve robustness is to include tolerance towards errors in the ideal models to account for practical imperfections. Beamformers are then designed by optimising an objective function, which include the tolerance, based either on their worst-case or on their mean performances [62, 76–78]. Both of these approaches have their own advantages and drawbacks. Optimising for the worst-case performance ensures the resulting beamformers can operate for all the condition, including the worst-case scenario. However, such designs are too pessimistic in the sense that the worst-case scenario may be too far from the mean scenario and may only occur infrequently. On the other hand, optimising for the mean performance ensures the beamformers can operate in the vicinity of the mean conditions. Hence, if there is a sudden occurrence which shifts the operating condition far away from the mean condition, the beamformer may fail. The suitability of these methods depends heavily on the target applications.

For the mean performance optimisation, it can be extended to include a stochastic model to describe the error characteristics [54, 79]. This enables explicit quantification of the parameters related to practical environments, sources,

and array models which are known probabilistically, thus allowing a more direct and meaningful quantification of physical parameters and their desired tolerance. Besides, such stochastic model is applicable in most cases, where the errors are random and only their stochastic characteristics are known. In addition, the stochastic error model is more sensible in the sense that the errors are weighted by their probability density function, i.e. errors that occur more frequently are weighted higher than those that occur less frequently. Hence, its mean performance, where the errors are concentrated, is optimised to achieve optimal mean performance.

This chapter discusses a stochastic error model for broadband beamformer design, which is an extension to the model in [54, 79]. The discussion includes formulations involving the multiplicative errors, additive errors and their combinations. The multiplicative error model is useful to model errors that can be translated into errors in the array elements, such as their non-ideal characteristics, mismatches between the array elements, errors in the sensor positions and errors in the presumed source position. The additive error model is useful to model errors due to source spreading and local scattering [80].

This chapter is organised as follows. Section 4.2 provides a detailed formulation of the stochastic error model in terms of gain and phase errors. Section 4.3 discusses the incorporation of the stochastic error model into different broadband beamformer design formulations to achieve robust designs. Section 4.4 provides the performance evaluations, comparisons and discussion for a number of robust beamformer examples using the stochastic error model, and lastly, conclusions are drawn in Section 4.5.

4.2 Stochastic error model

4.2.1 Multiplicative error

Sensor errors $\varepsilon(\mathbf{r}_k, \omega, \mathbf{r}_s)$ such as gain and phase errors can often be modelled as multiplicative errors [54, 79], i.e.

$$\varepsilon(\mathbf{r}_k, \omega, \mathbf{r}_s) = \varepsilon_\rho(\mathbf{r}_k, \omega, \mathbf{r}_T) \exp\left(j\varepsilon_\gamma(\mathbf{r}_k, \omega, \mathbf{r}_s)\right). \tag{4.1}$$

where $\varepsilon_\rho(\mathbf{r}_k, \omega, \mathbf{r}_s)$ is the gain error and $\varepsilon_\gamma(\mathbf{r}_k, \omega, \mathbf{r}_s)$ is the phase error. The perturbed array element response can then be written as

$$\hat{a}(\mathbf{r}_k, \omega, \mathbf{r}_s) = \varepsilon(\mathbf{r}_k, \omega, \mathbf{r}_s) a(\mathbf{r}_k, \omega, \mathbf{r}_s) \tag{4.2}$$

or in vector form as

$$\hat{\mathbf{a}}(\omega, \mathbf{r}_s) = \boldsymbol{\varepsilon}(\omega, \mathbf{r}_s) \odot \mathbf{a}(\omega, \mathbf{r}_s) \tag{4.3}$$

where

$$[\boldsymbol{\varepsilon}(\omega, \mathbf{r}_s)]_k^* = \varepsilon(\mathbf{r}_k, \omega, \mathbf{r}_s) \tag{4.4}$$

and $\odot$ represent element-wise or Hadamard multiplication. The conjugation in (4.4) is due to the Hermitian transpose of the array response vector in the derivation of (3.11). Replacing $\mathbf{a}(\omega, \mathbf{r}_s)$ in (3.12) and (3.16) with (4.3) yields

$$\begin{aligned} \hat{\mathbf{d}}(\psi, \omega, \mathbf{r}_s) &= \hat{\mathbf{a}}(\omega, \mathbf{r}_s) \otimes \boldsymbol{\psi} \otimes \mathbf{e}(\omega) \\ &= (\boldsymbol{\varepsilon}(\omega, \mathbf{r}_s) \otimes \mathbf{1}_{NL}) \odot \mathbf{d}(\psi, \omega, \mathbf{r}_s) \end{aligned} \tag{4.5}$$

for the time domain design formulation, and

$$\begin{aligned} \hat{\mathbf{d}}_f(\psi, \omega, \mathbf{r}_s) &= \hat{\mathbf{a}}(\omega, \mathbf{r}_s) \otimes \boldsymbol{\psi} \\ &= (\boldsymbol{\varepsilon}(\omega, \mathbf{r}_s) \otimes \mathbf{1}_N) \odot \mathbf{d}_f(\psi, \omega, \mathbf{r}_s) \end{aligned} \tag{4.6}$$

for the frequency domain design formulation, where $\mathbf{1}$ is a column vector with all unity elements and its subscript denotes its length. Note that both (4.5) and (4.6) have similar forms and thus from here onwards, only the time domain formulation will be discussed as the frequency domain formulation follows similarly.

The critical equation for the beamformer design formulations in Chapter 3 stems from the absolute error squared $|\xi(\psi, \omega, \mathbf{r}_s)|^2$ which exists in both the weighted LS and TLS formulations. Note that at this point, farfield sources are not assumed yet, and thus the dependency is still on $\mathbf{r}_s$ rather than on ϕ_s alone. Suppose that now, the array response vector (4.5) with the error model is used in (3.28), then the matrix $\mathbf{Q}(\psi, \omega, \mathbf{r}_s)$ becomes

$$\begin{aligned} \mathbf{Q}(\psi, \omega, \mathbf{r}_s) &= \hat{\mathbf{Q}}(\psi, \omega, \mathbf{r}_s) \\ &= \hat{\mathbf{d}}(\psi, \omega, \mathbf{r}_s) \hat{\mathbf{d}}^{\mathrm{H}}(\psi, \omega, \mathbf{r}_s) \\ &= \left(\left(\boldsymbol{\varepsilon}(\omega, \mathbf{r}_s) \boldsymbol{\varepsilon}^{\mathrm{H}}(\omega, \mathbf{r}_s) \right) \otimes \mathbf{1}_{NL} \mathbf{1}_{NL}^{\mathrm{T}} \right) \odot \mathbf{Q}(\psi, \omega, \mathbf{r}_s) \end{aligned} \tag{4.7}$$

and the vector $\mathbf{q}(\psi, \omega, \mathbf{r}_s)$ becomes

$$\begin{aligned}\mathbf{q}(\psi, \omega, \mathbf{r}_s) &= \hat{\mathbf{q}}(\psi, \omega, \mathbf{r}_s) \\ &= \hat{\mathbf{d}}(\psi, \omega, \mathbf{r}_s) B_d(\psi, \omega, \phi_s) \\ &= (\boldsymbol{\varepsilon}(\omega, \mathbf{r}_s) \otimes \mathbf{1}_{NL}) \odot \mathbf{q}(\psi, \omega, \mathbf{r}_s). \end{aligned} \tag{4.8}$$

Note that the sensor gain and phase errors can be considered as random variables and it is the error vector $\boldsymbol{\varepsilon}(\omega, \mathbf{r}_s)$ that is of interest. Let

$$\mathbf{E}(\omega, \mathbf{r}_s) = \boldsymbol{\varepsilon}(\omega, \mathbf{r}_s) \boldsymbol{\varepsilon}^{\mathrm{H}}(\omega, \mathbf{r}_s) \tag{4.9}$$

and suppose we want to optimise the mean performance by using the gain and phase probability density functions (PDFs) as the weights for the weighted sum of cost functions for all feasible sensors, i.e.

$$\bar{\mathbf{E}}(\omega, \mathbf{r}_s) = \mathbb{E}\{\mathbf{E}(\omega, \mathbf{r}_s)\} = \int ... \int \mathbf{E}(\omega, \mathbf{r}_s) f_{E_1,...,E_K}(\varepsilon_1, ..., \varepsilon_K) d(\varepsilon_1, ..., \varepsilon_K) \tag{4.10}$$

$$\bar{\varepsilon}(\omega, \mathbf{r}_s) = \mathbb{E}\{\boldsymbol{\varepsilon}(\omega, \mathbf{r}_s)\} = \int ... \int \boldsymbol{\varepsilon}(\omega, \mathbf{r}_s) f_{E_1,...,E_K}(\varepsilon_1, ..., \varepsilon_K) d(\varepsilon_1, ..., \varepsilon_K) \tag{4.11}$$

where $f_{E_1,...,E_K}(\varepsilon_1, ..., \varepsilon_K)$ is the joint PDFs for all the sensor's errors. From now on, the dependencies $(\omega, \mathbf{r}_s)$ is dropped from $\boldsymbol{\varepsilon}$ for notational convenience and their dependencies are understood from the context, and the k^{th} element of the error vector $\boldsymbol{\varepsilon}$ is simply denoted by ε_k. Assuming independence between errors from different sensors, then

$$[\bar{\varepsilon}(\omega, \mathbf{r}_s)]_k^* = \int \varepsilon_k f_{E_k}(\varepsilon_k) d(\varepsilon_k) \tag{4.12}$$

where $f_{E_k}(\varepsilon_k)$ is the PDF of the k^{th} sensor's error. The $(k_1, k_2)^{th}$ element (for $k_1 \neq k_2$) in the matrix $\bar{\mathbf{E}}(\omega, \mathbf{r}_s)$ is given by

$$\begin{aligned}\left[\bar{\mathbf{E}}(\omega, \mathbf{r}_s)\right]_{k_1,k_2}^* &= \int \int \varepsilon_{k_1} \varepsilon_{k_2}^* f_{E_{k_1}}(\varepsilon_{k_1}) f_{E_{k_2}}(\varepsilon_{k_2}) d(\varepsilon_{k_1}) d(\varepsilon_{k_2}) \\ &= \left(\int \varepsilon_{k_1} f_{E_{k_1}}(\varepsilon_{k_1}) d(\varepsilon_{k_1})\right) \left(\int \varepsilon_{k_2}^* f_{E_{k_2}}(\varepsilon_{k_2}) d(\varepsilon_{k_2})\right) \end{aligned} \tag{4.13}$$

and for $k_1 = k_2$ (diagonal elements),

$$\left[\bar{\mathbf{E}}(\omega, \mathbf{r}_s)\right]_{k_1,k_2} = \int |\varepsilon_{k_1}|^2 f_{k_1}(\varepsilon_{k_1}) d(\varepsilon_{k_1}) = \sigma_k^2 \tag{4.14}$$

where σ_k^2 is the second moment of the gain random variable. Let

$$\boldsymbol{\sigma} = \begin{bmatrix} \sigma_1^2 & 0 & 0 \\ 0 & \ddots & 0 \\ 0 & 0 & \sigma_K^2 \end{bmatrix}, \tag{4.15}$$

the matrix $\bar{\mathbf{E}}(\omega, \mathbf{r}_s)$ can be written as

$$\bar{\mathbf{E}}\left(\omega, \mathbf{r}_s\right) = \left(\bar{\varepsilon}\left(\omega, \mathbf{r}_s\right) \bar{\varepsilon}^{\mathrm{H}}\left(\omega, \mathbf{r}_s\right)\right) \odot \left(\mathbf{1}_K \mathbf{1}_K^{\mathrm{T}} - \mathbf{I}_K\right) + \boldsymbol{\sigma} \tag{4.16}$$

where $\mathbf{I}_K$ is $K \times K$ identity matrix. Hence, taking the expectation or mean of the absolute error squared results in

$$\mathbb{E}\left\{\left|\xi\left(\psi, \omega, \mathbf{r}_s\right)\right|^2\right\} = \mathbf{w}^{\mathrm{H}} \bar{\mathbf{Q}}\left(\psi, \omega, \mathbf{r}_s\right) \mathbf{w} - 2\mathrm{Re}\left\{\bar{\mathbf{q}}^{\mathrm{H}}\left(\psi, \omega, \mathbf{r}_s\right) \mathbf{w}\right\} + \left|B_d\left(\psi, \omega, \phi_s\right)\right|^2 \tag{4.17}$$

where

$$\bar{\mathbf{Q}}\left(\psi, \omega, \mathbf{r}_s\right) = \bar{\mathbf{E}}_{(m)}\left(\omega, \mathbf{r}_s\right) \odot \mathbf{Q}\left(\psi, \omega, \mathbf{r}_s\right), \tag{4.18}$$

$$\bar{\mathbf{E}}_{(m)}\left(\omega, \mathbf{r}_s\right) = \bar{\mathbf{E}}\left(\omega, \mathbf{r}_s\right) \otimes \mathbf{1}_{NL} \mathbf{1}_{NL}^{\mathrm{T}}, \tag{4.19}$$

$$\bar{\mathbf{q}}\left(\psi, \omega, \mathbf{r}_s\right) = \bar{\boldsymbol{\varepsilon}}_{(m)}\left(\omega, \mathbf{r}_s\right) \odot \mathbf{q}\left(\psi, \omega, \mathbf{r}_s\right), \tag{4.20}$$

$$\bar{\boldsymbol{\varepsilon}}_{(m)}\left(\omega, \mathbf{r}_s\right) = \bar{\boldsymbol{\varepsilon}}\left(\omega, \mathbf{r}_s\right) \otimes \mathbf{1}_{NL}, \tag{4.21}$$

and the subscript (m) denotes multiplicative error. If the gain and phase errors are assumed to be independent, (4.12) can be simplified into

$$\begin{aligned} \left[\bar{\varepsilon}(\omega, \mathbf{r}_s)\right]_k^* &= \int\int \varepsilon_k^{(\rho)} \exp\left(j\varepsilon_k^{(\gamma)}\right) f_{E_k^{(\rho)}}\left(\varepsilon_k^{(\rho)}\right) f_{E_k^{(\gamma)}}\left(\varepsilon_k^{(\gamma)}\right) d\left(\varepsilon_k^{(\rho)}\right) d\left(\varepsilon_k^{(\gamma)}\right) \\ &= \left(\int \varepsilon_k^{(\rho)} f_{E_k^{(\rho)}}\left(\varepsilon_k^{(\rho)}\right) d\left(\varepsilon_k^{(\rho)}\right)\right) \left(\int \cos\left(\varepsilon_k^{(\gamma)}\right) f_{E_k^{(\gamma)}}\left(\varepsilon_k^{(\gamma)}\right) d\left(\varepsilon_k^{(\gamma)}\right)\right. \\ &\qquad \left. + j \int \sin\left(\varepsilon_k^{(\gamma)}\right) f_{E_k^{(\gamma)}}\left(\varepsilon_k^{(\gamma)}\right) d\left(\varepsilon_k^{(\gamma)}\right)\right) \end{aligned} \tag{4.22}$$

and therefore,

$$\bar{\boldsymbol{\varepsilon}}(\omega, \mathbf{r}_s) = \bar{\boldsymbol{\varepsilon}}_\rho \odot \left(\bar{\boldsymbol{\varepsilon}}_\gamma^c + j\bar{\boldsymbol{\varepsilon}}_\gamma^s\right) \tag{4.23}$$

where

$$\left[\bar{\boldsymbol{\varepsilon}}_\rho\right]_k = \int \varepsilon_k^{(\rho)} f_{E_k^{(\rho)}}\left(\varepsilon_k^{(\rho)}\right) d\left(\varepsilon_k^{(\rho)}\right), \tag{4.24}$$

$$\left[\bar{\boldsymbol{\varepsilon}}_\gamma^c\right]_k = \int \cos\left(\varepsilon_k^{(\gamma)}\right) f_{E_k^{(\gamma)}}\left(\varepsilon_k^{(\gamma)}\right) d\left(\varepsilon_k^{(\gamma)}\right), \tag{4.25}$$

$$\left[\bar{\boldsymbol{\varepsilon}}_\gamma^s\right]_k = \int \sin\left(\varepsilon_k^{(\gamma)}\right) f_{E_k^{(\gamma)}}\left(\varepsilon_k^{(\gamma)}\right) d\left(\varepsilon_k^{(\gamma)}\right), \tag{4.26}$$

with $f_{E_k^{(\rho)}}\left(\varepsilon_k^{(\rho)}\right)$ and $f_{E_k^{(\gamma)}}\left(\varepsilon_k^{(\gamma)}\right)$ the PDFs of the gain and phase errors of the k^{th} sensor. In [54, 65, 79], it is shown that stochastic error modelling with multiplicative errors is also useful for modelling errors such as mismatch between array elements, errors in sensor positions and error in presumed source positions.

4.2.2 Additive error

Instead of multiplicative errors, suppose the sensor's errors are additive due to, for example, source spreading or local scattering [80], i.e.

$$\hat{\mathbf{a}}(\omega, \mathbf{r}_s) = \boldsymbol{\varepsilon}(\omega, \mathbf{r}_s) + \mathbf{a}(\omega, \mathbf{r}_s). \tag{4.27}$$

Then, following the same procedure discussed in Section 4.2.1, it can be derived that

$$\begin{aligned}
\hat{\mathbf{Q}}(\psi, \omega, \mathbf{r}_s) &= \hat{\mathbf{d}}(\psi, \omega, \mathbf{r}_s)\hat{\mathbf{d}}^{\mathrm{H}}(\psi, \omega, \mathbf{r}_s) \\
&= (\boldsymbol{\varepsilon}(\omega, \mathbf{r}_s) \otimes \boldsymbol{\psi} \otimes \mathbf{e}(\omega) + \mathbf{d}(\psi, \omega, \mathbf{r}_s)) \\
&\qquad \times (\boldsymbol{\varepsilon}(\omega, \mathbf{r}_s) \otimes \boldsymbol{\psi} \otimes \mathbf{e}(\omega) + \mathbf{d}(\psi, \omega, \mathbf{r}_s))^{\mathrm{H}} \\
&= \mathbf{Q}(\psi, \omega, \mathbf{r}_s) + \big(\boldsymbol{\varepsilon}(\omega, \mathbf{r}_s)\boldsymbol{\varepsilon}^{\mathrm{H}}(\omega, \mathbf{r}_s) + \boldsymbol{\varepsilon}(\omega, \mathbf{r}_s)\mathbf{a}^{\mathrm{H}}(\omega, \mathbf{r}_s) \\
&\qquad + \mathbf{a}(\omega, \mathbf{r}_s)\boldsymbol{\varepsilon}^{\mathrm{H}}(\omega, \mathbf{r}_s)\big) \otimes \mathbf{U}(\psi, \omega)
\end{aligned} \tag{4.28}$$

and

$$\begin{aligned}
\hat{\mathbf{q}}(\psi, \omega, \mathbf{r}_s) &= \hat{\mathbf{d}}(\psi, \omega, \mathbf{r}_s)B_d(\psi, \omega, \phi_s) \\
&= (\boldsymbol{\varepsilon}(\omega, \mathbf{r}_s) \otimes \boldsymbol{\psi} \otimes \mathbf{e}(\omega) + \mathbf{d}(\psi, \omega, \mathbf{r}_s))\, B_d(\psi, \omega, \phi_s) \\
&= \mathbf{q}(\psi, \omega, \mathbf{r}_s) + \boldsymbol{\varepsilon}(\omega, \mathbf{r}_s) \otimes \mathbf{u}(\psi, \omega)B_d(\psi, \omega, \phi_s)
\end{aligned} \tag{4.29}$$

where $\mathbf{U}(\psi, \omega) = \mathbf{u}(\psi, \omega)\mathbf{u}^{\mathrm{H}}(\psi, \omega)$ and $\mathbf{u}(\psi, \omega) = \boldsymbol{\psi} \otimes \mathbf{e}(\omega)$. Following the same procedure to optimise the mean performance as in Section 4.2.1 yields

$$\bar{\mathbf{Q}}(\psi, \omega, \mathbf{r}_s) = \mathbf{Q}(\psi, \omega, \mathbf{r}_s) + \bar{\mathbf{E}}_{(a)}(\psi, \omega, \mathbf{r}_s), \tag{4.30}$$

$$\bar{\mathbf{q}}(\psi, \omega, \mathbf{r}_s) = \mathbf{q}(\psi, \omega, \mathbf{r}_s) + \bar{\boldsymbol{\varepsilon}}_{(a)}(\psi, \omega, \mathbf{r}_s), \tag{4.31}$$

where

$$\bar{\mathbf{E}}_{(a)}(\psi, \omega, \mathbf{r}_s) = \big(\bar{\mathbf{E}}(\omega, \mathbf{r}_s) + \bar{\boldsymbol{\varepsilon}}(\omega, \mathbf{r}_s)\mathbf{a}^{\mathrm{H}}(\omega, \mathbf{r}_s) + \mathbf{a}(\omega, \mathbf{r}_s)\bar{\boldsymbol{\varepsilon}}^{\mathrm{H}}(\omega, \mathbf{r}_s)\big) \otimes \mathbf{U}(\psi, \omega), \tag{4.32}$$

$$\bar{\boldsymbol{\varepsilon}}_{(a)}(\psi, \omega, \mathbf{r}_s) = \bar{\boldsymbol{\varepsilon}}(\omega, \mathbf{r}_s) \otimes \mathbf{u}(\psi, \omega)B_d(\psi, \omega, \phi_s), \tag{4.33}$$

and the subscript (a) denotes additive error.

4.2.3 Multiplicative and additive error

A more general error model that covers both multiplicative and additive errors can be obtained by combining the derivations in Sections 4.2.1 and 4.2.2. The resulting array response vector with both multiplicative and additive errors becomes

$$\hat{\mathbf{a}}(\omega, \mathbf{r}_s) = \boldsymbol{\varepsilon}_{(m)}(\omega, \mathbf{r}_s) \odot \mathbf{a}(\omega, \mathbf{r}_s) + \boldsymbol{\varepsilon}_{(a)}(\omega, \mathbf{r}_s). \tag{4.34}$$

Following a similar procedure as in Sections 4.2.1 and 4.2.2, it can be shown that

$$\bar{\mathbf{Q}}(\psi, \omega, \mathbf{r}_s) = \bar{\mathbf{E}}_{(m)}(\omega, \mathbf{r}_s) \odot \mathbf{Q}(\psi, \omega, \mathbf{r}_s) + \bar{\mathbf{E}}_{(a)}(\psi, \omega, \mathbf{r}_s), \tag{4.35}$$

$$\bar{\mathbf{q}}(\psi, \omega, \mathbf{r}_s) = \bar{\boldsymbol{\varepsilon}}_{(m)}(\omega, \mathbf{r}_s)\mathbf{q}(\psi, \omega, \mathbf{r}_s) + \bar{\boldsymbol{\varepsilon}}_{(a)}(\psi, \omega, \mathbf{r}_s), \tag{4.36}$$

where $\bar{\mathbf{E}}_{(m)}(\omega, \mathbf{r}_s)$, $\bar{\boldsymbol{\varepsilon}}_{(m)}(\omega, \mathbf{r}_s)$, $\bar{\mathbf{E}}_{(a)}(\psi, \omega, \mathbf{r}_s)$ and $\bar{\boldsymbol{\varepsilon}}_{(a)}(\psi, \omega, \mathbf{r}_s)$ are defined respectively in (4.19), (4.21), (4.32), and (4.33). It should be noted that although the subscripts (m) and (a) distinguish the multiplicative and additive errors, their derivations are essentially based on the derivations of $\bar{\mathbf{E}}(\omega, \mathbf{r}_s)$ in (4.10) and $\bar{\boldsymbol{\varepsilon}}(\omega, \mathbf{r}_s)$ in (4.11).

4.3 Robust formulation for SBBF design in the element space domain

Apart from providing a more meaningful quantification of practical models, this stochastic approach merges the error modelling into the design formulation itself. Hence, conventional weighted LS and weighted TLS design techniques, which are formulated for non-robust designs, can also be used directly in the proposed robust design method.

4.3.1 Weighted least squares formulation

Incorporating the error model in Section 4.2 into the weighted LS beamformer design formulation in (3.31) and assuming farfield sources, i.e. the dependency

on $\mathbf{r}_s$ becomes dependency on ϕ_s only. Let the new objective function be the weighted sum of mean absolute error squared, i.e.

$$\begin{aligned}\bar{J}_{LS} &= \int_{\Psi}\int_{\Omega}\int_{\Phi} V(\psi,\omega,\phi_s)\mathbb{E}\left\{\left|\xi(\psi,\omega,\phi_s)\right|^2\right\} d\phi_s d\omega d\psi \\ &= \mathbf{w}^{\mathrm{T}}\bar{\mathbf{Q}}\mathbf{w} - 2\mathrm{Re}\left\{\bar{\mathbf{q}}^{\mathrm{H}}\mathbf{w}\right\} + b \end{aligned} \tag{4.37}$$

where

$$\bar{\mathbf{Q}} = \int_{\Psi}\int_{\Omega}\int_{\Phi} V(\psi,\omega,\phi_s)\bar{\mathbf{Q}}(\psi,\omega,\phi_s)d\phi_s d\omega d\psi, \tag{4.38}$$

$$\bar{\mathbf{q}} = \int_{\Psi}\int_{\Omega}\int_{\Phi} V(\psi,\omega,\phi_s)\bar{\mathbf{q}}(\psi,\omega,\phi_s)d\phi_s d\omega d\psi. \tag{4.39}$$

The matrix $\bar{\mathbf{Q}}(\psi,\omega,\phi_s)$ and vector $\bar{\mathbf{q}}(\psi,\omega,\phi_s)$ used in (4.38) and (4.39) are as defined in Section 4.2, depending on the error model used, i.e. either as multiplicative error, additive error or both.

The design of the robust weighted LS steerable broadband beamformer can be achieved by minimising (4.37). Its analytical solution, which is similar to (3.37), is given by

$$\mathbf{w} = \left(\mathrm{Re}\left\{\bar{\mathbf{Q}}\right\}\right)^{-1}\mathrm{Re}\left\{\bar{\mathbf{q}}\right\}. \tag{4.40}$$

4.3.2 Total least squares eigenfilter formulation

As for the weighted TLS design formulation, let

$$A = \int_{\Psi}\int_{0}^{\pi}\int_{-\pi}^{\pi} V(\psi,\omega,\phi_s)\mathbb{E}\left\{\left|B(\tilde{\psi},\omega,\phi_s)\right|^2\right\} d\phi_s d\omega d\psi = \mathbf{w}^{\mathrm{H}}\bar{\mathbf{Q}}_T\mathbf{w}, \tag{4.41}$$

$$\bar{\mathbf{Q}}_T = \int_{\Psi}\int_{0}^{\pi}\int_{-\pi}^{\pi} V\left(\psi,\omega,\phi_s\right)\bar{\mathbf{Q}}\left(\psi,\omega,\phi_s\right)d\phi_s d\omega d\psi, \tag{4.42}$$

in (3.38), and define the new objective function as

$$\bar{J}_{TLS} = \int_{\Psi}\int_{\Omega}\int_{\Phi} V(\psi,\omega,\phi_s)\mathbb{E}\left\{\xi^2_{TLS}(\psi,\omega,\phi_s)\right\} d\phi_s d\omega d\psi. \tag{4.43}$$

Then, the design of the robust weighted TLS steerable broadband beamformer can be achieved by minimising (4.43), which can be solved similarly to that described in Section 3.4.2 by substituting $\mathbf{Q}_T = \bar{\mathbf{Q}}_T$, $\mathbf{Q} = \bar{\mathbf{Q}}$ and $\mathbf{q} = \bar{\mathbf{q}}$.

4.4 Design examples and discussions

4.4.1 Design specifications

In order to illustrate the robustness achieved by using the stochastic error model, a number of design examples are presented and compared with their corresponding non-robust design examples in Section 3.5. The same design specifications as listed in Tables 3.2 and 3.3, as well as the same performance assessment as defined in (3.56) and (3.55) are used for meaningful comparison. For the robust design, both the multiplicative-only error model and additive-only error model are used. The errors in all sensors are assumed to follow the same PDF model, which is independent of both frequency ω and azimuth angle ϕ_s, with the gain and phase error PDFs given by

$$f_{E_k^{(\rho)}}\left(\varepsilon_k^{(\rho)}\right) = \begin{cases} \mathcal{N}\left(1, 0.05\right) & , \varepsilon_k^{(\rho)} \geq 0 \\ 0 & , \text{otherwise} \end{cases} \tag{4.44}$$

$$f_{E_k^{(\gamma)}}\left(\varepsilon_k^{(\gamma)}\right) = \mathcal{U}\left(-0.05 \text{ rad}, 0.05 \text{ rad}\right) \tag{4.45}$$

where $\mathcal{N}(\cdot)$ is a Gaussian PDF and $\mathcal{U}(\cdot)$ is a Uniform PDF. Note that (4.44) is essentially a cropped Gaussian PDF. The same PDF model of (4.44) and (4.45) are used in both multiplicative-only and additive-only robust designs for comparison purpose.

4.4.2 Perturbation in sensors characteristics

In order to evaluate the robustness performance, the following perturbation model is introduced into all sensors. The ideal sensor response is assumed to be a bandpass filter with unity gain and linear phase shift within the spectral passband. This response is then modelled with a 50-tap FIR filter, which will introduce a phase delay into the sensor response. The ideal filter coefficients $b_r\left(k, l'\right)$ are then perturbed with a uniform random variable as in

$$\hat{b}_r\left(k, l'\right) \sim b_r\left(k, l'\right) + \mathcal{U}\left(-0.1, 0.1\right) \tag{4.46}$$

where $\hat{b}_r\left(k, l'\right)$ is the perturbed l'^{th} filter coefficient of the k^{th} sensor. Fig. 4.1 shows the perturbed sensor responses, where each line corresponds to the response

of each sensor. Here, it is noted that the perturbation model (4.46) is pessimistic relative to the actual sensor response from calibration graph provided by manufacturers. The reason that the model (4.46) is chosen is because it is simple and if the design is robust against such perturbations, then they most likely will be robust against the actual perturbations and mismatches in real sensors.

The performance error for the design examples with this perturbation is shown in Fig. 4.2, where each plot is averaged over 50 runs with the vertical bars representing one standard deviation. It is clear from this figure that robustness is achieved in the designs with the stochastic error model. The trade-off for achieving this robustness is the increased performance error relative to the ideal situation (without perturbation) as shown in Fig. 4.3. This trade-off is typical in any robust designs. A further highlight of the achieved robustness using the stochastic error model is illustrated in Figs. 4.4 and 4.5, where the DIs with perturbation for both non-robust and robust, LS and TLS designs are shown. From these figures, the robust designs successfully maintain their directivity in the presence of perturbations, unlike their non-robust counterparts.

4.4.3 Perturbation in sensor positions

The robustness achieved in the design examples is not limited to perturbation in the sensor characteristics, but also to other perturbations such as in the sensor positions. Errors in the sensor position cause variations in gain and phase delay of the signal arriving at the sensor, which fit readily into the multiplicative error model.

In this subsection, the same design examples are evaluated in the presence of errors in the sensor positions. The sensor positions are perturbed within a circular region (with the radius given by the Gaussian distribution $\mathcal{N}\left(0,(0.001)^2\right)$) around their nominal values, and the perturbed positions (in $x-y$ coordinate) are given by

$$\hat{\mathbf{r}}_k \sim \left[x_k + \mathcal{N}\left(0,(0.001)^2\right)\cos\left(\mathcal{U}\left(0,\pi\right)\right), y_k + \mathcal{N}\left(0,(0.001)^2\right)\sin\left(\mathcal{U}\left(0,\pi\right)\right)\right] \tag{4.47}$$

where $[x_k, y_k]$ is the nominal position of the k^{th} sensor in $x-y$ coordinate. The

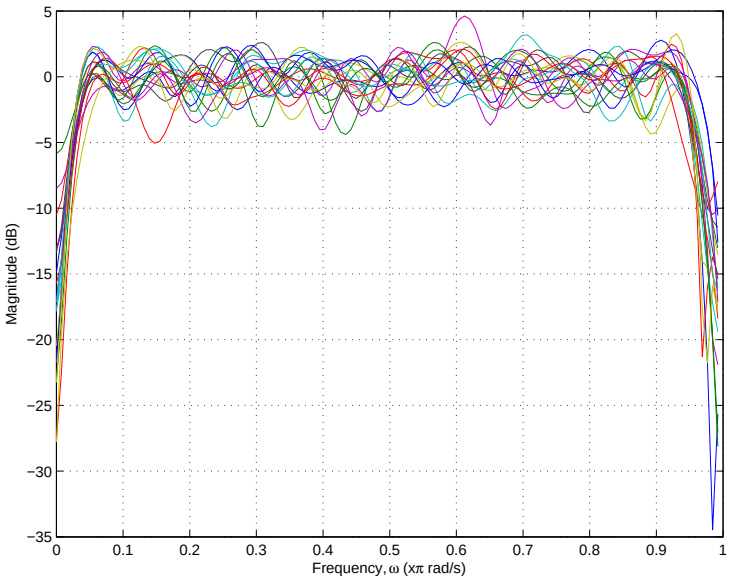

(a) Magnitude response.

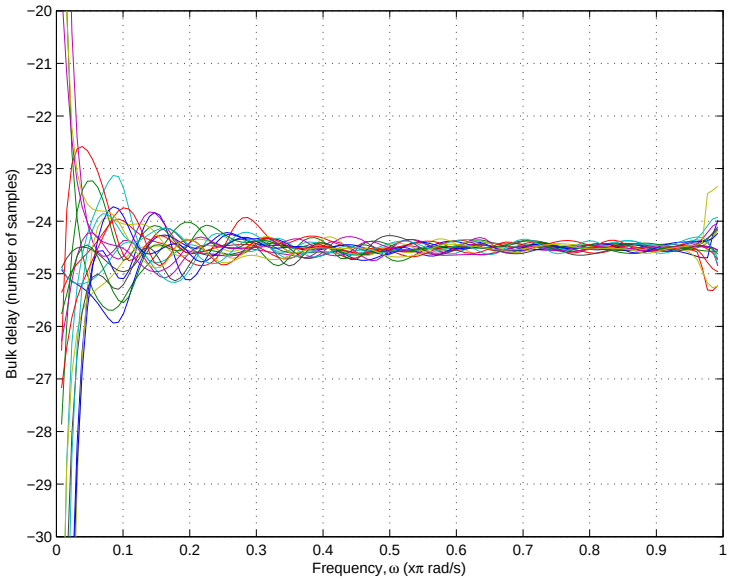

(b) Phase delay.

Figure 4.1: Perturbed sensor responses.

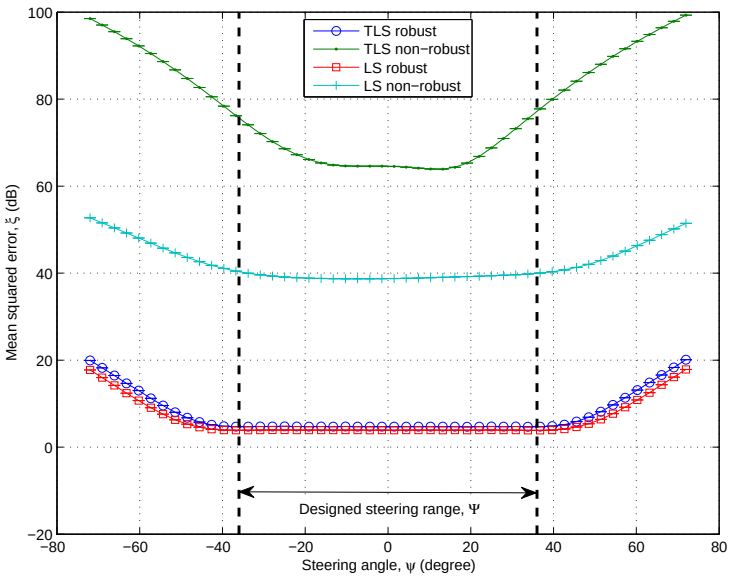

Figure 4.2: Averaged performance error with perturbation in sensor characteristics for non-robust and robust multiplicative-only designs .

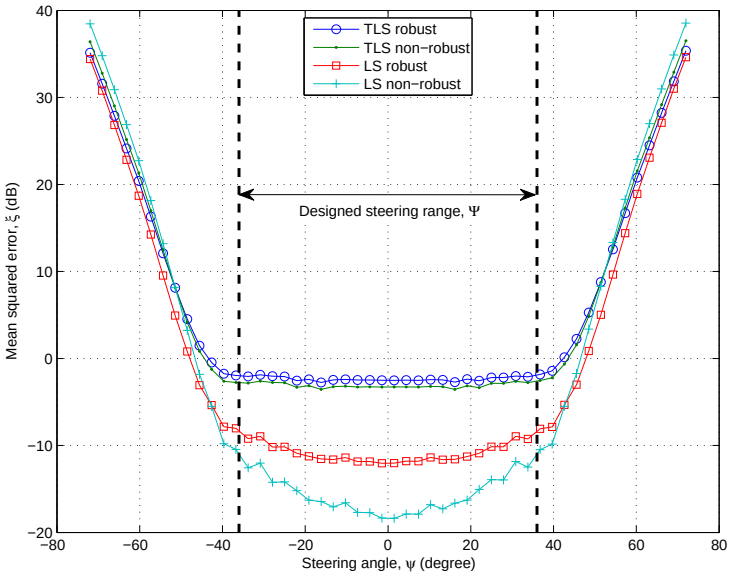

Figure 4.3: Performance error without perturbation for non-robust and robust multiplicative-only designs.

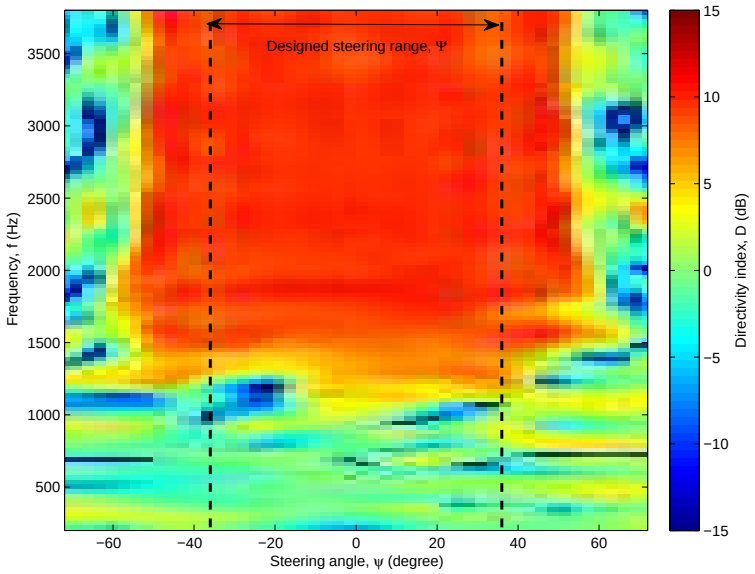

(a) LS designs.

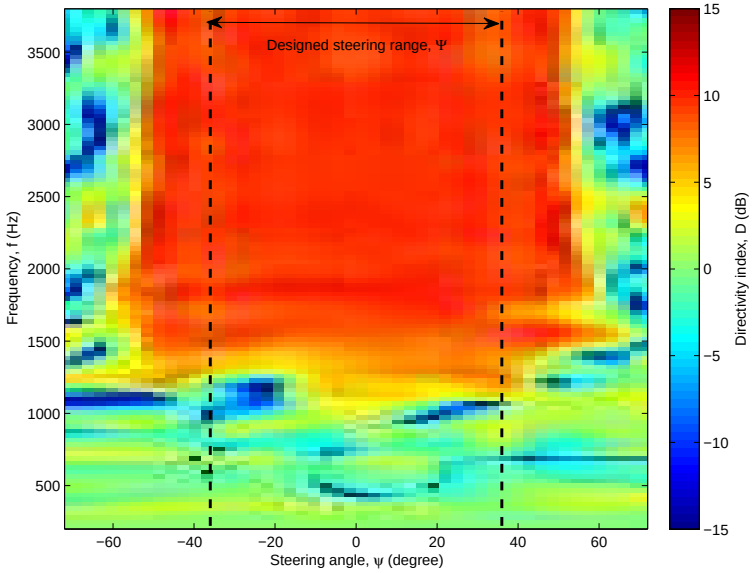

(b) TLS designs.

Figure 4.4: DIs with perturbation in sensor characteristics for non-robust LS and TLS designs.

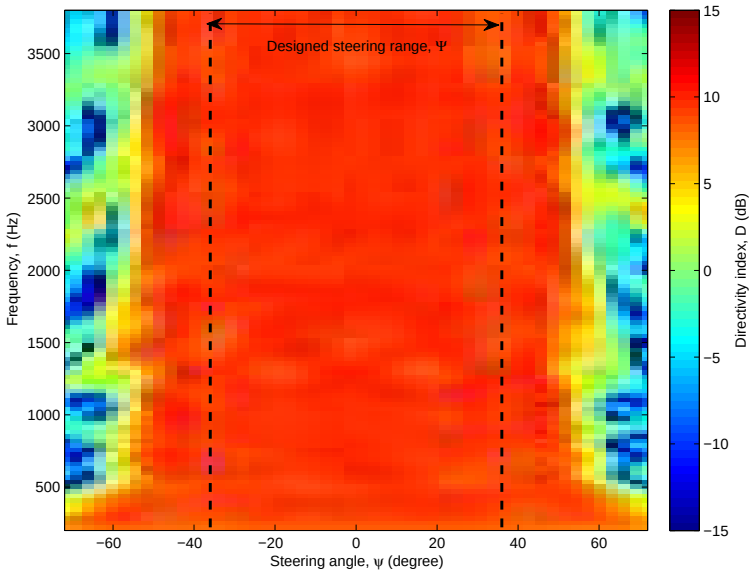

(a) LS designs.

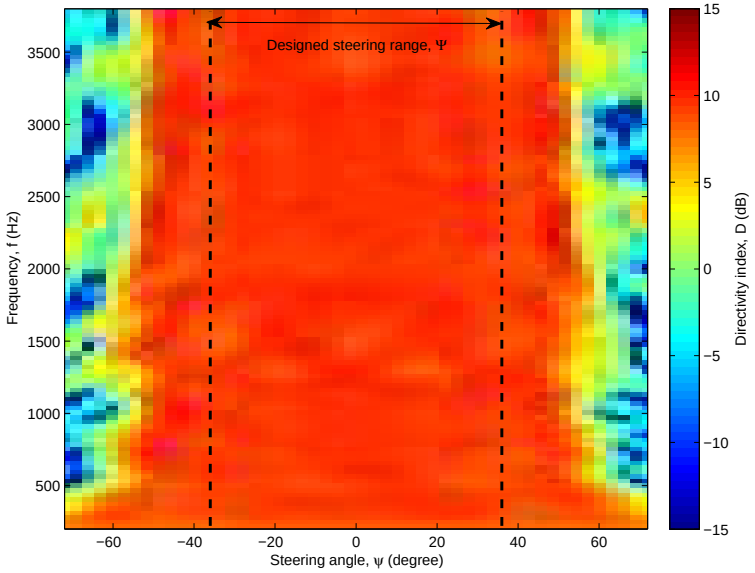

(b) TLS designs.

Figure 4.5: DIs with perturbation in sensor characteristics for robust multiplicative-only LS and TLS designs.

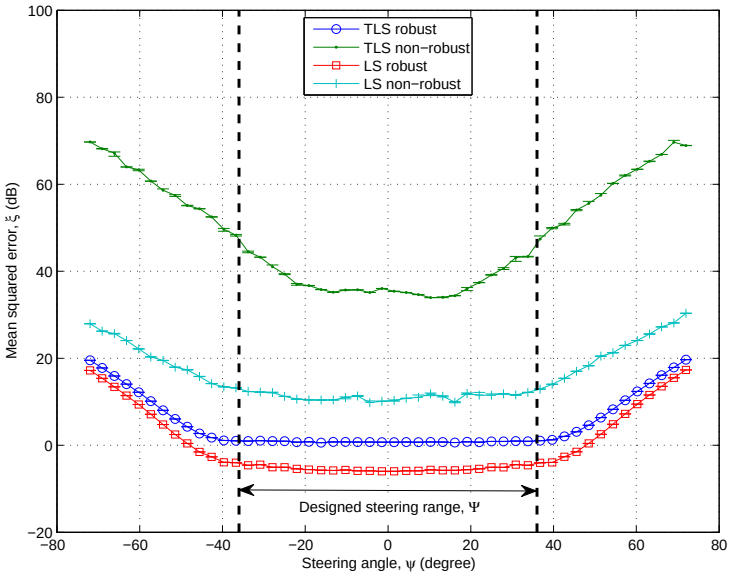

Figure 4.6: Averaged performance error with perturbation in sensor positions for non-robust and robust multiplicative-only designs.

averaged performance error for the robust and non-robust designs are shown in Fig. 4.6. Again, each plot is averaged over 50 runs with the vertical bars representing one standard deviation. The robustness in the designs are indicated by the low performance error as well as the small standard deviation. It is evident from the figure that the robust designs still work under the introduced perturbations in the sensor positions.

4.4.4 Perturbation due to local scattering

In order to evaluate the design examples against additive error model, errors due to local scattering is considered [80]. In this perturbation model, additional propagation paths from signal source to the sensor array are present in addition to the direct line-of-sight propagation path as shown in Fig. 4.7. The array element response with such perturbation model is given by

$$\hat{a}\left(\mathbf{r}_k, \omega, \mathbf{r}_s\right) = a\left(\mathbf{r}_k, \omega, \mathbf{r}_s\right) + \frac{1}{L}\sum_{i=1}^{L} \rho^{(i)} a\left(\mathbf{r}_k, \omega, \mathbf{r}_s^{(i)}\right) \tag{4.48}$$

where $\mathbf{r}_s^{(i)} = \left(r_s, \phi_s + \phi^{(i)}\right)$, L is the number of propagation paths, $\phi^{(i)}$ is the variation in angle of arrival and $\rho^{(i)}$ is the variation in gain of the impinging

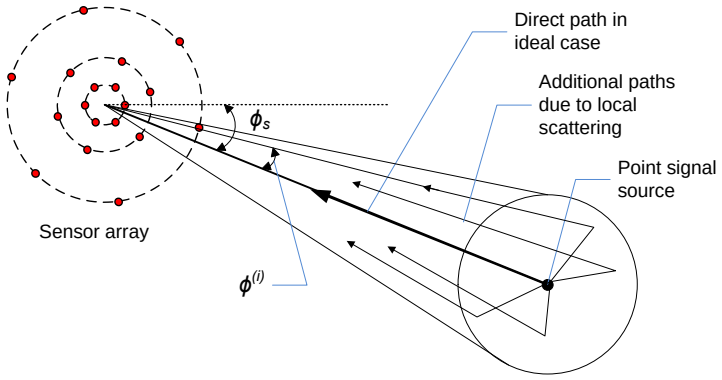

Figure 4.7: Model used for perturbation due to local scattering.

signal due to local scattering. Both the variations $\phi^{(i)}$ and $\rho^{(i)}$ are taken to be

$$\phi^{(i)} \sim \mathcal{U}\left(-\frac{\pi}{9}, \frac{\pi}{9}\right) \tag{4.49}$$

$$\rho^{(i)} \sim \text{Rayleigh}\,(0.01) \tag{4.50}$$

where Rayleigh $(\cdot)$ is a Rayleigh PDF.

Fig. 4.8 shows the averaged performance error for the design examples with such perturbation. Again, each plot is averaged over 50 runs with the vertical bars representing one standard deviation. As expected, the robust additive-only designs have lower performance error as compared to their non-robust counterparts in the presence of local scattering perturbation. Similarly, the trade-off for achieving this robustness is the increased performance error in the absence of perturbation as shown in Fig. 4.9. Figs. 4.10 and 4.11 show the DIs with local scattering perturbation for the non-robust and robust additive-only designs, respectively. It is evident that the DIs for the robust additive-only designs are maintained in the presence of local scattering perturbation.

4.5 Conclusions

In conclusion, stochastic error models offer a nice approach for modelling real world perturbations and errors into the robust beamformers design formulation. This is because in this formulation, errors are modelled as random variables, which is sensible since real world perturbations can be considered as random. Hence, this error model can capture the stochastic properties of the errors to be

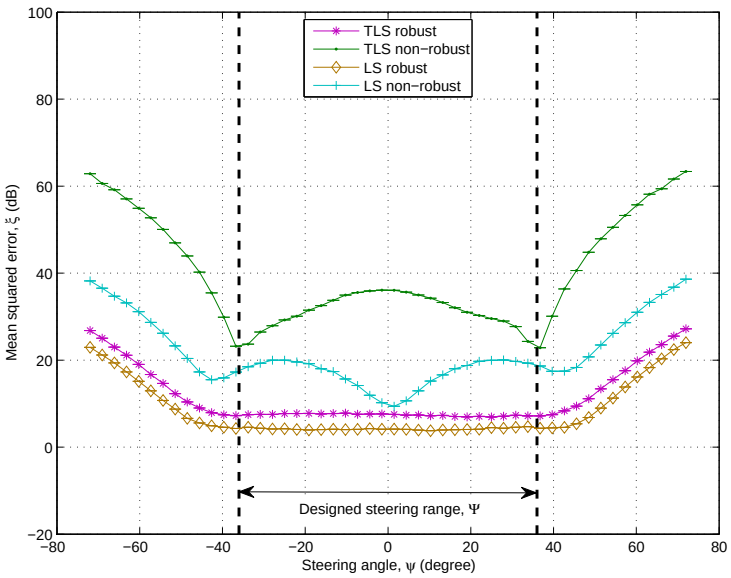

Figure 4.8: Average performance error with local scattering perturbation for non-robust and robust additive-only designs.

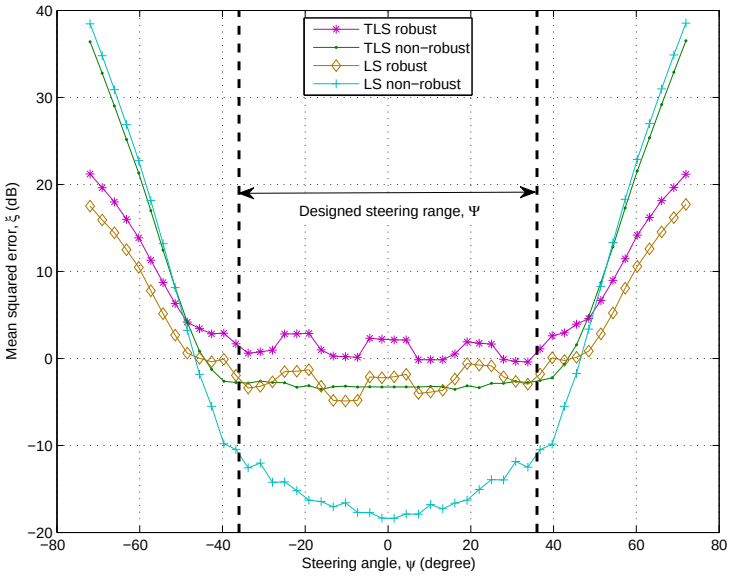

Figure 4.9: Performance error without perturbation for non-robust and robust additive-only designs.

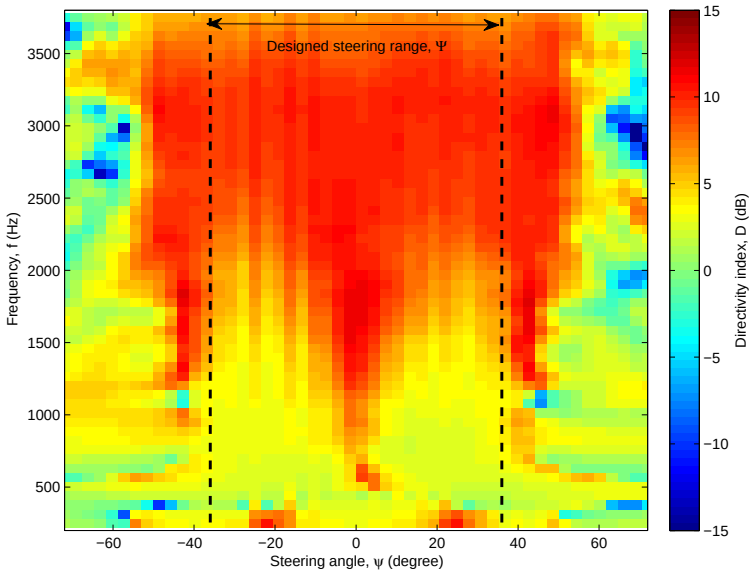

(a) LS designs.

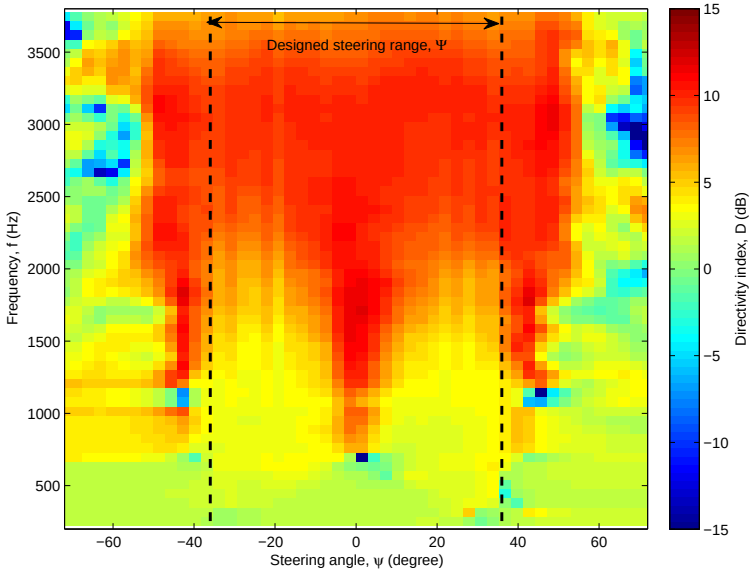

(b) TLS designs.

Figure 4.10: DIs with local scattering perturbation for non-robust LS and TLS designs.

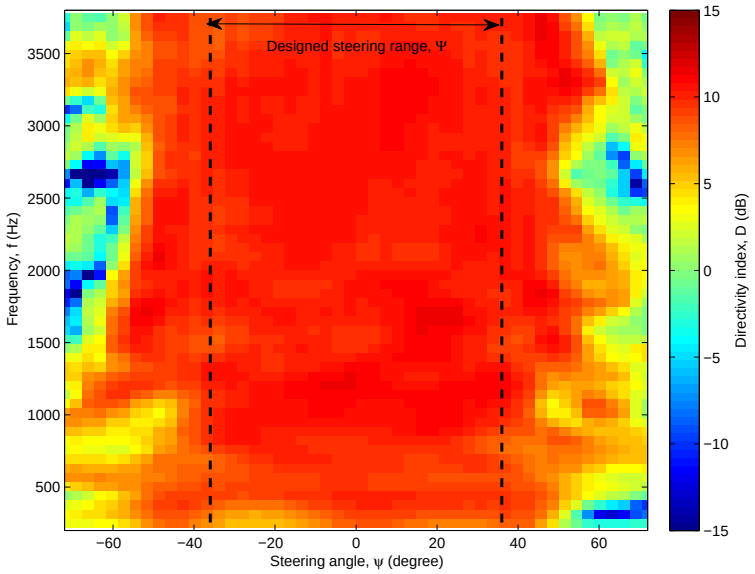

(a) LS designs.

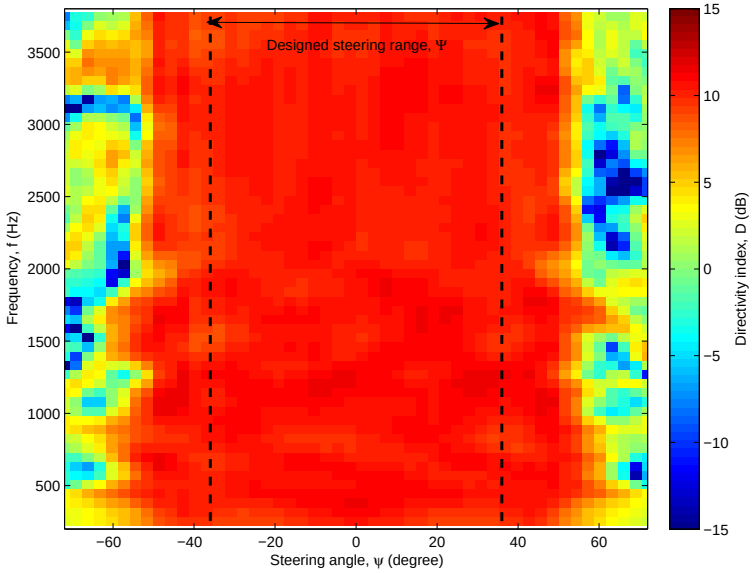

(b) TLS designs.

Figure 4.11: DIs with local scattering perturbation for robust additive-only LS and TLS designs.

integrated into the design model, where the errors are weighted by their rate of occurrence or PDFs.

The design optimisation studied in this chapter provides a good way to achieve robustness in the sense that the designs are optimised with respect to the mean error, where the errors happen most frequently. This provide a fair balance between robustness and performance as it is not as pessimistic as the method of optimising for the worst case error. Furthermore, the method of optimising for the mean performance effectively embeds the error model into the beamformer design models. Hence, the robust design formulations can be extended, modified and solved in similar ways as their non-robust counterparts.

In addition, as most practical errors can be translated into errors occurring during the sampling of the sensor output signal, they can be modelled as either multiplicative complex errors, additive complex error or both. This error modelling provides a better connection between the real world error and design model, unlike the WNG method where such connection is vague. Hence, a more quantitative robustness specification is possible with this error model.

Chapter 5

Mixed Nearfield-Farfield Broadband Beamformer

5.1 Introduction

The discussion on the formulation of beamformer design in the previous two chapters focuses only on steerable beamformer designs for either a nearfield or farfield source, and not their combination. The main-beam in those designs allows the spatial pass region to be steered around the azimuth plane, but not along the source radial distance. Regardless of the look direction of the main-beam, the source (possibly a moving source) need to always remains in either the nearfield (at a specific radial distance where it is designed for) or the farfield region, depending on the source model used for the design.

Although in some applications, such restriction may not be a significant problem, beamformers designed using either the nearfield source model or farfield source model (and not their combination) limit their source operating region to the model assumed. For instance, farfield beamformers cannot be used for nearfield sources and vice versa. Specifically, this differentiation is due to the deviation in the curvature of the impinging wavefront between a nearfield and a farfield source (see Fig. 5.1). The gain attenuations and phase delays of the array elements are thus different for a nearfield and a farfield source. These deviations, especially the phase delays, will cause the response to deviate from the desired

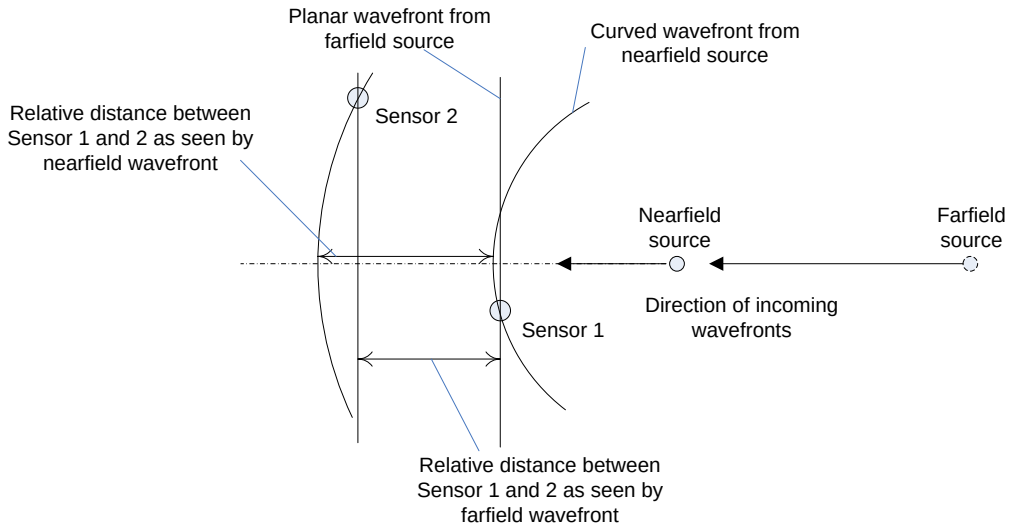

Figure 5.1: Difference between nearfield and farfield source model.

response, since the basic concept behind beamforming is built upon the relative phase delays between the array elements for a given source direction. Such deviation can be seen from Figs. 5.2 and 5.3 which clearly show that beamformers are not operable for the source models they are not designed for.

For all that, recent demands require broadband beamformers to be operable for both nearfield and farfield sources, or at least robust to variation in the source radial distance. In applications such as teleconferencing and audio surveillance, it is very likely that the acoustic source will be moving around, causing its radial distance r_s to change. Hence, beamformers for such applications need to be robust to such changes. Furthermore, if the beamformers are robust to a wide range of radial distance r_s (such as in mixed nearfield-farfield beamformers), then the speaker has more freedom to move in teleconferencing applications (or the surveillance area can be increased in audio surveillance applications). Besides, in mixed nearfield-farfield beamformers, it is no longer necessary to consider the condition that governs the validity of the farfield (or nearfield) model since there is no switching between the nearfield and farfield designs.

Mixed nearfield-farfield broadband beamformer design was first investigated in [81] where a weighted sum of a nearfield cost function and a farfield cost function is optimised. Doclo and Moonen [56] applied the same technique to a different design formulation to achieve the same characteristics. Although this method

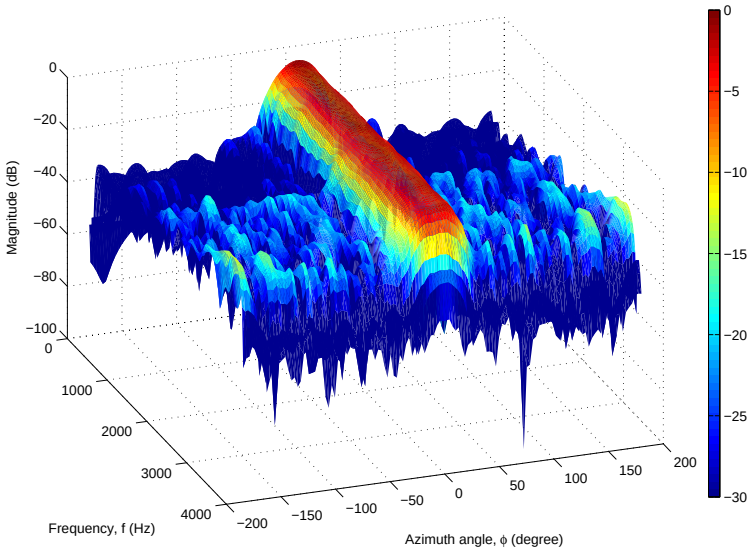

(a) Farfield source model.

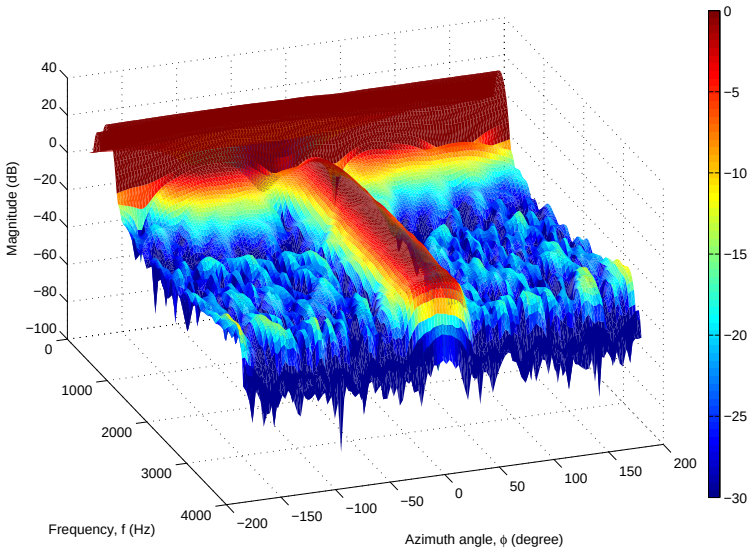

(b) Nearfield source model.

Figure 5.2: Farfield beamformer evaluated using farfield and nearfield source model.

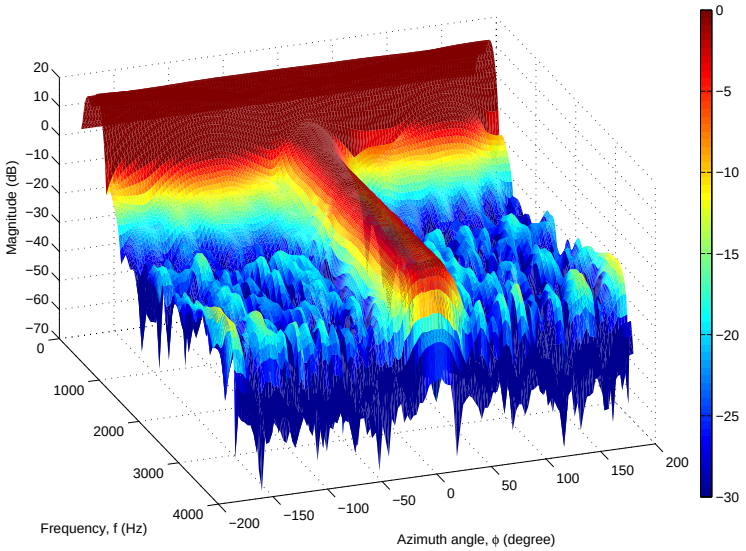

(a) Farfield source model.

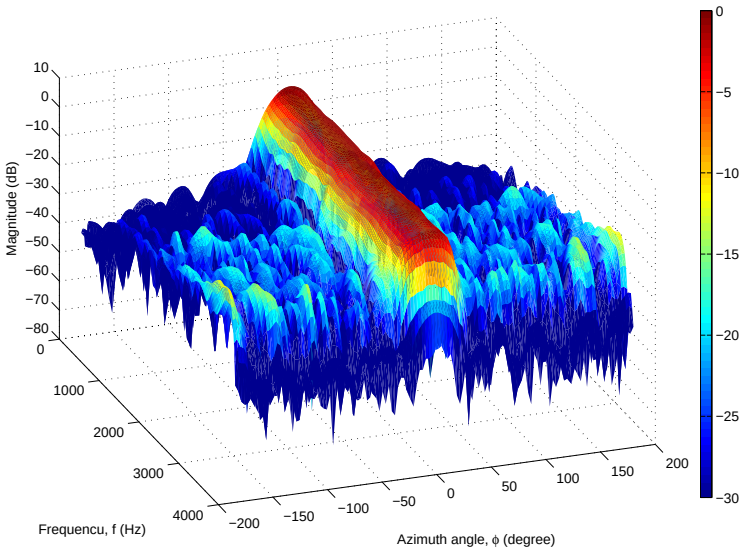

(b) Nearfield source model.

Figure 5.3: Nearfield beamformer evaluated using farfield and nearfield source model.

effectively mixes the nearfield and farfield model into a single design formulation, it is not robust in the sense that there is no deviation modelling in its formulation. Moreover, their main-beam is fixed and cannot be steered.

In this chapter, a weighted LS design formulation for steerable robust mixed nearfield-farfield broadband beamformers is proposed. The steerability context in this chapter is the same as the previous two chapters, i.e. the design formulation allows the spatial pass region to be steered around the azimuth plane. However, unlike the previous chapters, the design formulation in this chapter achieves beamformers that continues to work regardless of the source moving between the nearfield and farfield regions. In other words, this chapter presents a design formulation for beamformers with i) steerability of the main-beam around the azimuth dimension, ii) invariant response over a wide frequency range (broadband), iii) invariant response over a wide distance (covering both nearfield and farfield regions), and iv) robust against errors and perturbations. The proposed method extends the design formulation of steerable beamformers in Chapter 3 in a similar way as [56, 81] to accommodate for both nearfield and farfield sources at the same time. This allows the operability for both nearfield and farfield sources to be added on top of the steerability property. In addition, the robust formulation discussed in Chapter 4 is incorporated into the design formulation to achieve robustness against errors and perturbations.

This chapter is organised as follows. Section 5.2 discusses the proposed beamformer design formulation in weighted LS sense together with its robust design formulation. This is followed by design examples presented in Section 5.3 along with their performance evaluations. Lastly, conclusions are drawn in Section 5.4.

5.2 Mixed nearfield-farfield design formulation

5.2.1 Beamformer structure

The design formulation of a steerable mixed nearfield-farfield beamformer can be achieved by modifying the formulation in Chapter 3. Consider again the Farrow beamformer structure of Fig. 3.5 repeated in Fig. 5.4. Assuming ideal omni-

directional sensors, its normalised response to a nearfield source, with arbitrary planar array geometry, is given by

$$B\left(\tilde{\psi},\omega,r_s,\phi_s\right)=\sum_{k=0}^{K-1}\bar{a}\left(\mathbf{r}_k,\omega,r_s,\phi_s\right)\sum_{n=0}^{N-1}\tilde{\psi}^n\sum_{l=0}^{L-1}w_{k,n}\left(l\right)\exp\left(-i\omega T_S l\right) \tag{5.1}$$

where K is the number of sensors, $N-1$ is the order of the Farrow filter structure, L is the number of FIR taps, (r_s,ϕ_s) is the source position (expressed in terms of radial distance and azimuth angle to facilitate the formulation that follows), ω is the source signal angular frequency, and T_S is the sampling period. Note that (5.1) is similar to (3.5) in Chapter 3, except that a normalised array response $\bar{a}\left(\cdot\right)$ is used here to have a consistent response from both nearfield and farfield sources, relative to a common reference point. Let the origin of the coordinate system, located usually at the centre of gravity of the array, be the reference point. Hence, the normalised array response of the k^{th} element $\bar{a}\left(\mathbf{r}_k,\omega,r_s,\phi\right)$, relative to the reference point, is given by

$$\bar{a}\left(\mathbf{r}_k,\omega,r_s,\phi_s\right)=\frac{r}{d\left(\mathbf{r}_k,r_s,\phi_s\right)}\exp\left(j\frac{\omega}{c}\left(r-d\left(\mathbf{r}_k,r_s,\phi_s\right)\right)\right) \tag{5.2}$$

where c is the speed of the propagating wave and $d\left(\mathbf{r}_k,r_s,\phi_s\right)$ is the Cartesian distance between the source and the k^{th} sensor located at $\mathbf{r}_k=(r_k,\phi_k)$, given by

$$d_k\left(\mathbf{r}_k,r_s,\phi_s\right)=\sqrt{r_k^2+r_s^2-2r_k r_s\cos\left(\phi_s-\phi_k\right)}. \tag{5.3}$$

Equation (5.2) comes from (2.5) and is rewritten in a slightly different form to facilitate the discussion in this chapter. Define now

$$\mathbf{a}\left(\omega,r_s,\phi_s\right)=\left[\begin{array}{cccc}\bar{a}\left(\mathbf{r}_0,\omega,r_s,\phi_s\right) & ... & \bar{a}\left(\mathbf{r}_{K-1}\omega,r_s,\phi_s\right)\end{array}\right]^{\mathrm{H}}, \tag{5.4}$$

$$\mathbf{w}=\left[\begin{array}{ccc|c}w_{0,0}\left(0\right) & ... & w_{0,0}\left(L-1\right) & \\ w_{0,1}\left(0\right) & ... & w_{0,1}\left(L-1\right) & \cdots \\ \hline & w_{K-1,N-1}\left(0\right) & ... & w_{K-1,N-1}\left(L-1\right)\end{array}\right]^{\mathrm{T}}. \tag{5.5}$$

Equation (5.1) can be written compactly in matrix form as follows.

$$B\left(\tilde{\psi},\omega,r_s,\phi\right)=\mathbf{d}^{\mathrm{H}}\left(\psi,\omega,r_s,\phi_s\right)\mathbf{w} \tag{5.6}$$

where $\mathbf{d}\left(\psi,\omega,r_s,\phi_s\right)=\mathbf{a}\left(\omega,r_s,\phi_s\right)\otimes\tilde{\boldsymbol{\psi}}\otimes\mathbf{e}$, and both $\tilde{\boldsymbol{\psi}}$ and $\mathbf{e}$ are given respectively, by (3.7) and (3.8).

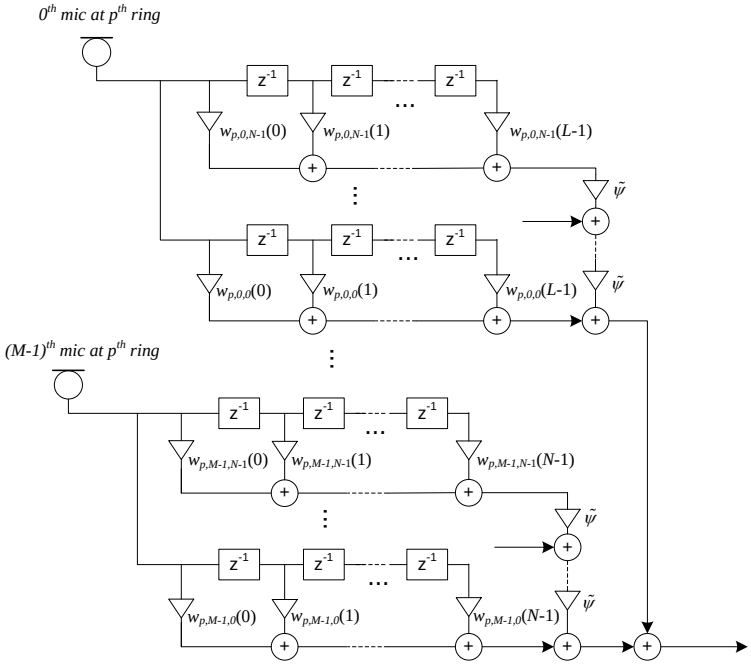

Figure 5.4: Time domain steerable broadband beamformer structure using Farrow structure.

5.2.2 Weighted least squares formulation

Defining the error function as the difference between the normalised beamformer response and the desired response as follows

$$\xi\left(\psi,\omega,r_s,\phi_s\right)=B\left(\tilde{\psi},\omega,r_s,\phi_s\right)-B_d\left(\psi,\omega,\phi_s\right) \tag{5.7}$$

where the desired beamformer response $B_d\left(\psi,\omega,\phi_s\right)$ is independent of r_s, the weighted LS design formulation is defined by

$$J_{LS}\left(\mathbf{w}\right)=\int_{\Psi}\int_{\Omega}\int_{\Phi}\int_{\mathcal{R}}V\left(\psi,\omega,r_s,\phi_s\right)\left|\xi\left(\psi,\omega,r_s,\phi_s\right)\right|^2 dr_s d\phi_s d\omega d\psi \tag{5.8}$$

where Ψ, Ω, Φ and $\mathcal{R}$ are, respectively, the steering, spectral, azimuthal and radial range of interest with $\mathcal{R}$ covering both nearfield and farfield distances. The purpose of the weighting function $V\left(\psi,\omega,r_s,\phi_s\right)$ is to control the approximation error over the design space. Following (5.6), (5.8) can be rewritten in matrix form as follows

$$J_{LS}\left(\mathbf{w}\right)=\mathbf{w}^{\mathrm{T}}\mathbf{Q}_{LS}\mathbf{w}-2\left(\mathrm{Re}\left\{\mathbf{q}_{LS}\right\}\right)^{\mathrm{T}}\mathbf{w}+b \tag{5.9}$$

where

$$\mathbf{Q}_{LS} = \int\int\int\int V(\psi,\omega,r_s,\phi_s)\,\mathbf{Q}(\psi,\omega,r_s,\phi_s)\,dr_s d\phi_s d\omega d\psi, \tag{5.10}$$

$$\mathbf{q}_{LS} = \int\int\int\int V(\psi,\omega,r_s,\phi_s)\,\mathbf{q}(\psi,\omega,r_s,\phi_s)\,dr_s d\phi_s d\omega d\psi, \tag{5.11}$$

$$b = \int\int\int\int V(\psi,\omega,r_s,\phi_s)\,|B_d(\psi,\omega,\phi_s)|^2\,dr_s d\phi_s d\omega d\psi, \tag{5.12}$$

and

$$\mathbf{Q}(\psi,\omega,r_s,\phi_s) = \mathbf{d}(\psi,\omega,r_s,\phi_s)\,\mathbf{d}^{\mathrm{H}}(\psi,\omega,r_s,\phi_s), \tag{5.13}$$

$$\mathbf{q}(\psi,\omega,r_s,\phi_s) = \mathbf{d}(\psi,\omega,r_s,\phi_s)\,B_d(\psi,\omega,\phi_s), \tag{5.14}$$

and the integration ranges have been omitted for notational convenience. Minimising (5.9) with respect to $\mathbf{w}$ gives the analytical solution

$$\mathbf{w} = \mathbf{Q}_{LS}^{-1}\mathrm{Re}\{\mathbf{q}_{LS}\}. \tag{5.15}$$

The non-steerable mixed nearfield-farfield beamformer with fixed main-beam as presented in [56, 81] is a special case of the proposed design formulation with a single steering direction, i.e. $\Psi = \{0^\circ\}$ and the Farrow filter structure has order $N - 1 = 0$.

5.2.3 Robust formulation

In order to achieve robustness in the design, the proposed design formulation can be converted seamlessly to a robust design formulation using the stochastic error model presented in Chapter 4. This can be done by first substituting (5.13) and (5.14) respectively into (4.35) and (4.36), which are repeated as (5.16) and (5.17) here for convenience.

$$\bar{\mathbf{Q}}(\psi,\omega,r_s,\phi) = \bar{\mathbf{E}}_{(m)}(\omega,r_s,\phi) \odot \mathbf{Q}(\psi,\omega,r_s,\phi), \tag{5.16}$$

$$\bar{\mathbf{q}}(\psi,\omega,r_s,\phi) = \bar{\boldsymbol{\varepsilon}}_{(m)}(\omega,r_s,\phi)\mathbf{q}(\psi,\omega,r_s,\phi). \tag{5.17}$$

The expectation of stochastic error model, captured in $\bar{\mathbf{E}}_{(m)}(\cdot)$ and $\bar{\boldsymbol{\varepsilon}}_{(m)}(\cdot)$ for multiplicative error model, essentially integrate the robustness property into the design formulation. They are given by (repeated from (4.19) and (4.21))

$$\bar{\mathbf{E}}_{(m)}(\omega, r_s, \phi) = \bar{\mathbf{E}}(\omega, r_s, \phi) \otimes \mathbf{1}_{NL}\mathbf{1}_{NL}^{\mathrm{T}}, \tag{5.18}$$

$$\bar{\boldsymbol{\varepsilon}}_{(m)}(\omega, r_s, \phi) = \bar{\boldsymbol{\varepsilon}}(\omega, r_s, \phi) \otimes \mathbf{1}_{NL}, \tag{5.19}$$

where

$$\bar{\mathbf{E}}(\omega, r_s, \phi) = \mathbb{E}\{\mathbf{E}(\omega, r_s, \phi)\} = \int ... \int \mathbf{E}(\omega, \mathbf{r}_s) f_{E_1,...,E_K}(\varepsilon_1, ..., \varepsilon_K) d(\varepsilon_1, ..., \varepsilon_K), \tag{5.20}$$

$$\bar{\varepsilon}(\omega, r_s, \phi) = \mathbb{E}\{\boldsymbol{\varepsilon}(\omega, r_s, \phi)\} = \int ... \int \boldsymbol{\varepsilon}(\omega, \mathbf{r}_s) f_{E_1,...,E_K}(\varepsilon_1, ..., \varepsilon_K) d(\varepsilon_1, ..., \varepsilon_K), \tag{5.21}$$

with the matrix $\mathbf{E}(\omega, \mathbf{r}_s)$ and vector $\boldsymbol{\varepsilon}(\omega, \mathbf{r}_s)$ modelling only the multiplicative error (see Section 4 for details). Next, (5.16) and (5.17) are used to replace $\mathbf{Q}(\psi, \omega, r_s, \phi_s)$ and $\mathbf{q}(\psi, \omega, r_s, \phi_s)$ in (5.10) and (5.11), which yield

$$\mathbf{Q}_{LS} = \int\int\int\int V(\psi, \omega, r_s, \phi_s) \bar{\mathbf{Q}}(\psi, \omega, r_s, \phi_s) \, dr_s d\phi_s d\omega d\psi, \tag{5.22}$$

$$\mathbf{q}_{LS} = \int\int\int\int V(\psi, \omega, r_s, \phi_s) \bar{\mathbf{q}}(\psi, \omega, r_s, \phi_s) \, dr_s d\phi_s d\omega d\psi. \tag{5.23}$$

Hence, solving for the beamformer weights $\mathbf{w}$ using (5.15) with (5.22) and (5.23) yields robust beamformers. Note that although the robust design is formulated only from the multiplicative error model, they can also be formulated in a similar way to utilise both the multiplicative and additive error model of Section 4.2.3.

5.3 Performance evaluations and discussions

5.3.1 Design specifications and evaluation quantities

In order to illustrate the proposed weighted LS design formulation, two design examples (one non-robust and one robust) are presented and evaluated. The array geometry used in these design examples is the 2D spiral arm (a type of multi-ring concentric) array geometry discussed in Section 3.2, with a total of $K = PM$ sensors, placed in P rings with M sensors per ring. The same design parameters listed in Tables 3.2 and 3.3 are used, with the additional parameter

of $\mathcal{R} \in [1, r_{max}]$m and $r_{max} = \{5, 50, 100\}$. Note that from the rule of thumb (2.11) and $c = 343\text{ms}^{-1}$, the nearfield-farfield boundaries for $f = 200$Hz and $f = 3800$Hz are at $r_s = 2.01$m and $r_s = 38.21$m, respectively.

In these examples, the sensors are assumed to be omni-directional microphones operating in air. For simplicity, the weighting functions are selected to be $V(\psi, \omega, r_s, \phi_s) = 1$. The desired beamformer response $B_d(\psi, \omega, \phi_s)$ is the same as (3.54). For the robust design, the same PDF model as (4.44) and (4.45) are used for the microphones' characteristics.

The designs are evaluated in term of their performance error. The performance error function, defined as

$$\xi_{LS}(\psi, r_s) = \int_{\Omega}\int_{\Phi} \left|\xi(\psi, \omega, r_s, \phi_s)\right|^2 d\phi_s d\omega, \tag{5.24}$$

is used to perform an overall assessment on the designs over their key design spaces ψ and r_s. In order to facilitate comparisons among the different designs, the performance error (5.24) averaged along ψ and r_s are used, i.e.

$$\xi_{LS}(r_s) = \int_{\Psi} \xi_{LS}(\psi, r_s)\, d\psi,, \tag{5.25}$$

$$\xi_{LS}(\psi) = \int_{\mathcal{R}} \xi_{LS}(\psi, r_s)\, dr_s. \tag{5.26}$$

5.3.2 Evaluation of integrals

The design formulation of a steerable robust mixed nearfield-farfield broadband beamformer requires the evaluation of four integrals. For the design examples presented in this section, these integrals are approximated by discrete summations with uniformly spaced points. This approach requires sufficient number of discretisation points in order to provide close approximation of the original integrals. However, as the number of points increases, so does the design problem size. Hence, the trade-off here is to have a manageable problem size and yet have an approximation with acceptable accuracy. Another approach is to have non-uniform discretisation points where they are placed in a specific way to increase accuracy with limited number of points, such as the quadrature integration method, which is outside the scope of this thesis.

For simplicity, the design examples in this section utilise approximation with uniform discretisation points, where the range Ψ, Ω, Φ and $\mathcal{R}$ are uniformly discretised into 8, 64, 90 and 2 points respectively. This low number of points is chosen to ensure the design problem size is manageable and solvable using a standard computer.

5.3.3 Discussions on the range $\mathcal{R}$

In this subsection, all design examples are evaluated without introducing any perturbations. The plots of (5.25) and (5.26) for all the designs are shown in Fig. 5.5. From the figure, low performance errors indicate that the designs work within their design specifications. As anticipated, under ideal condition, the robust designs achieve slightly higher performance error as compared to their non-robust counterparts due to the trade-off for robustness.

A more interesting insight can be seen from Fig. 5.5a. Specifically, the design with $\mathcal{R} \in [1, 5]$ remains operable for source located at $r_s > 5$ and has a relatively similar performance error as the other two designs with $\mathcal{R} \in [1, 50]$ and $\mathcal{R} \in [1, 100]$. This indicates that it is not necessary to have the range $\mathcal{R}$ extending far into the farfield region in order for the designs to work for farfield source. The reason for this is that in the nearfield, changes in the source radial distance can cause significant variations to the array response, especially on the phase, due to the curvature of the nearfield source's wavefront. However, as the source enters the farfield region, such effects becomes less significant and eventually becomes negligible, as indicated by the asymptotic performance error in Fig. 5.5a. The plot of (5.24) for the $\mathcal{R} \in [1, 5]$ design, and its beampatterns at $(r_s = 1\text{m}, \psi = 25°)$ and $(r_s = 1000\text{m}, \psi = -20°)$ are shown respectively in Fig. 5.6 and 5.7 as further evidence on the operability of the design as a steerable mixed nearfield-farfield beamformer.

5.3.4 Discussion on robustness

Fig. 5.8 shows the performance errors of the designs with the same perturbations in the microphone characteristics as in Section 4.4.2. As expected, the

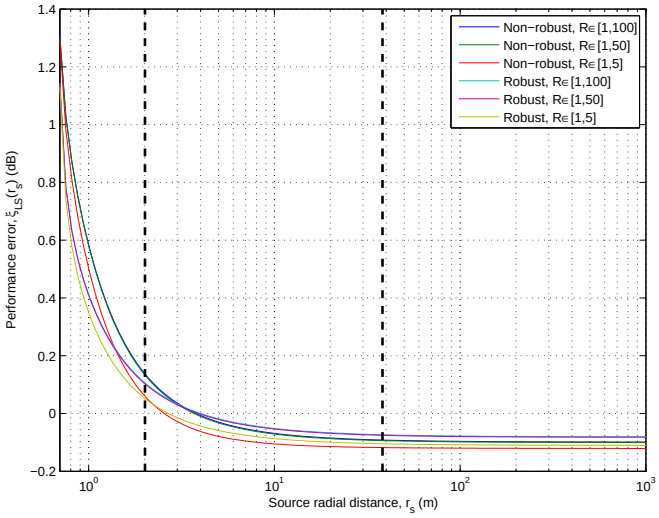

(a) With respect to source radial distance, r_s.

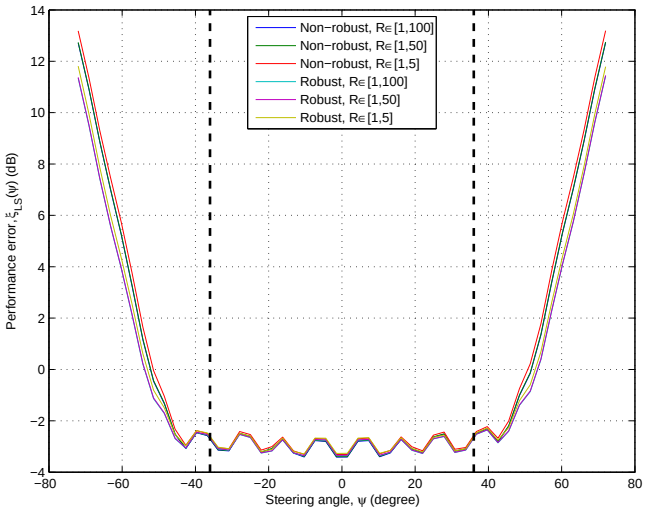

(b) With respect to steering angle, ψ.

Figure 5.5: Comparisons of performance errors of the design examples without any perturbations.

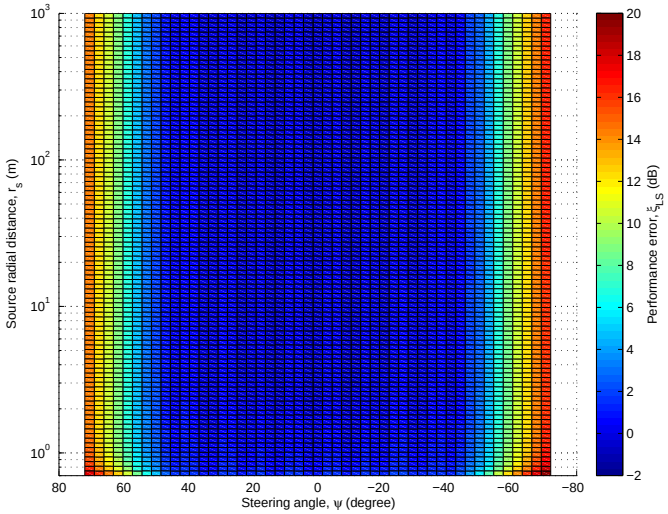

Figure 5.6: Plot of (5.24) for the $\mathcal{R} \in [1, 5]$ design.

robust designs continue to work (indicated by low performance error) in the presence of perturbations, whereas the non-robust designs ceased to work. Several beampatterns for the robust and non-robust $\mathcal{R} \in [1, 5]$ designs, evaluated at $r_s = \{1, 1000\}$m, steered to $\psi = \{0°, 18°, 36°\}$ and with perturbations are shown in Figs. 5.9 - 5.14. Note that from these figures, the introduced perturbations have greater effect on the low frequencies of the non-robust beamformer's response. This is because broadband beamformers behave like superdirective beamformers at low frequencies (see Section 4.1). This is also true for the other non-robust designs with $\mathcal{R} \in [1, 50]$ and $\mathcal{R} \in [1, 100]$.

5.4 Conclusions

In conclusion, a steerable robust mixed nearfield-farfield broadband beamformer design method is proposed. The invariance in the beamformer response against source radial distance is achieved by designing beamformers over a range of source radial distances. The range need not extend far into the farfield region for the beamformers to continue working for farfield sources due to the slow variation in the farfield source's wavefront. The steerability of the main-beam and the robustness of the designs are achieved using the methods discussed in Chapter 3 and 4, respectively.

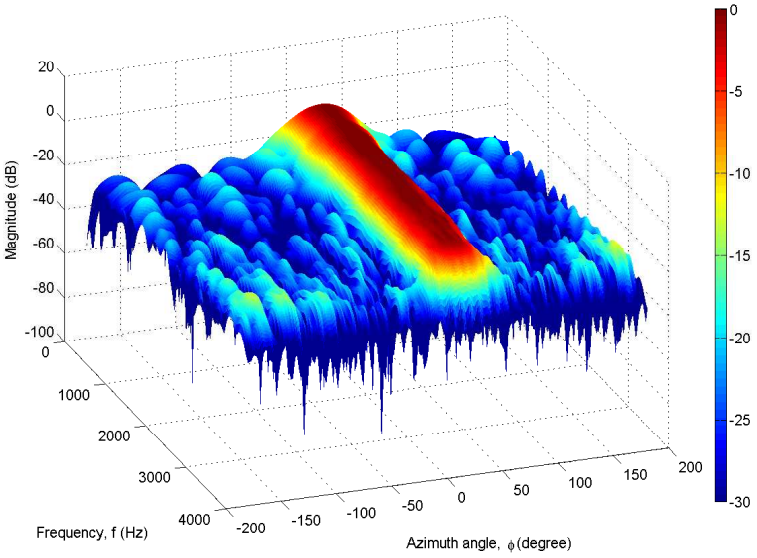

(a) At $r_s = 1\text{m}$ and steered to $\psi = 25°$.

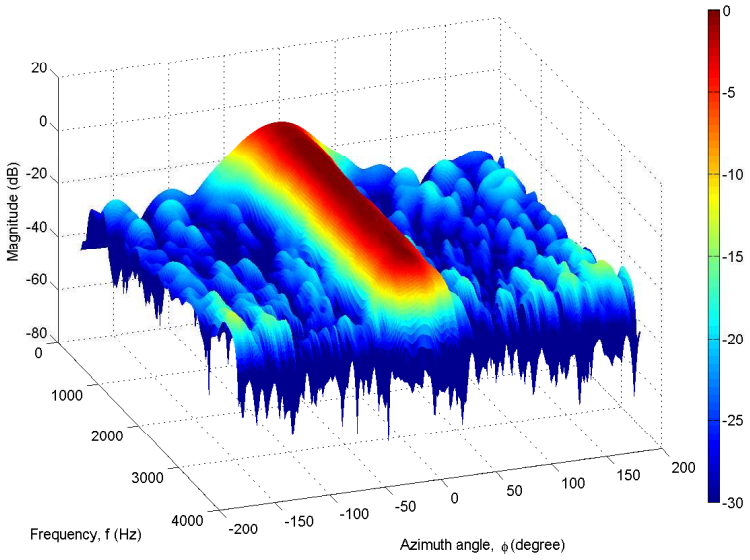

(b) At $r_s = 1000\text{m}$ and steered to $-20°$.

Figure 5.7: Beampatterns for the $\mathcal{R} \in [1, 5]$ design.

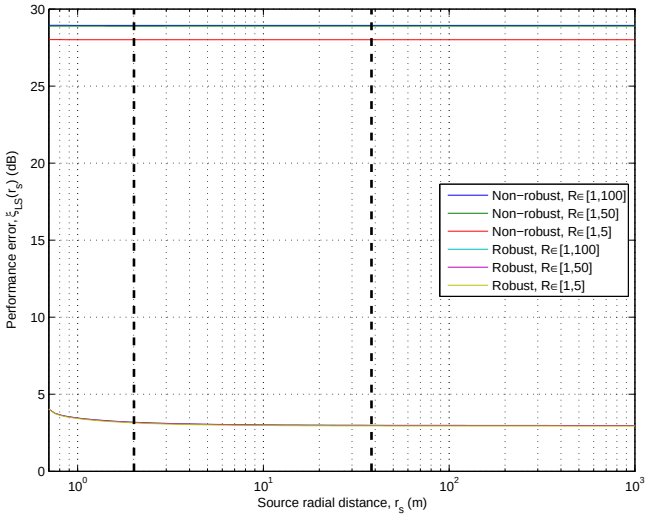

(a) With respect to source radial distance, r_s.

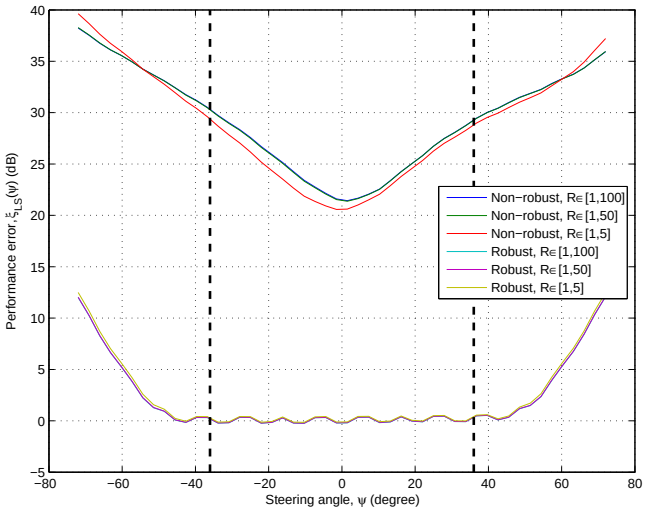

(b) With respect to steering angle, ψ.

Figure 5.8: Comparisons of performance errors of the design examples with perturbation.

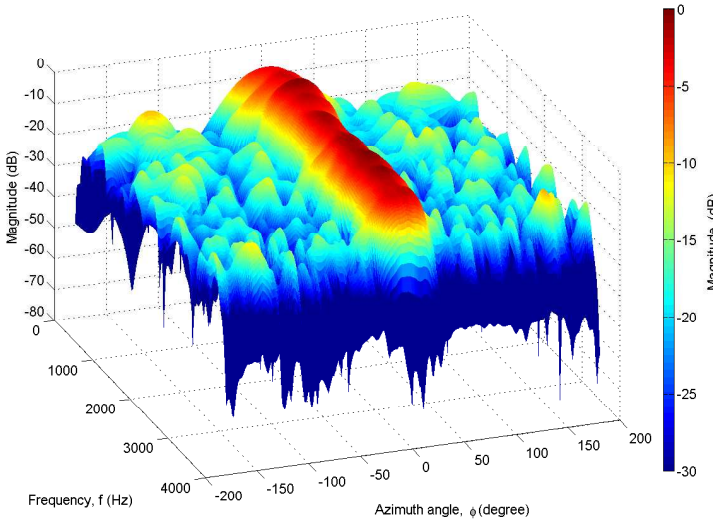

(a) Robust design.

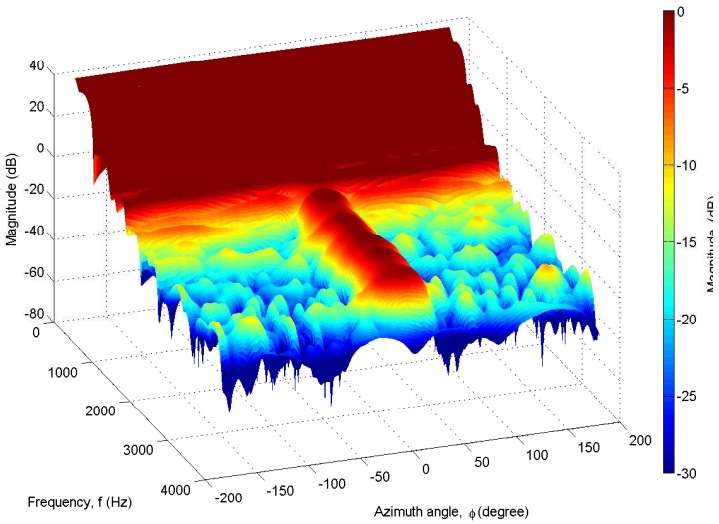

(b) Non-robust design.

Figure 5.9: Beampatterns for the $\mathcal{R} \in [1, 5]$ design at $r_s = 1\text{m}$, steered to $\psi = 0°$ and with perturbation.

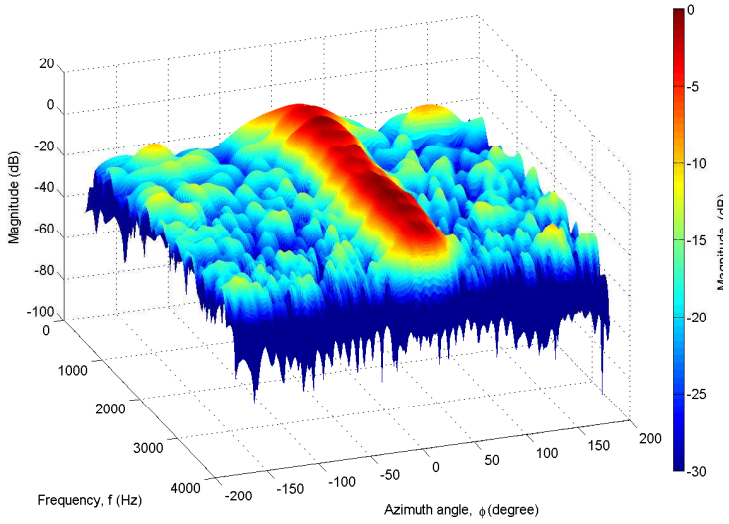

(a) Robust design.

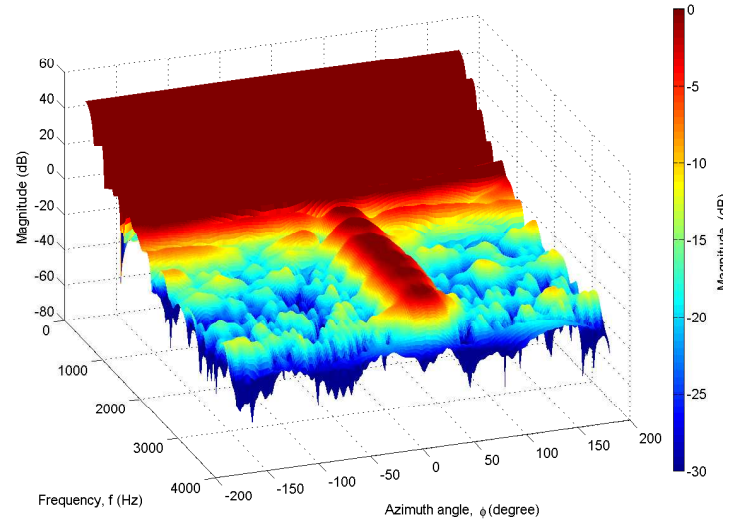

(b) Non-robust design.

Figure 5.10: Beampatterns for the $\mathcal{R} \in [1, 5]$ design at $r_s = 1\text{m}$, steered to $\psi = 18°$ and with perturbation.

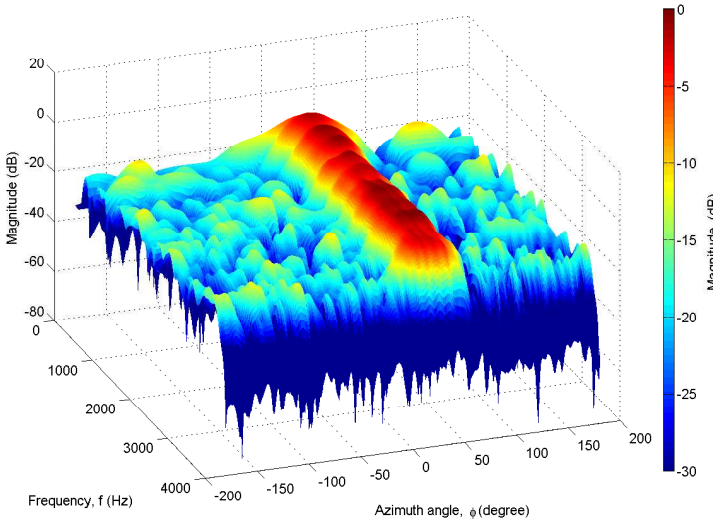

(a) Robust design.

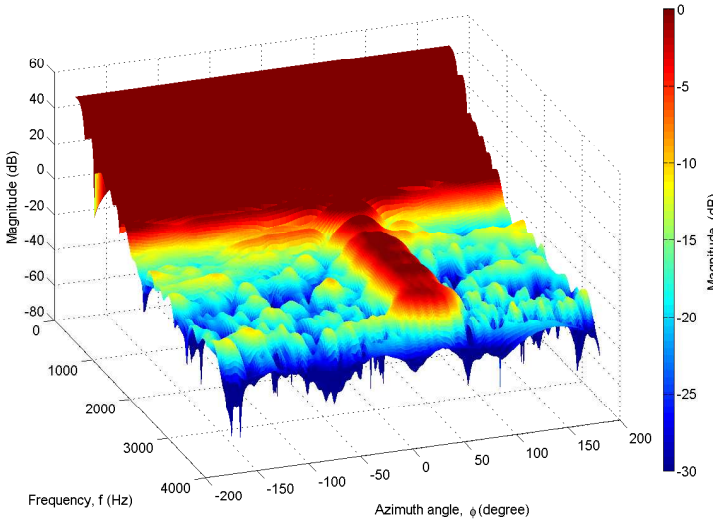

(b) Non-robust design.

Figure 5.11: Beampatterns for the $\mathcal{R} \in [1, 5]$ design at $r_s = 1\text{m}$, steered to $\psi = 36°$ and with perturbation.

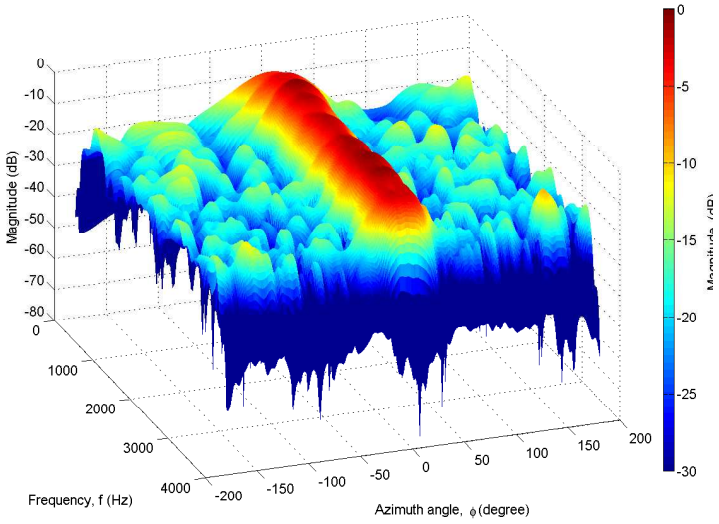

(a) Robust design.

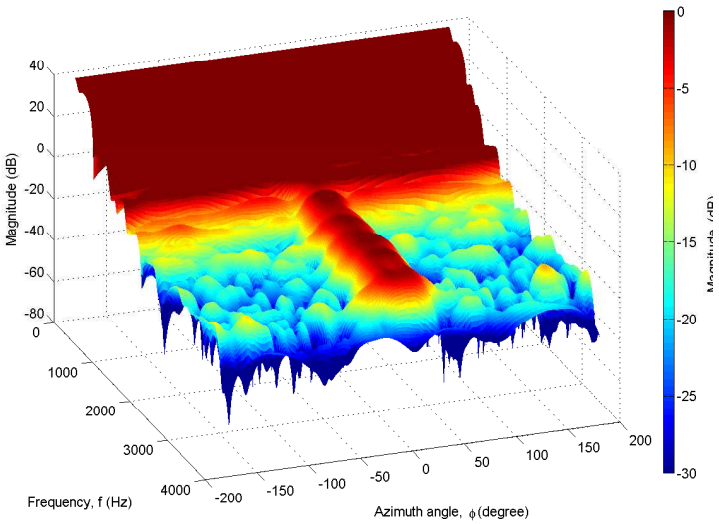

(b) Non-robust design.

Figure 5.12: Beampatterns for the $\mathcal{R} \in [1, 5]$ design at $r_s = 1000$m, steered to $\psi = 0°$ and with perturbation.

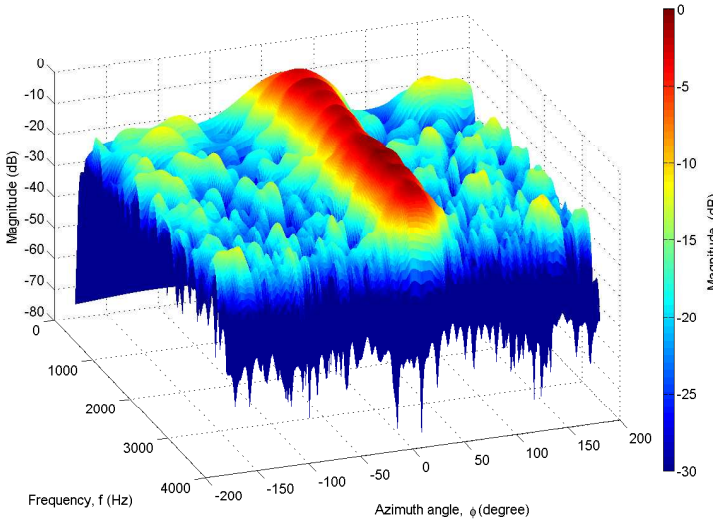

(a) Robust design.

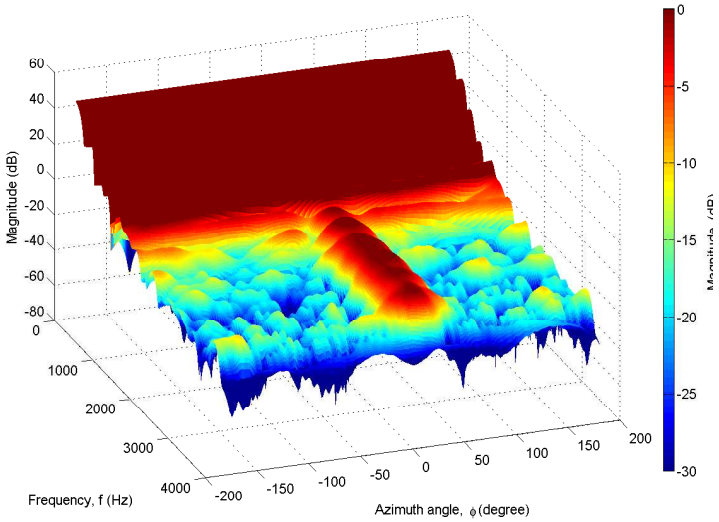

(b) Non-robust design.

Figure 5.13: Beampatterns for the $\mathcal{R} \in [1, 5]$ design at $r_s = 1000$m, steered to $\psi = 18°$ and with perturbation.

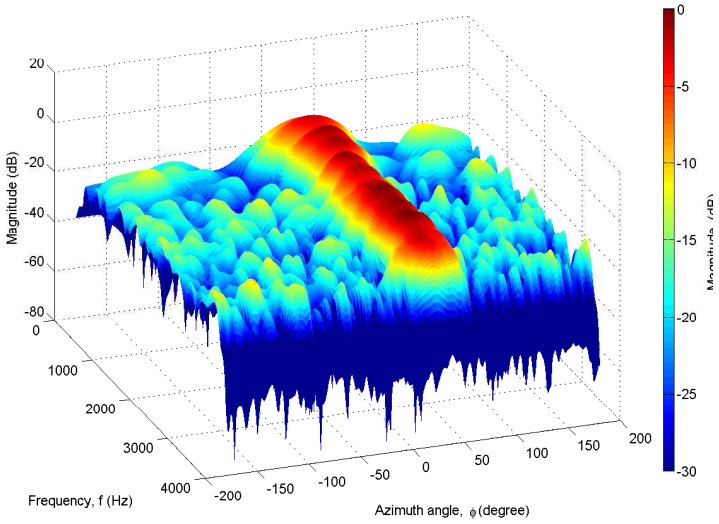

(a) Robust design.

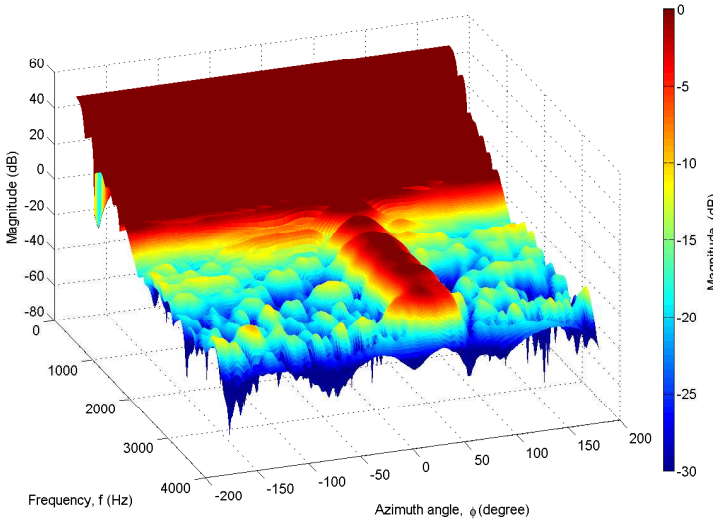

(b) Non-robust design.

Figure 5.14: Beampatterns for the $\mathcal{R} \in [1, 5]$ design at $r_s = 1000$m, steered to $\psi = 36°$ and with perturbation.

Chapter 6

3D Farfield Steerable Broadband Beamformer Design

6.1 Introduction

Thus far, the design formulations of steerable beamformers have been limited to azimuth-only beamformers. This chapter extends the design formulation of steerable beamformers to azimuth-elevation beamformers. Compared to azimuth-only sensor array beamforming, azimuth-elevation sensor array beamforming offers an additional spatial dimension for acoustic reception, which is useful in applications that requires azimuth-elevation spatial sound reception such as audio surveillance, teleconferencing and source localisation [82]. For these applications, spherical arrays can be attractive because their symmetrical structure allows for unbiased response for any azimuth-elevation angle.

A possible method to design steerable azimuth-elevation beamformers for spherical arrays is to employ a 2D Farrow structure, where the two independent Farrow parameters can be used to steer the main-beam around azimuth and elevation planes [83, 84]. However, due to its problem size and complexity, this approach will not be pursued. Instead, a design formulation based on spherical harmonics is presented in this chapter. This approach is particularly appealing since the spherical harmonics framework is closely matched to spherical arrays [42, 43]. The key benefits of the spherical harmonics design approach are:

a) straightforward beam steering with steering invariant beampatterns, b) independence of the sensor sampling scheme, as long as the sensor positions satisfy an orthonormality criterion, and c) usually less computationally intensive than filter-and-sum beamformers.

Initial studies on this subject were carried out by Meyer and Elko [42], and Abhayapala and Ward [43] who propose beamformer designs (commonly known as spherical or modal beamformers) based on the spherical harmonics decomposition of the received sound field. Their designs allow for simple beam steering by means of modulation, similar to the steering mechanism in [85]. Since then, studies in this area have grown which include other modal beamforming approaches such as delay-and-sum method [86], multiple beam and/or null steering [87, 88], Dolph-Chebychev pattern approach [89], nearfield modal beamforming [90, 91] and optimal beamforming approach [92–94].

As the mathematical spherical harmonic framework is established for sound-field reception over a continuous surface as opposed to the use of finite point sensor elements in practice, most of the above spherical beamformer design approaches rely on the numerical integration (known as quadrature scheme) of the received sound field. Under this quadrature scheme, a set of points $\tilde{\Omega}_s$ (or locations of sensor elements) on the surface of the spherical array and their corresponding optimal weights α_s are carefully chosen to satisfy [95]

$$\oint_{\tilde{\Omega}\in S^2} f\left(\tilde{\Omega}\right) d\tilde{\Omega} = \sum_{s=1}^{S} \alpha_s f\left(\tilde{\Omega}_s\right) \tag{6.1}$$

where $f(\cdot)$ is a polynomial of order $(2S-1)$, $\tilde{\Omega} = \left(\tilde{\theta}, \tilde{\phi}\right)$ represents points (in spherical coordinate system) on the surface S^2 of a unit sphere and the integral $\oint_{\tilde{\Omega}\in S^2} d\tilde{\Omega} = \int_0^{2\pi}\int_0^{\pi} \sin(\tilde{\theta}) d\tilde{\theta} d\tilde{\phi}$ covers the whole surface S^2. In practice, it may not always be feasible if not impossible to find a set of points $\tilde{\Omega}_s$ satisfying (6.1), and this will lead to spatial aliasing from high order spherical harmonics [96].

In this chapter, a filter-and-sum beamformer design formulation integrated with the steering capability of spherical harmonic beamforming is proposed to attain azimuth-elevation beamformers with simple steering mechanism. This is achieved by including the modal decomposition and beam steering block from

[42, 93, 97] into the classical filter-and-sum beamformer structure. The resulting structure is similar to the existing spherical harmonic beamformer structure, except that the filtering block has been moved to the sensor end. Although this modification causes the independent sensor sampling and computational advantages from the existing spherical harmonic beamformers to be lost, it allows for arbitrary sensor positions, i.e. the choice of sensor configuration need not satisfy (6.1), and yet retains the steering invariant property of spherical harmonic beamforming. In addition, it can be shown that the proposed method requires fewer sensors to achieve similar performance as the existing spherical harmonic beamformers for the same order of spherical harmonics. Other properties and the performances of the proposed method are also discussed and compared to existing design approaches in this chapter.

This chapter is organised as follows. Section 6.2 provides a brief background on the existing spherical beamformer design approach, followed by Section 6.3 for different sensor sampling schemes on the surface of a spherical array. Section 6.4 provides the design formulation of the proposed method in both frequency and time domain, followed by an investigation of its properties in Section 6.5. Performance evaluations and comparison with existing design approach is presented in Section 6.6 and finally conclusions are drawn in Section 6.7.

6.2 Background

Consider a unit magnitude plane wave (farfield source model) impinging on a sphere with radius a from direction $\Omega = (\theta, \phi)$ as shown in Fig. 6.1, where θ is the elevation angle and ϕ is the azimuth angle. The frequency domain expression of the total sound pressure as observed at a point $\tilde{\Omega} = \left(\tilde{\theta}, \tilde{\phi}\right)$ on the sphere surface can be written as

$$p\left(ka, \Omega, \tilde{\Omega}\right) = \sum_{n=0}^{\infty} \sum_{m=-n}^{n} p_n^m\left(ka, \Omega\right) Y_n^m\left(\tilde{\Omega}\right) \tag{6.2}$$

where $k = {}^{2\pi f}/_{c}$ is the wavenumber, f is the frequency and c is the speed of propagating wave. $Y_n^m(\Omega)$ is the spherical harmonics of order n and degree m,

and is given by [33]

$$Y_n^m(\Omega) = Y_n^m(\theta,\phi) = \sqrt{\frac{(2n+1)}{4\pi}\frac{(n-m)!}{(n+m)!}} P_n^m(\cos(\theta))\, e^{im\phi} \tag{6.3}$$

where $P_n^m(\cos(\theta))$ is the associated Legendre polynomial of order n and degree m, and $i = \sqrt{-1}$. The term $p_n^m(ka,\Omega)$, which is the spherical Fourier transform or spherical harmonic coefficient of $p\left(ka,\Omega,\tilde{\Omega}\right)$, is given by

$$p_n^m(ka,\Omega) = \oint_{\tilde{\Omega}\in S^2} p\left(ka,\Omega,\tilde{\Omega}\right)\left[Y_n^m\left(\tilde{\Omega}\right)\right]^* d\tilde{\Omega} \tag{6.4}$$

where the integration is evaluated over the whole surface of the unit sphere S^2, and the superscript $*$ denotes complex conjugate. Note that (6.4) is the spherical harmonic transform of $p\left(ka,\Omega,\tilde{\Omega}\right)$ and (6.2) is its inverse [33]. Explicit expression for $p_n^m(ka,\Omega)$, which can be obtained by solving the wave equation, is given by

$$p_n^m(ka,\Omega) = b_n(ka)\left[Y_n^{m*}(\Omega)\right]^* \tag{6.5}$$

where the coefficient $b_n(ka)$ depends on the type of sphere. For example, for an open sphere (sensors are "floating" in free space) and rigid sphere (sensors mounted on surface of solid sphere) [33],

$$b_n(ka) = \begin{cases} 4\pi i^n j_n(ka), & \text{open sphere} \\ 4\pi i^n\left(j_n(ka) - \frac{j_n'(ka)}{h_n'(ka)} h_n(ka)\right), & \text{rigid sphere} \end{cases} \tag{6.6}$$

where $j_n(\cdot)$ and $h_n(\cdot)$ are respectively the n^{th} order spherical Bessel and Hankel function of the first kind, and $j_n'(\cdot)$ and $h_n'(\cdot)$ are their derivatives with respect to their arguments.

The basic principle in spherical beamformer designs is to use the spherical harmonic framework to decompose the sound field received by a spherical array into orthogonal components. These components are then linearly combined to achieve a desired beampattern [33, 94]. Hence, the beampattern for a spherical beamformer can be written as

$$B(f,\Omega) = \oint_{\tilde{\Omega}\in S^2} p\left(ka,\Omega,\tilde{\Omega}\right) w^*\left(f,\tilde{\Omega}\right) d\tilde{\Omega}, \tag{6.7}$$

where $w\left(f,\tilde{\Omega}\right)$ is the complex beamformer weight. In practice, the continuous term $\tilde{\Omega}$ in (6.7) is sampled at finite sensor positions $\tilde{\Omega}_s$ for $s = 1,...,S$. Equation

(6.7) then becomes

$$B(f,\Omega) = \sum_{s=1}^{S} \alpha_s p\left(ka, \Omega, \tilde{\Omega}_s\right) w^*\left(f, \tilde{\Omega}_s\right) \tag{6.8}$$

$$= \sum_{n=0}^{N} \sum_{m=-n}^{n} p_n^m(ka,\Omega)\left[w_n^m(f)\right]^* \tag{6.9}$$

$$= \sum_{n=0}^{N} w_n(f)\, b_n(ka) \sum_{m=-n}^{n} \left[Y_n^m(\Omega)\right]^* Y_n^m(\Omega_0) \tag{6.10}$$

where the real scalar α_s is due to spatial sampling (see Section 6.3) and $[w_n^m(f)]^*$, which is the spherical harmonic transform of $w^*\left(f, \tilde{\Omega}_s\right)$, is normally selected to be

$$\left[w_n^m(f)\right]^* = w_n(f)\, Y_n^m(\Omega_0) \tag{6.11}$$

in order to achieve steerability to any look direction Ω_0 and rotational symmetric beampattern around Ω_0 [42, 97]. The aim for designing a modal beamformer is to find the complex weights $w_n(f)$. For frequency invariant (broadband) designs, it is necessary to find $w_n(f)$ such that

$$w_n(f)\, b_n(ka) = a_n, f \in \Omega_{pb} \tag{6.12}$$

where a_n is some scalar that is independent of frequency within the spectral range Ω_{pb}. Hence,

$$w_n(f) = \frac{a_n}{b_n(ka)}. \tag{6.13}$$

However, at low frequencies, only the zeroth mode ($n = 0$) is significant, while the other modes are very small (see Fig. 6.2). This will result in very large $w_n(f)$ for $n > 0$ at low frequencies, which makes the beamformer very sensitive to errors and perturbations.

The structure of the modal beamformer is shown in Fig. 6.3. In the first stage, the received signals are decomposed by the modal decomposition block into their spherical harmonic components. The spherical harmonic components are then modulated by the steering block to favour reception from the desired look direction. Finally, frequency response and beampattern shaping are performed by the filtering block.

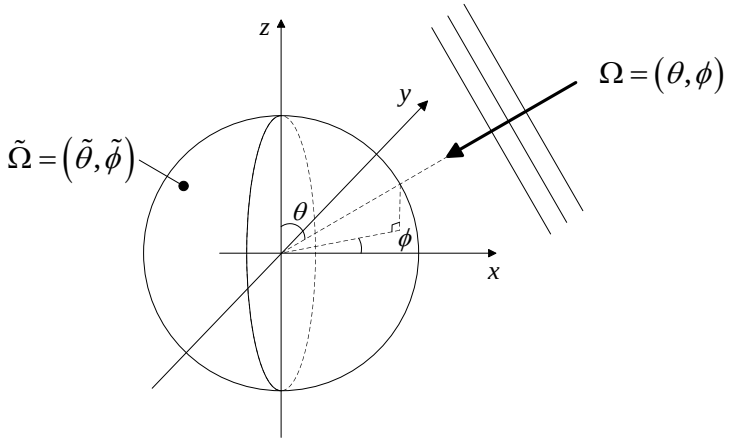

Figure 6.1: Plane wave incident on spherical array.

6.3 Sensor element sampling theorem

The spherical beamformer design formulation in the previous section has been formulated by implicitly assuming that the sensor positions have been chosen to follow the orthonormality criterion

$$\sum_{s=1}^{S} \alpha_s Y_{n'}^{m'} \left(\tilde{\Omega}_s\right) \left[Y_n^m \left(\tilde{\Omega}_s\right)\right]^* = \delta(n-n')\,\delta(m-m') \quad n, n' \leq N \tag{6.14}$$

where $\delta(\cdot)$ is the delta function, N is the highest spherical harmonics order, and $\alpha_s \in \mathbb{R}$ is the scaling factor of the s^{th} sensor which depends on the sampling scheme. The requirement of (6.14) can be seen as follows. Taking the individual spherical harmonic transform of $p\left(ka, \Omega, \tilde{\Omega}_s\right)$ and $w^*\left(f, \tilde{\Omega}_s\right)$ in (6.8) gives

$$B(f,\Omega) = \sum_{s=1}^{S} \alpha_s \sum_{n=0}^{N} \sum_{m=-n}^{n} p_n^m(ka,\Omega) \left[Y_n^m \left(\tilde{\Omega}_s\right)\right]^* \sum_{n'=0}^{N} \sum_{m'=-n'}^{n'} \left[w_{n'}^{m'}(f)\right]^* Y_{n'}^{m'} \left(\tilde{\Omega}_s\right) \tag{6.15}$$

$$= \sum_{n=0}^{N} \sum_{m=-n}^{n} p_n^m(ka,\Omega) \sum_{n'=0}^{N} \sum_{m'=-n'}^{n'} \left[w_{n'}^{m'}(f)\right]^* \sum_{s=1}^{S} \alpha_s \left[Y_n^m \left(\tilde{\Omega}_s\right)\right]^* Y_{n'}^{m'} \left(\tilde{\Omega}_s\right) \tag{6.16}$$

$$= \sum_{n=0}^{N} \sum_{m=-n}^{n} p_n^m(ka,\Omega) \left[w_n^m(f)\right]^* \tag{6.17}$$

where the last step results from using (6.14) and is as obtained in (6.9).

The condition (6.14) can also be considered as a criterion to avoid spatial aliasing when sampling a bandlimited harmonic order (up to N) function on a

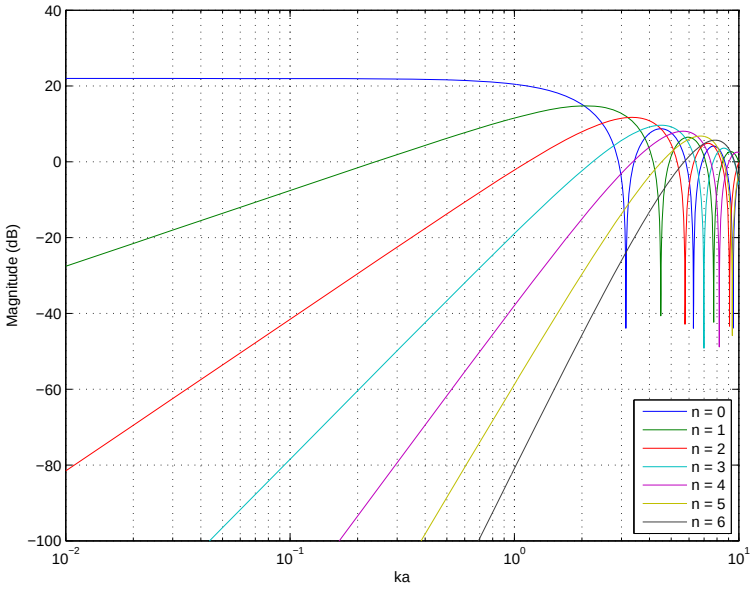

(a) Open sphere.

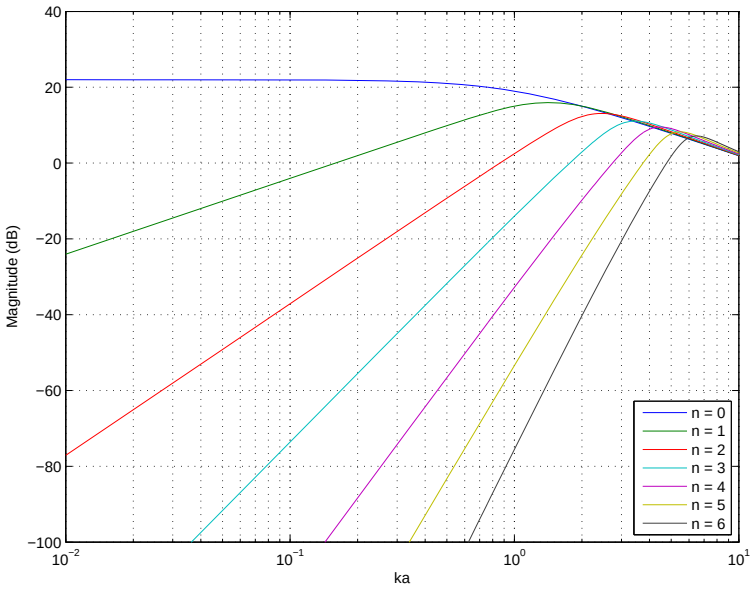

(b) Rigid sphere.

Figure 6.2: Magnitude of $b_n(ka)$ for open and rigid sphere.

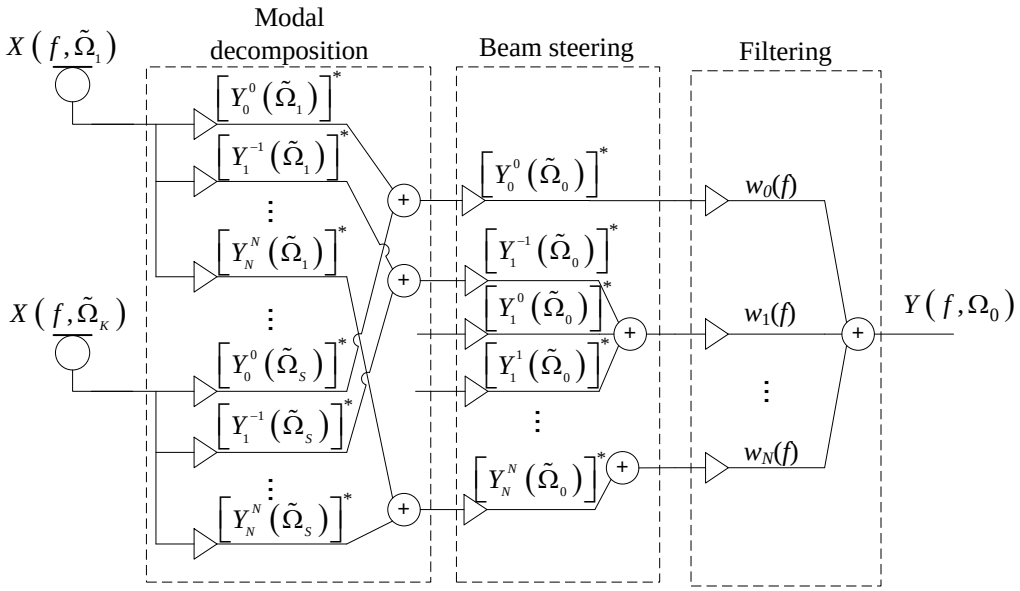

Figure 6.3: Existing modal beamformer structure.

sphere [96, 98]. A sampling scheme is considered alias-free if condition (6.14) is satisfied completely without any error.

Hence, there exist a number of sampling schemes that aim to choose a set of points on a sphere and their corresponding weights α_s such that (6.14) is satisfied without error (or at least with negligible error). These sampling schemes exhibit trade-off between the number of required points and how close (6.14) can be satisfied.

6.3.1 Equiangle sampling

The equiangle sampling scheme is presented by Driscoll and Healy [99]. In this scheme, a total of $4(N+1)^2$ points are required to sampled a bandlimited function ($f_n^m = 0$ for $n > N$) on a sphere without aliasing. The points are selected such that the elevation angle $\tilde{\theta}$ and the azimuthal angle $\tilde{\phi}$ are uniformly spaced, i.e. $\tilde{\theta} = {}^{\pi j}/_{(2N+2)}$, $j = 0, ..., 2N+1$, and $\tilde{\phi} = {}^{\pi k}/_{(2N+2)}$, $k = 0, ..., 2N+1$. The spherical harmonic transform using this sampling scheme is given by

$$f_n^m = \sum_{j=0}^{2N+1} \sum_{k=0}^{2N+1} \alpha_j f\left(\tilde{\theta}_j, \tilde{\phi}_k\right) \left[Y_n^m\left(\tilde{\theta}_j, \tilde{\phi}_k\right)\right]^*. \tag{6.18}$$

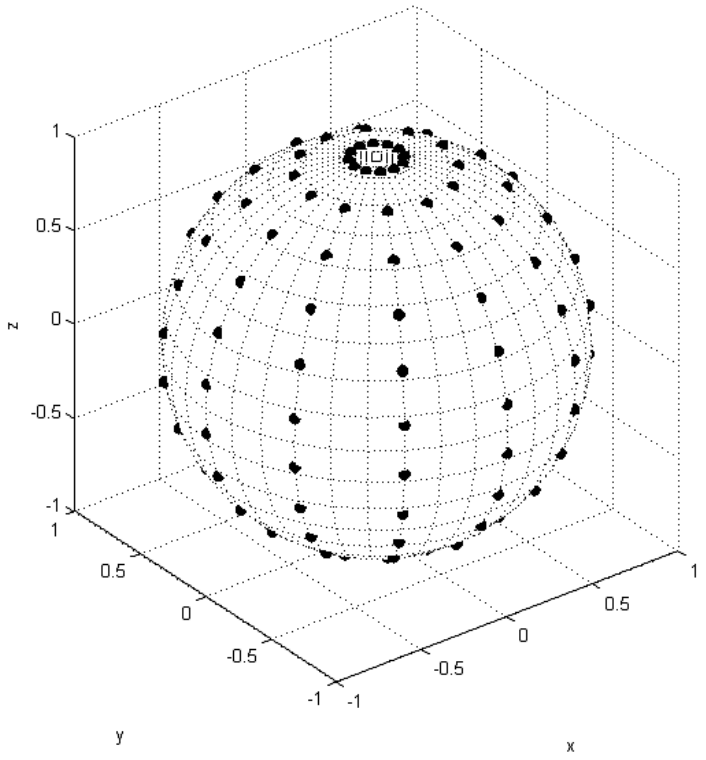

Figure 6.4: Sampled 144 points for a function bandlimited to $N = 5$ using the equiangle sampling scheme.

The weights α_j are used to compensate for the denser grid near the poles and are chosen such that

$$\sum_{j=0}^{2N+1} \alpha_j P_n \left(\cos \left(\tilde{\theta}_j \right) \right) = \sqrt{2} \delta \left(n \right). \tag{6.19}$$

The main advantage of this scheme is the constant angular difference in both $\tilde{\theta}$ and $\tilde{\phi}$, which is useful in applications where such symmetry is required. However, the large number of required samples makes it less attractive compared to alternative schemes. In order to illustrate this sampling scheme, a set of 144 samples required for a function bandlimited to $N = 5$ is shown in Fig. 6.4 and its corresponding orthonormality (6.14) is shown in Fig. 6.5.

6.3.2 Gaussian sampling

The second sampling scheme is the Gaussian quadrature sampling scheme [100, 101], which requires only $2\left(N+1\right)^2$ points. In this scheme, the azimuthal angle $\tilde{\phi}$

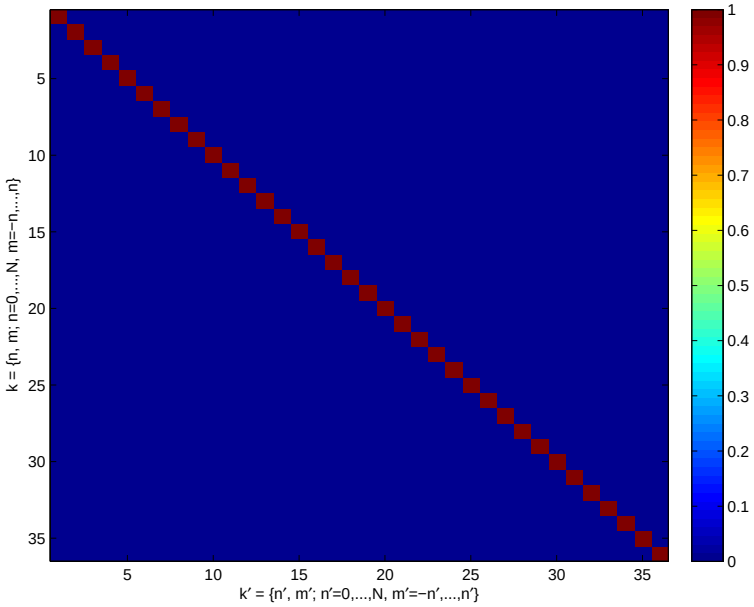

Figure 6.5: Orthonormality plot of the points in Fig. 6.4 up to order $N = 5$.

is sampled similarly to the equiangle scheme, but the elevation angle $\tilde{\theta}$ is sampled only at $N + 1$ points, which are nearly equally spaced. The samples $\tilde{\theta}_j$ is chosen as the zeros of the $N + 1$ order Legendre polynomial, i.e. $P_{N+1}\left(\cos\left(\tilde{\theta}_j\right)\right) = 0$ for $j = 0, ..., N$. This choice forces $f_n^m = 0$ for $n = N + 1$, thus satisfying (6.14). The spherical harmonic transform for this scheme is

$$f_n^m = \sum_{j=0}^{N} \sum_{k=0}^{2N+1} \alpha_j f\left(\tilde{\theta}_j, \tilde{\phi}_k\right) \left[Y_n^m\left(\tilde{\theta}_j, \tilde{\phi}_k\right)\right]^*. \tag{6.20}$$

The weights α_j are chosen similarly to (6.19) except that the upper summation limit is now N rather than $2N + 1$. The advantage of this scheme is that it requires less points compared to the equiangle scheme. However, its non-uniform spacing in $\tilde{\theta}$ may not be desirable in some applications. The required 72 points to sample a bandlimited function ($N = 5$) using this scheme is shown in Fig. 6.6, with its orthonormality shown in Fig. 6.7.

6.3.3 Uniform or quasi uniform sampling

The third sampling scheme is the uniform or quasi-uniform sampling scheme [102, 103], where the distances (as measured along the sphere arc) between adjacent sensors are uniform. This sampling scheme limits the sensor configurations

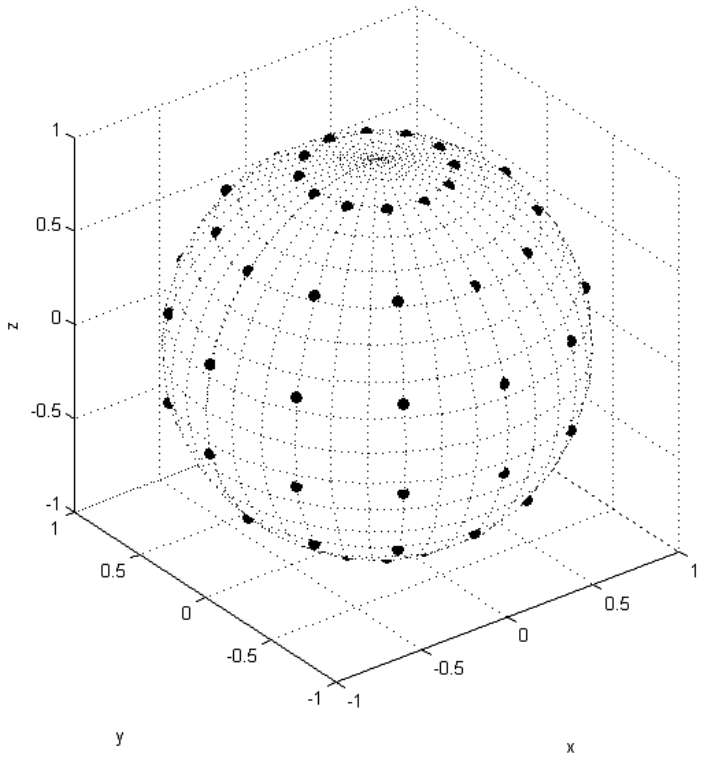

Figure 6.6: Sampled 72 points for a function bandlimited to $N = 5$ using the Gaussian sampling scheme.

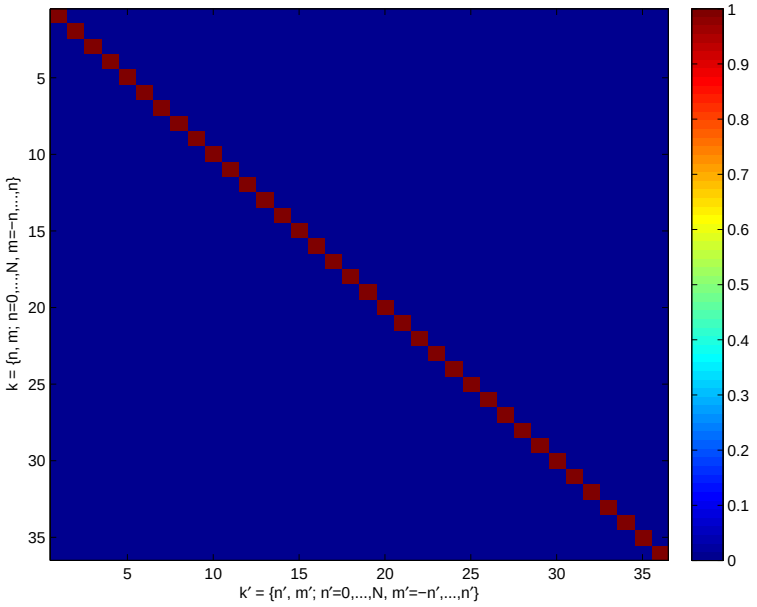

Figure 6.7: Orthonormality plot of the points in Fig. 6.6 up to order $N = 5$.

to specific geometries known as platonic solids, which can only accommodate a certain number of sensors [104]. For cases where there is no known platonic solid for a given number of sensors, only quasi-uniform sampling is achieved. For these cases, the criterion (6.14) is no longer satisfied completely and is normally compensated by increasing the number of sensors. In fact, Hardin and Sloane [105] show that the number of sensors required for this sampling scheme is at least $(N+1)^2$, but in practice, more than $1.5\,(N+1)^2$ are required.

The advantages of this quasi-uniform sampling scheme are its small number of required sensors, and the wider range of possible configurations compared to the equiangle and Gaussian schemes. However, its non-uniform angular difference in both $\tilde{\theta}$ and $\tilde{\phi}$ may cause inconvenience in some applications.

The set of points and weights for this sampling scheme can be found using the methods in [102, 103, 105], which include the truncation of platonic solids and the minimisation of potential energy on a unit sphere surface (also known as Thompson's problem). As an example, Fig. 6.8 shows the required 54 points (obtained from the minimisation of Thompson's problem) to sample a bandlimited function ($N = 5$) using this scheme and its orthonormality is shown in Fig. 6.9. It should be noted that Fig. 6.9 shows that the criterion (6.14) is only satisfied up to negligible error under this uniform scheme as there is no platonic solid for 54 points.

6.4 Proposed spherical beamformer design formulation

Although the uniform sampling scheme offers a wide range of configurations, they are still limited and are usually predefined. Hence, individual points cannot be flexibly relocated or removed to suit specific applications (such as to make room for cable outlet) where such regularity is infeasible or irregular sensor positions is required. In order to allow such flexibility, Li and Duraiswami [94] proposed a spherical beamformer design approach that allows flexibility in the sensor positions by designing the beamformer weights to explicitly satisfy the

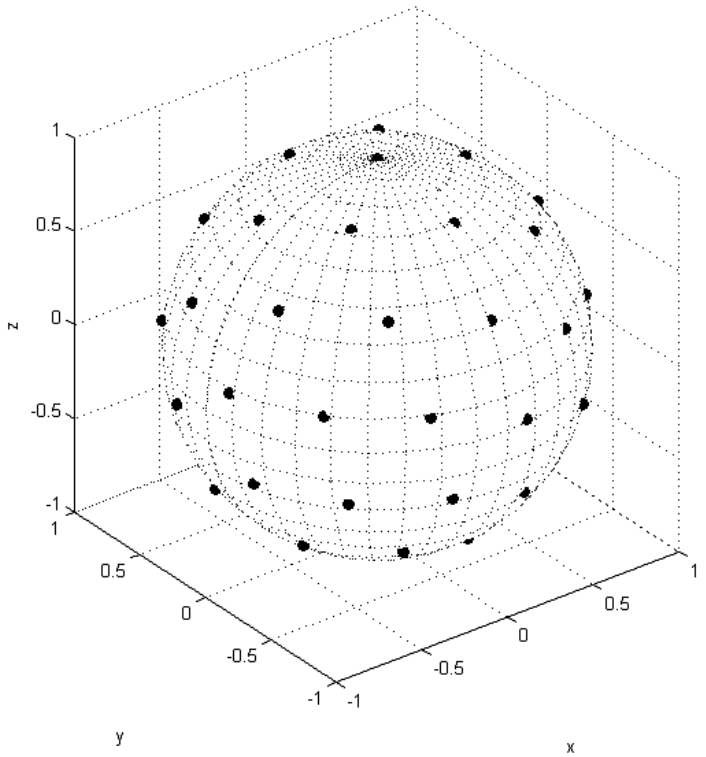

Figure 6.8: Sampled 54 points for a function bandlimited to $N = 5$ using the uniform sampling scheme.

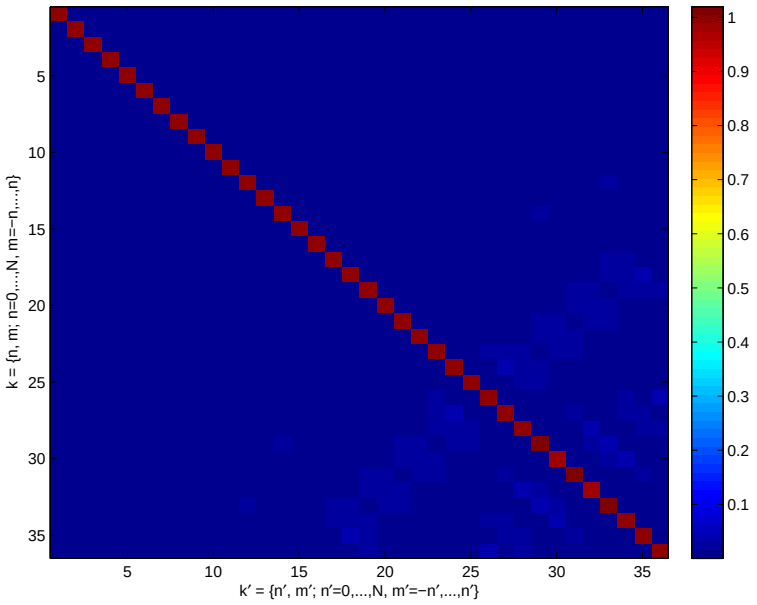

Figure 6.9: Orthonormality plot of the points in Fig. 6.8 up to order $N = 5$.

orthonormality property. However, their method no longer steers the main-beam similarly to [42, 97], i.e. by means of modulation with $Y_n^m(\Omega_0)$. Instead, they require different sets of beamformer weights for each discrete steering direction, which can limit the number of steering directions due to the finite memory size to store the beamformer weights.

The proposed method presented in this section not only allows for flexibility in sensor positions (as in [94]) but also reduces the required number of sensors to $(N+1)^2$ and yet maintains the ease of beam steering as in [42, 97]. The design formulations in both frequency and time domains are described below.

6.4.1 Frequency domain design

Consider a sphere with radius a where its surface is made of a continuous sound pressure receiver (continuous sensor array) and a point on its surface is denoted as $\tilde{\Omega} = \left(\tilde{\theta}, \tilde{\phi}\right)$. Suppose the output of the continuous array is weighted with a frequency and location (on the surface of the sphere) dependent complex weight $w\left(f, \tilde{\Omega}\right)$. Then the beampattern, which is defined as the beamformer response to a unit magnitude incoming wave from any direction Ω, is given by

$$A(f,\Omega) = \oint_{\tilde{\Omega}\in S^2} p\left(ka, \Omega, \tilde{\Omega}\right) w^*\left(f, \tilde{\Omega}\right) d\tilde{\Omega}. \tag{6.21}$$

Substituting (6.2) and (6.5) into (6.21), and restricting the summation to the N^{th} order spherical harmonics, results in

$$A(f,\Omega) \approx \sum_{n=0}^{N} \sum_{m=-n}^{n} b_n(ka) \left[Y_n^m(\Omega)\right]^* \oint_{\tilde{\Omega}\in S^2} w^*\left(f, \tilde{\Omega}\right) Y_n^m\left(\tilde{\Omega}\right) d\tilde{\Omega}. \tag{6.22}$$

In order to incorporate the ability to rotate the beampattern to any direction $\Omega_0 = (\theta_0, \phi_0)$, the term $Y_n^m(\Omega_0)$ is included at the right hand side of (6.22) [42, 97], which yields

$$B(f,\Omega,\Omega_0) = \sum_{n=0}^{N} \sum_{m=-n}^{n} \left(b_n(ka) \oint_{\tilde{\Omega}\in S^2} w^*\left(f, \tilde{\Omega}\right) Y_n^m\left(\tilde{\Omega}\right) d\tilde{\Omega} \right) \times \left[Y_n^m(\Omega)\right]^* Y_n^m(\Omega_0). \tag{6.23}$$

Suppose the desired beampattern with the main-beam pointing at Ω_0 be given by

$$B_d\left(f,\Omega,\Omega_0\right)=\sum_{n=0}^{N}\sum_{m=-n}^{n}\alpha_n^m\left(f\right)\left[Y_n^m\left(\Omega\right)\right]^*Y_n^m\left(\Omega_0\right), \tag{6.24}$$

which is a linear combination of the complex conjugate of all spherical harmonics up to order N with frequency dependent complex gains $\alpha_n^m\left(f\right)$. Equating the expression for the actual beampattern in (6.23) with the desired beampattern in (6.24) yields

$$b_n\left(ka\right)\oint_{\tilde{\Omega}\in S^2}w^*\left(f,\tilde{\Omega}\right)Y_n^m\left(\tilde{\Omega}\right)d\tilde{\Omega}=\alpha_n^m\left(f\right)\quad\forall n,m. \tag{6.25}$$

Since

$$\left[S\left\{w\left(f,\tilde{\Omega}\right)\right\}\right]^*=\oint_{\tilde{\Omega}\in S^2}w^*\left(f,\tilde{\Omega}\right)Y_n^m\left(\tilde{\Omega}\right)d\tilde{\Omega}, \tag{6.26}$$

where $S\left\{\cdot\right\}$ is the spherical harmonic transform, the solution for $w\left(f,\tilde{\Omega}\right)$ is given by

$$\begin{aligned}w\left(f,\tilde{\Omega}\right)&=S^{-1}\left\{\left[\frac{\alpha_n^m\left(f\right)}{b_n\left(ka\right)}\right]^*\right\}\\&=\sum_{n=0}^{\infty}\sum_{m=-n}^{n}\left[\frac{\alpha_n^m\left(f\right)}{b_n\left(ka\right)}\right]^*Y_n^m\left(\tilde{\Omega}\right).\end{aligned} \tag{6.27}$$

Although (6.27) gives the analytical expression for the continuous spherical beamformer weights of the proposed design, it is not practical due to its infinite sum.

In order to make the design practical, the continuous sensor array on the sphere surface is discretised into K discrete points or sensors, indexed by $s=1,...,K$. Hence, (6.23) becomes

$$B\left(f,\Omega,\Omega_0\right)\approx\sum_{n=0}^{N}\sum_{m=-n}^{n}\left(b_n\left(ka\right)\sum_{s=1}^{K}w^*\left(f,\tilde{\Omega}_s\right)Y_n^m\left(\tilde{\Omega}_s\right)\right)\left[Y_n^m\left(\Omega\right)\right]^*Y_n^m\left(\Omega_0\right) \tag{6.28}$$

where the factor α_s for the s^{th} sensor has been merged into $w^*\left(f,\tilde{\Omega}_s\right)$. The equation to find the beamformer weights (by equating (6.28) with (6.24)) is then given by

$$b_n\left(ka\right)\sum_{s=1}^{K}w^*\left(f,\tilde{\Omega}_s\right)Y_n^m\left(\tilde{\Omega}_s\right)=\alpha_n^m\left(f\right) \tag{6.29}$$

for all $n \in \{0, 1, ..., N\}$, $m \in \{-n, -n+1, ..., n\}$ and $f \in \Omega_{pb}$. Let

$$\mathbf{Y} = \left[\left(\mathbf{y}_0^0\right), \left(\mathbf{y}_1^{-1}\right), \left(\mathbf{y}_1^0\right), \left(\mathbf{y}_1^1\right), ..., \left(\mathbf{y}_N^N\right)\right]^{\mathrm{T}}, \tag{6.30}$$

$$\mathbf{y}_n^m = \left[Y_n^m\left(\tilde{\Omega}_1\right), ..., Y_n^m\left(\tilde{\Omega}_K\right)\right]^{\mathrm{T}}, \tag{6.31}$$

$$\mathbf{w}\left(f\right) = \left[w^*\left(f, \tilde{\Omega}_1\right), ..., w^*\left(f, \tilde{\Omega}_K\right)\right]^{\mathrm{T}}, \tag{6.32}$$

$$\boldsymbol{\alpha}\left(f\right) = \left[\alpha_0^0\left(f\right), \alpha_1^{-1}\left(f\right), \alpha_1^0\left(f\right), \alpha_1^1\left(f\right), ..., \alpha_N^N\left(f\right)\right]^{\mathrm{T}}, \tag{6.33}$$

$$\mathbf{B}\left(ka\right) = \mathrm{diag}\left\{b_0\left(ka\right) \otimes \mathbf{1}_1, ..., b_N\left(ka\right) \otimes \mathbf{1}_{(2N+1)}\right\}, \tag{6.34}$$

where $\mathrm{diag}\{\cdot\}$ is a square diagonal matrix with the given diagonal elements, $\mathbf{1}_J$ is a length J row vector with all unity elements, and $\otimes$ denotes the Kronecker product. Using (6.30) - (6.34), equation (6.29) can be rewritten in matrix form as follows

$$\mathbf{B}\left(ka\right)\mathbf{Y}\mathbf{w}\left(f\right) = \boldsymbol{\alpha}\left(f\right) \tag{6.35}$$

which has analytical solution (in the least square sense)

$$\mathbf{w}\left(f\right) = \left(\mathbf{Y}^{\mathrm{H}}\mathbf{B}^{\mathrm{H}}\left(ka\right)\mathbf{B}\left(ka\right)\mathbf{Y}\right)^{-1}\mathbf{Y}^{\mathrm{H}}\mathbf{B}^{\mathrm{H}}\left(ka\right)\boldsymbol{\alpha}\left(f\right). \tag{6.36}$$

If $\mathbf{B}\left(ka\right)\mathbf{Y}$ is invertible, then (6.36) reduces to

$$\mathbf{w}\left(f\right) = \mathbf{Y}^{-1}\mathbf{B}^{-1}\left(ka\right)\boldsymbol{\alpha}\left(f\right). \tag{6.37}$$

The Fourier transform of the output signal for the proposed beamformer is given by

$$Y\left(f, \Omega_0\right) = \sum_{n=0}^{N}\sum_{m=-n}^{n} z_n^m\left(f\right)Y_n^m\left(\Omega_0\right) \tag{6.38}$$

where the term $Y_n^m\left(\Omega_0\right)$ steers the main-beam to direction Ω_0, and the modal decomposition of the intermediate output $z_n^m\left(f\right)$ is given by

$$z_n^m\left(f\right) = \sum_{s=1}^{K}\left[X(f, \tilde{\Omega}_s)w^*\left(f, \tilde{\Omega}_s\right)\right]\left[Y_n^m\left(\tilde{\Omega}_s\right)\right]^* \tag{6.39}$$

with $X(f, \tilde{\Omega}_s)$ the Fourier transform of the received signal at the s^{th} sensor. The structure of the proposed spherical beamformer is shown in Fig. 6.10. Compared to the existing spherical beamformers such as those in [42, 93, 97, 98], the filtering block has been moved to the sensor end in the proposed design. The proposed structure in Fig. 6.10 can be regarded as a filter-and-sum beamformer where

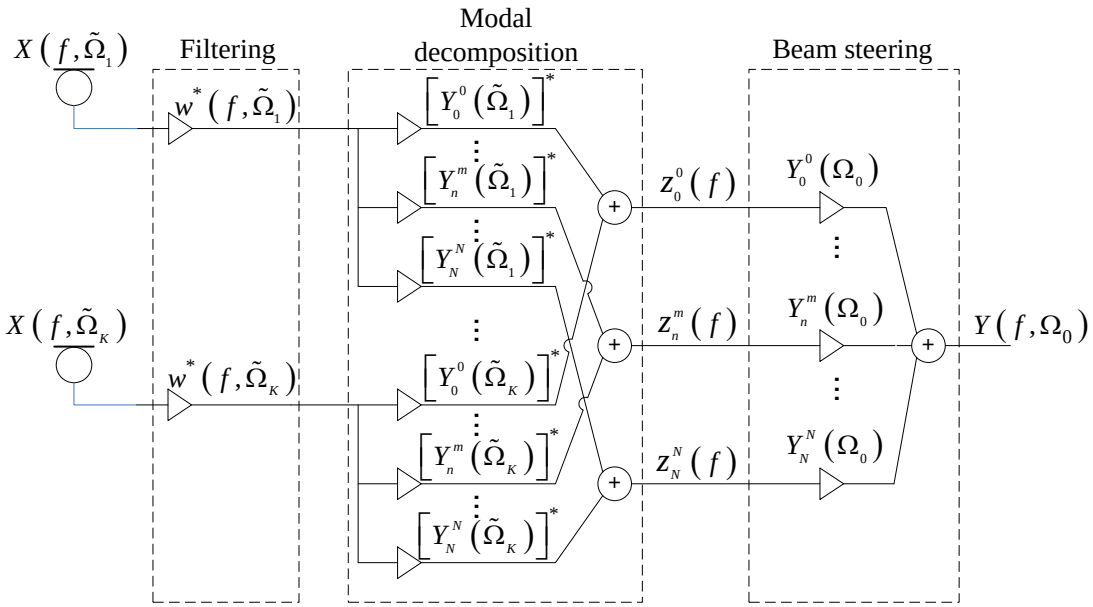

Figure 6.10: Proposed frequency domain beamformer structure.

the individual filter outputs are decomposed into orthogonal modes for beam steering. The shift of the filtering block allows arbitrary sensor configuration as in conventional filter-and-sum beamformers, and the retention of the spherical harmonics decomposition and steering block allows simple beam steering with invariant beampattern.

It is known that the performance of beamformers will degrade in the presence of errors and their robustness can be measured in terms of WNG [74, 93]. In the presence of spatially uncorrelated white noise with power spectral density σ_n^2, and no other noise terms, the output power of the proposed beamformer is given by

$$P_n(f) = \sigma_n^2 \sum_{s=1}^{K} \left| w\left(f, \tilde{\Omega}_s\right) \right|^2. \tag{6.40}$$

The WNG is then given by

$$WNG(f) = \frac{\sigma_n^2}{P_n(f)} = \frac{1}{\mathbf{w}^{\mathrm{H}}(f)\,\mathbf{w}(f)}. \tag{6.41}$$

A constraint based on (6.41) can then be included into the design (by minimising the 2-norm distance squared between $\mathbf{B}(ka)\,\mathbf{Y}\mathbf{w}(f)$ and $\boldsymbol{\alpha}(f)$) to improve

robustness as follows

$$\begin{aligned} \min_{\mathbf{w}(f)} \quad & \left\| \mathbf{B}(ka)\,\mathbf{Y}\mathbf{w}(f) - \boldsymbol{\alpha}(f) \right\|_2^2 \\ \text{subject to} \quad & WNG^{-1}(f) \leq \rho(f) \end{aligned} \tag{6.42}$$

where $\rho(\cdot)$ is a design parameter. The design problem (6.42) can be solved using optimisation toolboxes such as SeDuMi [106].

6.4.2 Time domain design

The frequency domain design in Section 6.4.1 can be transformed into the time domain. For the ideal case, i.e. continuous sensor array with continuous-time non-causal filters, the impulse response of the proposed beamformer design is given by (from (6.27))

$$h\left(t, \tilde{\Omega}\right) = F^{-1}\left\{ S^{-1}\left\{ \left[\frac{\alpha_n^m(f)}{b_n(ka)} \right]^* \right\} \right\} \tag{6.43}$$

where $F\{\cdot\}$ is the Fourier transform.

In the case of discrete-time implementation, the impulse response (6.43) is sampled at sampling frequency f_S and truncated to finite length. These operations are equivalent to approximating each of the frequency dependent complex weight in (6.29) with a real L-tap FIR filter, i.e.

$$w^*\left(f, \tilde{\Omega}_s\right) \approx \mathbf{h}_s^{\mathrm{T}} \mathbf{e}(f), \qquad |f| < \frac{f_S}{2} \tag{6.44}$$

where

$$\mathbf{h}_s = \left[h_s(0), h_s(1), ..., h_s(L-1) \right]^{\mathrm{T}}, \tag{6.45}$$

$$\mathbf{e}(f) = \left[1, \exp\left(-i\frac{2\pi f}{f_S} \right), ..., \exp\left(-i\frac{2\pi f\,(L-1)}{f_S} \right) \right]^{\mathrm{T}}. \tag{6.46}$$

In order to compensate for the inherent group delay in FIR filters, a negative predelay, typically chosen as [97]

$$\eta(f) = \exp\left(i\frac{\pi f\,(L-1)}{f_S} \right) \tag{6.47}$$

is also added to (6.29) to yield, for the time domain design, the beampattern expression

$$\mathcal{B}(f, \Omega, \Omega_0) = \sum_{n=0}^{N} \sum_{m=-n}^{n} \left(b_n(ka) \sum_{s=1}^{K} \eta(f)\, \mathbf{h}_s^{\mathrm{T}} \mathbf{e}(f)\, Y_n^m\left(\tilde{\Omega}_s\right) \right) \left[Y_n^m(\Omega) \right]^* Y_n^m(\Omega_0). \tag{6.48}$$

The weights design expression is then given by

$$b_n(ka)\sum_{s=1}^{K}\eta(f)\,\mathbf{h}_s^{\mathrm{T}}\mathbf{e}(f)\,Y_n^m\left(\tilde{\Omega}_s\right)=\alpha_n^m(f)\quad\forall n,m\,,\ f\in\Omega_{pb}. \tag{6.49}$$

Note that the term $\eta(f)$, which cannot be realized in practice, is only required to determine the beamformer weights during the design stage and is not required in the actual implementation of the beamformer. Let $\mathbf{h}=\left[\mathbf{h}_1^{\mathrm{T}},...,\mathbf{h}_K^{\mathrm{T}}\right]^{\mathrm{T}}$. Equation (6.49) can then be rewritten in matrix form as

$$\left(\left(\mathbf{B}(ka)\,\mathbf{Y}\right)\otimes\left(\eta(f)\,\mathbf{e}^{\mathrm{T}}(f)\right)\right)\mathbf{h}=\boldsymbol{\alpha}(f)\quad\forall f\in\Omega_{pb}. \tag{6.50}$$

Suppose the frequency range Ω_{pb} in (6.50) is discretised into $M>KL$ points and let

$$\mathbf{A}=\Big[\left(\left(\mathbf{B}(k_1a)\,\mathbf{Y}\right)\otimes\left(\eta(f_1)\,\mathbf{e}^{\mathrm{T}}(f_1)\right)\right)^{\mathrm{T}},...,\left(\left(\mathbf{B}(k_Ma)\,\mathbf{Y}\right)\otimes\left(\eta(f_M)\,\mathbf{e}^{\mathrm{T}}(f_M)\right)\right)^{\mathrm{T}}\Big]^{\mathrm{T}}, \tag{6.51}$$

$$\boldsymbol{\alpha}=\left[\boldsymbol{\alpha}^{\mathrm{T}}(f_1),\boldsymbol{\alpha}^{\mathrm{T}}(f_2),...,\boldsymbol{\alpha}^{\mathrm{T}}(f_M)\right]^{\mathrm{T}}, \tag{6.52}$$

(6.50) can be written compactly as

$$\mathbf{A}\mathbf{h}=\boldsymbol{\alpha}. \tag{6.53}$$

Solving (6.53) in the least squares sense, while constraining $\mathbf{h}$ to be real, $\mathbf{h}\in\mathbb{R}^{KL}$, yields

$$\mathbf{h}=\mathrm{Re}\left\{\mathbf{A}^{\mathrm{H}}\mathbf{A}\right\}^{-1}\mathrm{Re}\left\{\mathbf{A}^{\mathrm{H}}\boldsymbol{\alpha}\right\} \tag{6.54}$$

where $\mathrm{Re}\{\cdot\}$ denotes the real part of its argument. The implementation structure of the proposed time domain beamformer can be derived following the same procedure described in [97]. The time domain output signal of the beamformer is given by

$$y(l)=\sum_{n=0}^{N}\sum_{s=1}^{K}\left(x_s(l)\star h_s(l)\right)\sum_{m=-n}^{n}\left[Y_n^m\left(\tilde{\Omega}_s\right)\right]^*Y_n^m(\Omega_0) \tag{6.55}$$

where $\star$ denotes convolution. The summation of complex spherical harmonics for

$m = -n, ..., n$ in (6.55) can be expanded into summation of only real terms as in

$$\begin{aligned}
&\sum_{m=-n}^{n} \left[Y_n^m\left(\tilde{\Omega}_s\right)\right]^* Y_n^m\left(\Omega_0\right) \\
&\quad = Y_n^0\left(\tilde{\Omega}_s\right) Y_n^0\left(\Omega_0\right) + 2\sum_{m=1}^{n} \Big(\mathrm{Re}\left\{Y_n^m\left(\tilde{\Omega}_s\right)\right\} a_n^m P_n^m\left(\cos\left(\theta_0\right)\right)\cos\left(m\phi_0\right) \\
&\qquad +\mathrm{Im}\left\{Y_n^m\left(\tilde{\Omega}_s\right)\right\} a_n^m P_n^m\left(\cos\left(\theta_0\right)\right)\sin\left(m\phi_0\right)\Big)
\end{aligned} \tag{6.56}$$

where

$$a_n^m = \sqrt{\frac{(2n+1)}{4\pi}\frac{(n-m)!}{(n+m)!}}. \tag{6.57}$$

Substituting (6.56) into (6.55) results in a real expression for the time domain output signal of the modal beamformer. The resulting implementation structure is shown in Fig. 6.11.

The noise-only beamformer output power (in the only presense of spatially uncorrelated white noise with power spectral density σ_n^2) is [97]

$$\begin{aligned}
\bar{P}_n &= \int_{\Omega} P_n\left(f\right) df \\
&= \sum_{s=1}^{K} \int_{\Omega} \sigma_n^2 \left|\mathbf{h}_s^{\mathrm{T}}\mathbf{e}\left(f\right)\right|^2 df \\
&= \sigma_n^2 \mathbf{h}^{\mathrm{T}}\mathbf{h}.
\end{aligned} \tag{6.58}$$

Its WNG is then given by

$$WNG = \frac{\sigma_n^2}{\bar{P}_n} = \frac{1}{\mathbf{h}^{\mathrm{T}}\mathbf{h}}. \tag{6.59}$$

Robustness in the design can be achieved by constraining (6.59) while minimising the 2-norm distance squared between $\mathbf{Ah}$ and $\boldsymbol{\alpha}$, resulting in

$$\begin{aligned}
\min_{\mathbf{w}(f)} \quad & \left\|\mathbf{Ah} - \boldsymbol{\alpha}\right\|_2^2 \\
\text{subject to} \quad & WNG^{-1} \leq \rho.
\end{aligned} \tag{6.60}$$

As with (6.42) the above design problem can be solved using optimisation toolboxes such as SeDuMi.

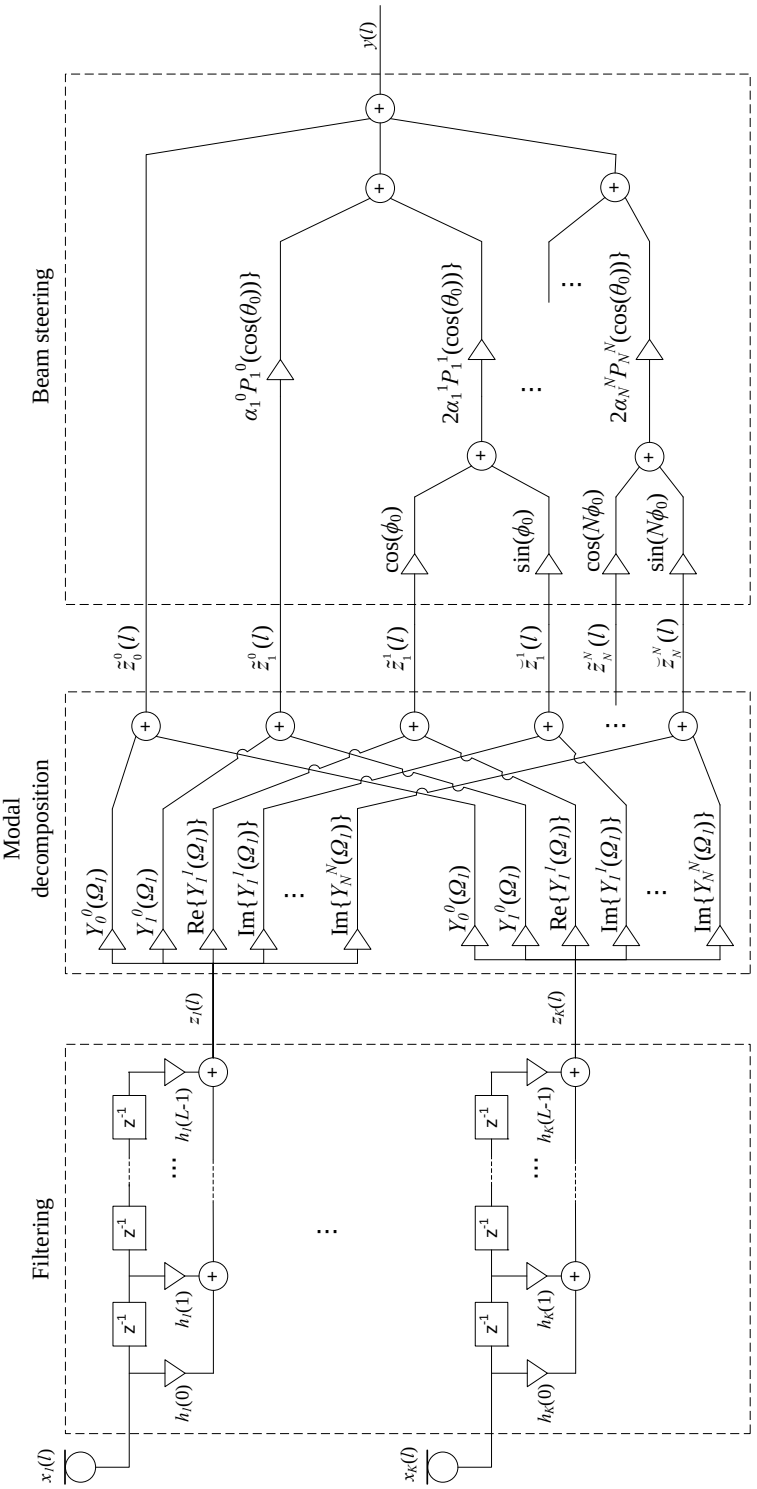

Figure 6.11: Proposed time domain beamformer structure.

6.5 Properties of the proposed beamformer

6.5.1 Independence of orthonormality criterion

The expressions for the proposed beamformer weights design in (6.37) and (6.54) are derived with no reference to the orthonormality criterion (6.14). This means that unlike the existing spherical beamformer designs, the proposed beamformer is not restricted by the criterion and hence, failure to satisfy it will not affect the performance of the proposed beamformer. In other words, in the proposed beamformer, the sensor placement can follow any arbitrary array configuration as long as the sensors are reasonably spread out. This provides freedom and flexibility in the sensor configuration, especially in cases where it is not possible to satisfy (6.14) or where an irregular spherical array is required.

6.5.2 Reduction in number of sensors

In the frequency domain design, the beamformer weights $w^*\left(f, \tilde{\Omega}_s\right)$ are required to satisfy (6.29) for all $n = 0, ..., N$ and $m = -n, ..., n$. Its matrix equivalent, given in (6.35), shows that it is indeed a linear system with $(N+1)^2$ equations. Hence, in order to satisfy all $(N+1)^2$ equations in (6.35), the length of the weight vector $\mathbf{w}(f)$ must be at least $(N+1)^2$. In other words, $K \geq (N+1)^2$ sensors are required to resolve spherical harmonics up to order N without any spatial aliasing. Compared to the existing spherical beamformer designs which use the sampling schemes discussed in Section 6.3, the proposed beamformer design requires fewer sensors. This is favourable in applications where the cost and number of sensors is a limiting factor, such as small, low cost spherical arrays.

As for the time domain design, which is merely an approximation of the frequency domain counterpart, it inherits the same properties. This is because they both have the same structure except for the filtering block (see Figs. 6.10 and 6.11), where FIR filters are used to approximate the frequency dependent weights in the frequency domain design. Hence, as long as the length of the FIR filters is sufficiently long to provide a close approximation of the complex weights, the minimum number of required sensors is also $(N+1)^2$.

6.5.3 Steerability of main-beam

Suppose the design expression given by (6.29) for frequency domain, or (6.49) for time domain, is satisfied completely. Then, both the beampattern expressions (6.28) and (6.48) will equal exactly to the desired beampattern (6.24). Since (6.24) is identical to the beampattern expressions in [42, 97], this means the proposed beamformer design can be steered in the same way as the existing spherical beamformer designs, i.e. by modulating with $Y_n^m(\Omega_0)$, without affecting its beampattern.

6.5.4 Effect of array rotation

In the proposed design, the beamformer weights depend on the position of the sensors. Accordingly, the orientation of the sensor array will affect its beampattern, which is not the case with the existing spherical beamformers. In order to analyse this effect, an array rotation of $\Omega_r = (\theta_r, \phi_r)$ is introduced into (6.23), which yields

$$B(f, \Omega, \Omega_0) = \sum_{n=0}^{\infty} \sum_{m=-n}^{n} \left(b_n(ka) \oint_{\tilde{\Omega} \in S^2} w^* \left(f, \tilde{\Omega} \right) Y_n^m \left(\tilde{\Omega} + \Omega_r \right) d\tilde{\Omega} \right) \times \left[Y_n^m(\Omega) \right]^* Y_n^m(\Omega_0). \tag{6.61}$$

Note that to avoid any approximation error in the analysis, due to the discretisation of the sensors and temporal sampling, (6.23) is used instead of (6.28) or (6.48) in (6.61). Note also that the term Ω_r is not introduced in the weights $w^* \left(f, \tilde{\Omega} \right)$ since the weights are fixed after the design. Substituting (6.3) into (6.61), it can be shown that

$$B(f, \Omega, \Omega_0) = \sum_{n=0}^{\infty} \sum_{m=-n}^{n} \left(b_n(ka) \oint_{\tilde{\Omega} \in S^2} w^* \left(f, \tilde{\Omega} \right) Y_n^m \left(\tilde{\theta} + \theta_r, \tilde{\phi} \right) d\tilde{\Omega} \right) \times \left[Y_n^m(\Omega) \right]^* Y_n^m(\theta_0, \phi_0 + \phi_r). \tag{6.62}$$

For $\theta_r = 0$, (6.62) shows that a mechanical rotation of the array by ϕ_r in the azimuth plane results merely in a rotation of the beampattern in that plane by the same angle (c.f. (6.23)).

Unfortunately, a similar property does not hold for rotation in elevation, since θ_r is embedded in the argument of the associated Legendre polynomials (see (6.3)). Using (6.27), the integral term in (6.62) becomes

$$\oint_{\tilde{\Omega}\in S^2} w^*\left(f,\tilde{\Omega}\right) Y_n^m\left(\tilde{\theta}+\theta_r,\tilde{\phi}\right) d\tilde{\Omega} = \sum_{n=0}^{\infty}\sum_{m=-n}^{n} \frac{\alpha_n^m(f)}{b_n(ka)} \oint_{\tilde{\Omega}\in S^2} \left[Y_n^m\left(\tilde{\Omega}\right)\right]^* Y_n^m\left(\tilde{\theta}+\theta_r,\tilde{\phi}\right) d\tilde{\Omega}. \quad (6.63)$$

Since $\left[Y_n^m\left(\tilde{\Omega}\right)\right]^*$ and $Y_n^m\left(\tilde{\theta}+\theta_r,\tilde{\phi}\right)$ in (6.63) are no longer orthogonal, this means that rotation in elevation will distort the beampattern. However, in most applications, this effect is minor since for small values of θ_r, the distortion is negligible as illustrated in Section 6.6.3.

6.5.5 Computational complexity

In order to compare the computational complexity of the proposed spherical beamformer to the existing spherical beamformers, the computational complexity is assessed in terms of number of real multiplications (RM) and real additions (RA). It is assumed that a single complex multiplication is equivalent to 4 RMs and 2 RAs while a complex addition is equivalent to 2 RAs. It is further assumed that all weights, such as the beamformer weights and the spherical harmonic coefficients for modal decomposition and beam steering have been precomputed and stored in memory. Table 6.1 compares the required number of RMs and RAs for the proposed frequency domain spherical beamformer design against the existing design of [42]. The required number of RMs and RAs is per frequency bin. Table 6.2 compares the computational complexity of the proposed design in time domain against the existing design of [97], where the required number of RMs and RAs is for the whole spectral range of interest.

Table 6.1: Comparison of computational complexity for frequency domain design.

System block		Existing	Proposed
Modal decomposition	RM	$4K\left(N+1\right)^2$	$4K\left(N+1\right)^2$
	RA	$2\left(2K-1\right)\left(N+1\right)^2$	$2\left(2K-1\right)\left(N+1\right)^2$
Beam steering	RM	$4\left(N+1\right)^2$	$4\left(N+1\right)^2$
	RA	$2\left(2N+1\right)\left(N+1\right)$	$4\left(N+1\right)^2-2$
Filtering	RM	$4\left(N+1\right)$	$4K$
	RA	$2\left(2N+1\right)$	$2K$
Total	RM	$4\left(\left(K+1\right)\left(N+1\right)^2+\left(N+1\right)\right)$	$4\left(\left(K+1\right)\left(N+1\right)^2+K\right)$
	RA	$2\left(\left(2K+1\right)\left(N+1\right)^2+N\right)$	$2\left(\left(2K+1\right)\left(N+1\right)^2+K-1\right)$

Table 6.2: Comparison of computational complexity for time domain design.

System block		Existing	Proposed
Modal decomposition	RM	$K\left(N+1\right)^2$	$K\left(N+1\right)^2$
	RA	$\left(K-1\right)\left(N+1\right)^2$	$\left(K-1\right)\left(N+1\right)^2$
Beam steering	RM	$\left(3N^2+5N\right)/2$	$\left(3N^2+5N\right)/2$
	RA	$N\left(N+1\right)$	$N\left(N+2\right)$
Filtering	RM	$L\left(N+1\right)$	KL
	RA	$L\left(N+1\right)-1$	$K\left(L-1\right)$
Total	RM	$\left(N+1\right)\left(K\left(N+1\right)+\frac{3}{2}N\right)+N+L\left(N+1\right)$	$\left(N+1\right)\left(K\left(N+1\right)+\frac{3}{2}N\right)+N+KL$
	RA	$KN\left(N+2\right)-1+\left(N+1\right)\left(L-1\right)+K$	$KN\left(N+2\right)-1+KL$

For a given K, N and L with $N < K$, it seems the proposed method will result in a higher computational load. However, if the orthonormality criterion is taken into account, i.e. for the existing designs, a minimum of $K = 1.5\,(N+1)^2$ sensors are required [105], whereas for the proposed design, a minimum of $K = (N+1)^2$ sensors are required, then a different conclusion can be drawn. For the frequency domain design, the proposed design has a lower computational load compared to the existing designs in all cases as shown in Fig. 6.12. For the time domain designs, the proposed design achieves lower computational load if

$$L < \frac{(N+1)^3}{2N} \tag{6.64}$$

where (6.64) is obtained by equating the corresponding total RM and RA counts from Table 6.2 after substituting $K = 1.5\,(N+1)^2$ for the existing method and $K = (N+1)^2$ for the proposed method. For example, to design a beamformer with spherical harmonic order of $N = 5$, the proposed design has a computational advantage if the filter length is chosen to be $L < 21.6$. This dependency on the filter length L is shown in Fig. 6.13, where the dashed lines, plotted for $L \in [4, 5152]$, represent the locations where the number of operations for both the proposed and the existing designs coincide for different values of L. The region below the dashed line is where the proposed method has a computational advantage.

6.6 Performance evaluations and discussions

In order to illustrate the performance of the proposed method, a number of time domain design examples based on (6.54) are presented. The design parameters are specified in Table 6.3, where the sensors are assumed to be omni-directional microphones mounted on a rigid sphere.

As for the sensor configurations, a quasi-uniform configuration [102] shown in Fig. 6.14 and a random configuration shown in Fig. 6.15 are considered. The sensor positions for the random configuration are given by

$$\tilde{\theta}_s = \cos^{-1}(2u-1), \quad \tilde{\phi}_s = 2\pi v \tag{6.65}$$

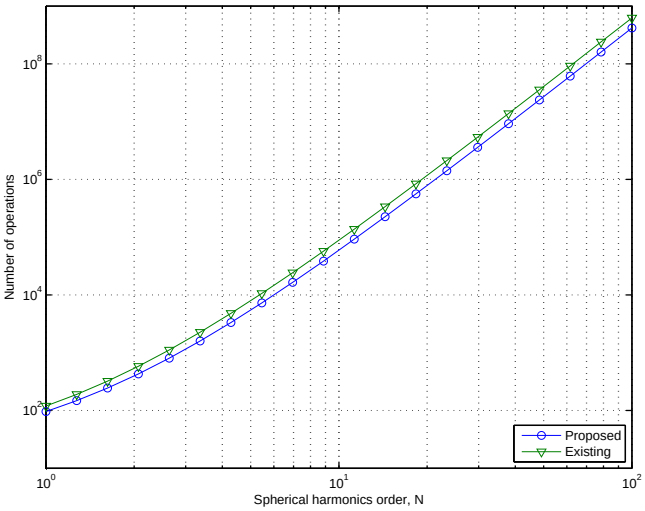

(a) Real multiplication.

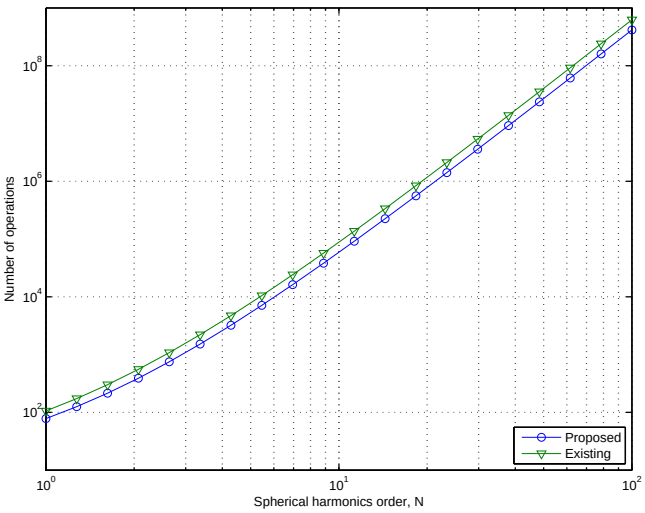

(b) Real addition.

Figure 6.12: Comparison of required number of real multiplications and additions for frequency domain designs.

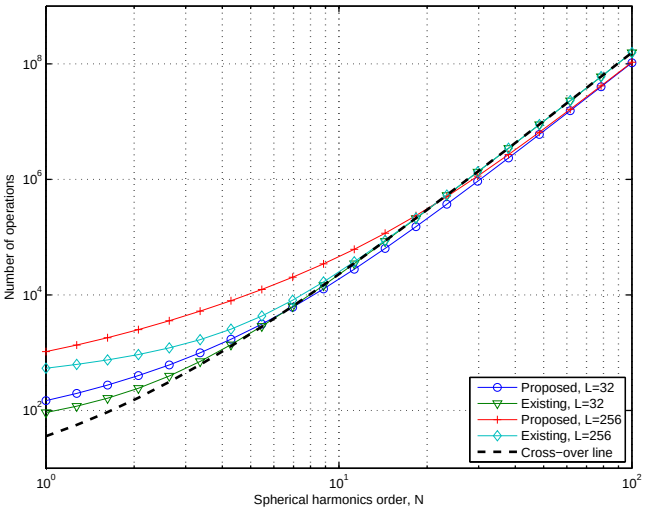

(a) Real multiplication.

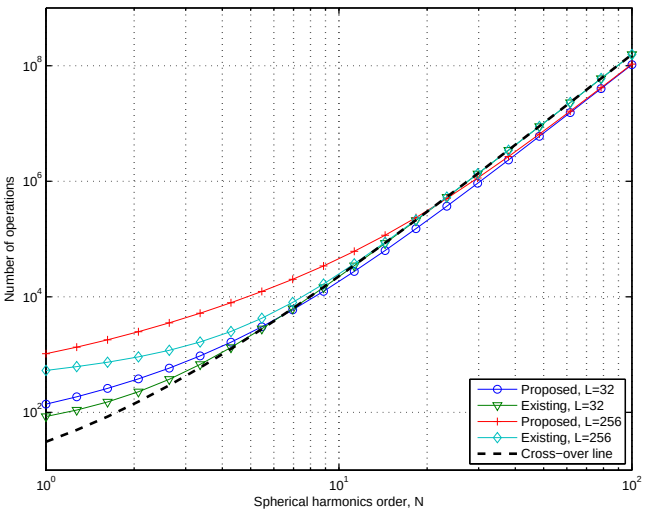

(b) Real addition.

Figure 6.13: Comparison of required number of real multiplications and additions for time domain designs.

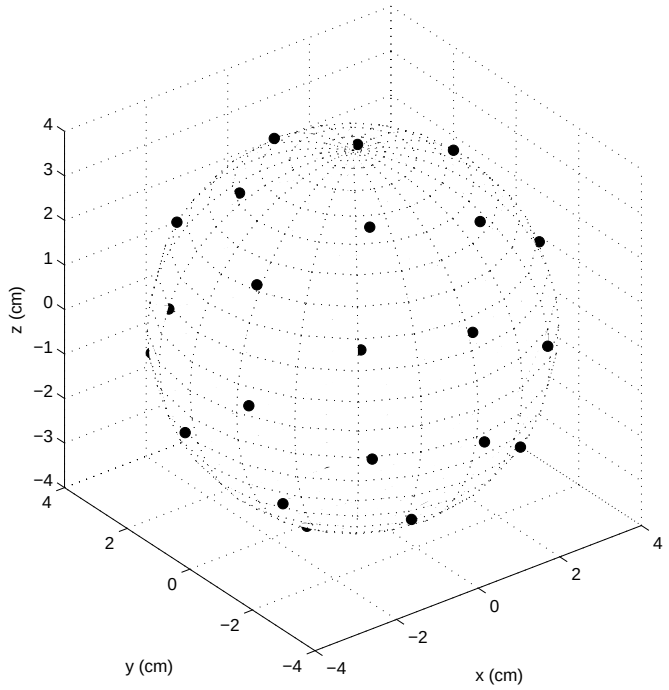

Figure 6.14: Uniform microphone configuration.

where $u, v \sim \mathcal{U}(0,1)$, in order to have sensors uniformly distributed over the surface of the sphere [107].

6.6.1 Sensor configurations and orthonormality criterion

In this section, the limitation imposed by the orthonormality criterion (6.14) on the existing methods is illustrated. For the uniform sensor configuration shown in Fig. 6.14, it has the absolute error squared of the orthonormality criterion as shown in Fig. 6.16, which is defined as

$$e(n,m,n',m') = \left| \sum_s \alpha_s \left[Y_n^m \left(\tilde{\Omega}_s \right) \right]^* Y_{n'}^{m'} \left(\tilde{\Omega}_s \right) - \delta_{m-m'} \delta_{n-n'} \right|^2, \tag{6.66}$$

where the index k is defined as $k = n(n+1) + m + 1$, and k' is defined similarly. The dark blue patch on the upper left corner of Fig. 6.16 shows that the uniform configuration satisfies (6.14) up to around $k \leq 21 \cap k' \leq 21$ (which corresponds to $N = 3$, rounded down). For k and $k' > 21$, the violation of the orthonormality

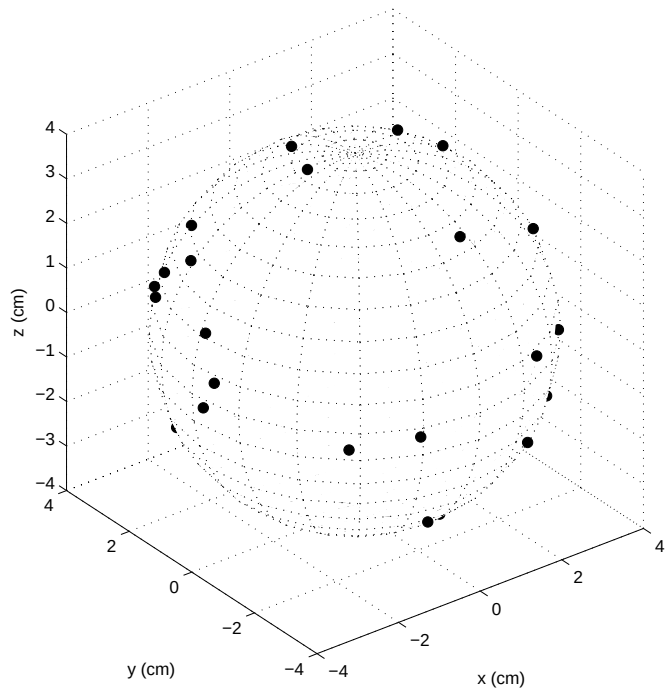

Figure 6.15: Random microphone configuration.

Table 6.3: Design parameters.

Parameters	**Value**
Highest spherical harmonics order, N	5
Number of microphone, K	36
FIR filter length, L	64
Sampling frequency, f_S	8000 Hz
Spectral passband, Ω_{pb}	$[200, 3800]$ Hz
Radius of spherical array, a	4 cm

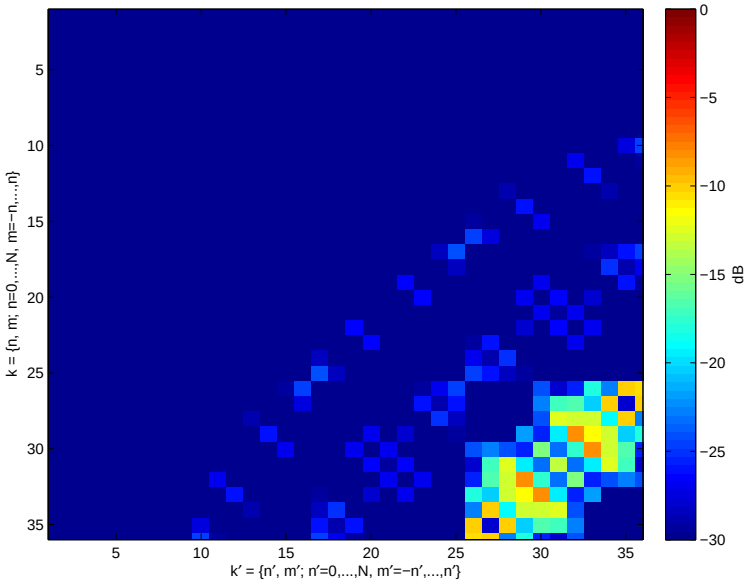

Figure 6.16: Plot of (6.66) for uniform microphone configuration.

criterion increases as indicated by the appearances of coloured patches (indicating large error) in the lower right corner. This limits the operable order of the existing beamfomer to $N = 3$ (where the low frequency components start to increase), as shown by the beampatterns in Fig. 6.18, evaluated for $N = 2$ and $N = 3$ using the existing method of [97]. This limiting factor was discussed by Hardin and Sloane [105].

In the case of the proposed method, given the same number of sensors ($K = 36$), more spherical harmonics (up to $N = 5$) can be resolved without any spatial aliasing. This is shown by Fig. 6.19, which depicts the beampattern obtained from the proposed method using the same uniform sensor configuration of Fig. 6.14. Moreover, consider the random configuration shown in Fig. 6.15 with its orthonormality error (6.66) shown in Fig. 6.17. The coloured spots (indicating large error) in Fig. 6.17 clearly show that the random configuration does not satisfy the orthonormality criterion (6.14) at all. However, the proposed method can still be used to design a modal beamformer up to $N = 5$ order of spherical harmonics. The beampattern of such a design is shown in Fig. 6.20.

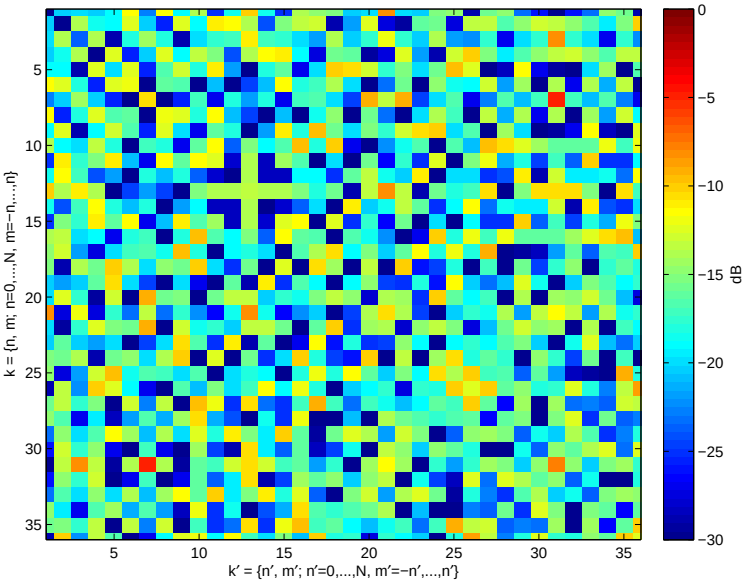

Figure 6.17: Plot of (6.66) for random microphone configuration.

6.6.2 Steerability performance

In this section, the ability of the proposed method to employ any arbitrary sensor configuration without sacrificing its steerability and performance is illustrated and compared against the design method of [97]. For the proposed method, the sensor configurations shown in Figs. 6.14 and 6.15 are employed. As for the existing method, it is assumed that (6.14) holds completely up to $N = 5$, either using the equiangle or Gaussian sampling scheme (see Section 6.3).

The performance of the designs are evaluated in terms of the integral of directivity covering the whole range $\Omega_0 \in \{\theta_0, \phi_0 : 0 \leq \theta_0 \leq \pi, 0 \leq \phi_0 \leq 2\pi\}$, given by

$$D(f) = \oint_{\Omega_0} D(f, \Omega_0)\, d\Omega_0 \tag{6.67}$$

where the directivity $D(f, \Omega_0)$ is defined as [59]

$$D(f, \Omega_0) = \frac{4\pi \left|B(f, \Omega_0, \Omega_0)\right|^2}{\int_\Omega \left|B(f, \Omega, \Omega_0)\right|^2 d\Omega}. \tag{6.68}$$

Fig. 6.21 shows the integral of DI (6.67) of the proposed designs compared against the existing design. The figure shows that the proposed designs, though using sensor configurations that do not satisfy (6.14) (see Figs. 6.16 and 6.17), still have similar performance as the existing design (except for the a slight degradation at low frequencies). This means the proposed designs are not limited

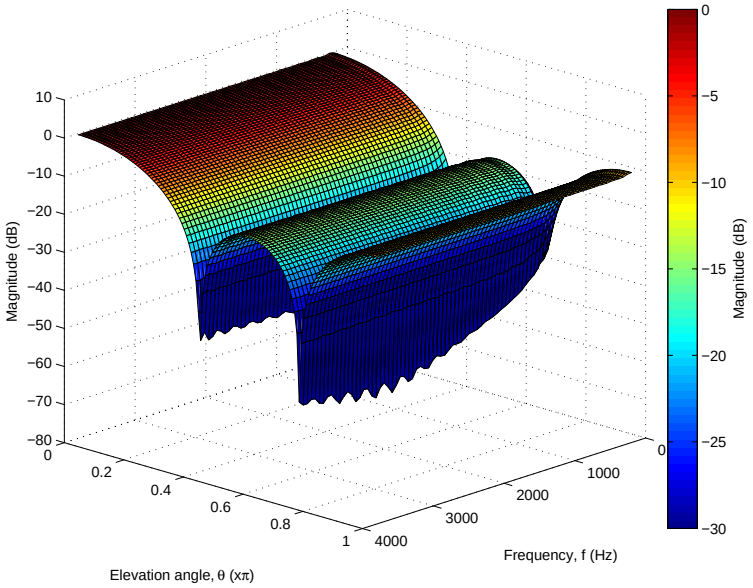

(a) N=2.

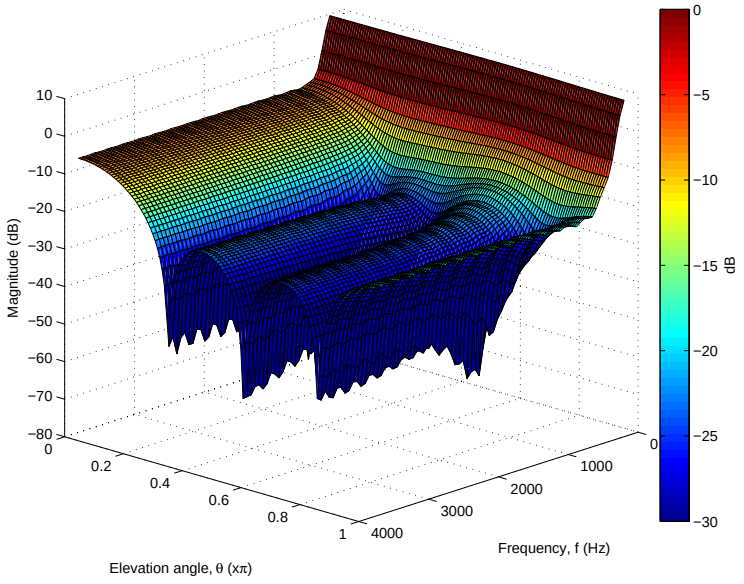

(b) N=3.

Figure 6.18: Beampattern for the existing design (uniform sensor configuration) steered to $\Omega_0 = (0, 0)$, evaluated for $N = 2$ and $N = 3$.

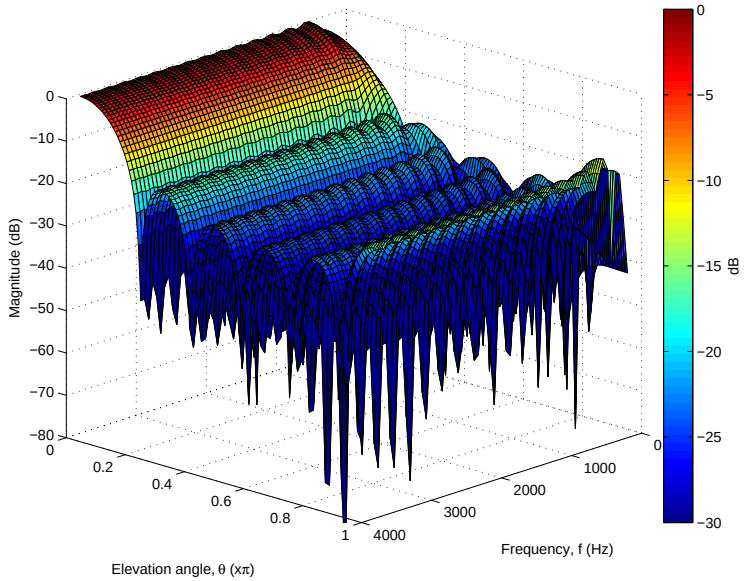

Figure 6.19: Beampattern for the proposed design (uniform sensor configuration) steered to $\Omega_0 = (0, 0)$ and evaluated for $N = 5$.

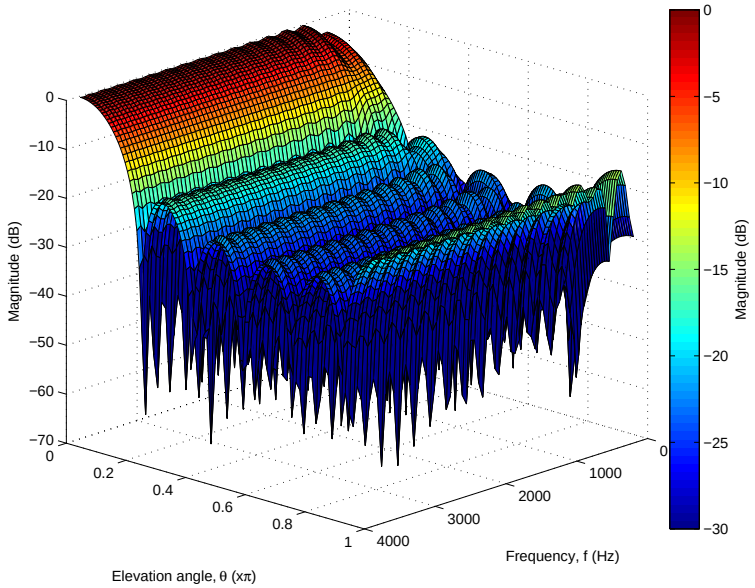

Figure 6.20: Beampattern for the proposed design (random sensor configuration) steered to $\Omega_0 = (0, 0)$ and evaluated for $N = 5$.

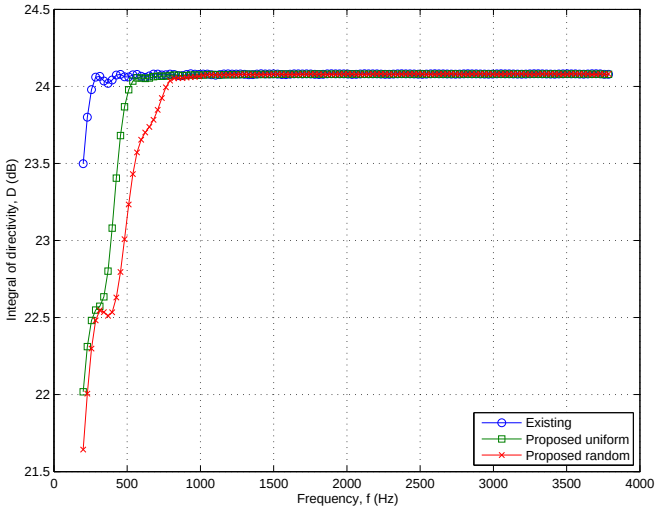

Figure 6.21: Plot of (6.67) using the proposed and existing design methods.

by the orthonormality criterion (6.14), and yet, are able to achieve similar steerability performance as the existing method.

The WNG for the non-robust and robust designs are shown in Fig. 6.22. Low WNG indicates that the beamformers are not robust, and this happens at the low frequencies of the non-robust designs. For the robust designs, their WNG measures are high and constant indicating their robustness (especially at low frequencies).

6.6.3 Performance with rotated array

In order to illustrate the discussion in Section 6.5.4, the beampattern (for frequency, $f = 2$kHz) of the proposed beamformer with random sensor configuration, steered to $\Omega_0 = ({}^{3\pi}/_4, {}^{\pi}/_3)$ is shown in Fig. 6.23. The beampattern with the same beamformer, but with its sensor array rotated by $\Omega_r = (0, {}^{\pi}/_3)$ around the azimuth plane, is shown in Fig. 6.24. The main-beam, under steering and array rotation, is now located at $\Omega_0 + \Omega_r$ (compare Fig. 6.23 with 6.24).

As for the effect of array rotation in elevation, Fig. 6.25 shows the directivity (6.68) of the beamformer with an array rotation of $\theta_r \in [0, \pi]$ and $\phi_r = 0$. Although the array rotation in elevation will decrease the beamformer's DI, the effect is minor for small θ_r. For example, for a 1dB drop in DI, the range of θ_r is

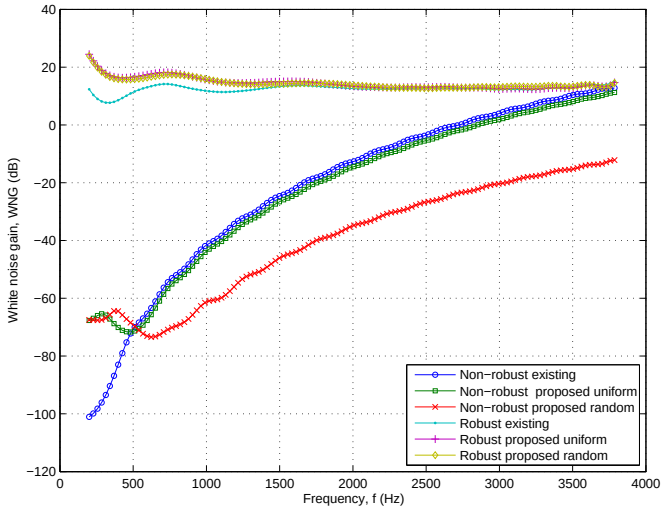

Figure 6.22: WNG measures for non-robust and robust (with $\rho = 2$) designs.

around $0 \leq \theta_r \leq 0.3\pi$.

6.7 Conclusions

A design method based on spherical harmonics for filter-and-sum beamformers with straightforward steering capability has been proposed. The proposed method allows for flexibility in sensor configuration and straightforward beam steering with a beampattern that is invariant to the steering direction. Flexibility in the sensor configuration to allow arbitrary configurations is achieved through the filter-and-sum beamformer while the straightforward steering property of spherical harmonic beamforming is achieved through spherical harmonic decomposition and modulation. In addition, it is shown that the proposed method requires fewer sensors to achieve similar performance as the existing spherical harmonic beamformers for the same order of spherical harmonics. The main trade-off of the proposed method, as compared to the existing beamformers, is that prior knowledge of the sensor positions are required, which results in its beampattern being dependent on the array orientation. However, the effect of such dependency is minor since small changes in the array orientation does not cause significant distortion to the beampattern. Robustness of the proposed designs can be achieved by constraining its WNG.

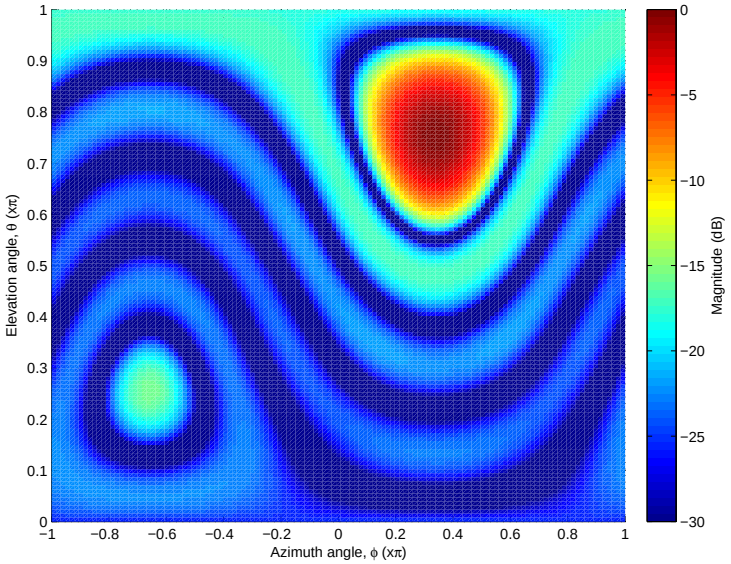

Figure 6.23: Beampattern (at $f = 2$kHz) of proposed design (random sensor configuration) steered to $\Omega_0 = (3\pi/4, \pi/3)$.

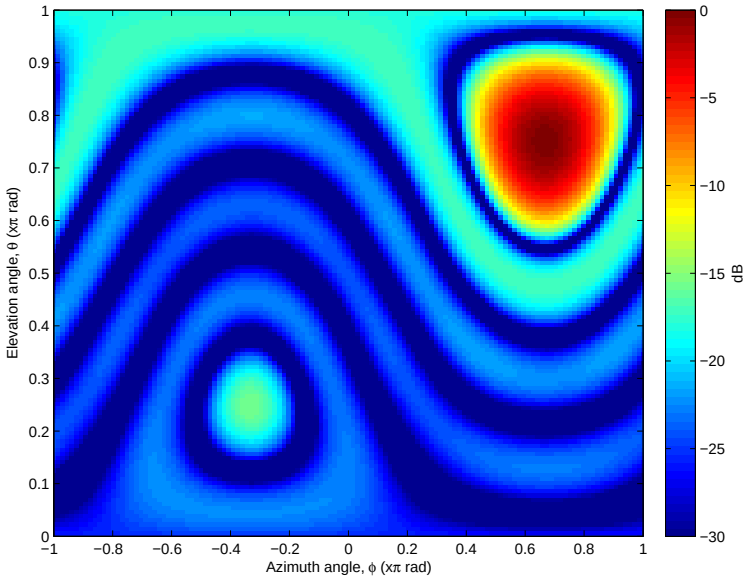

Figure 6.24: Beampattern (at $f = 2$kHz) of proposed design (random microphone configuration) steered to $\Omega_0 = (3\pi/4, \pi/3)$ and with array rotation of $\Omega_r = (0, \pi/3)$.

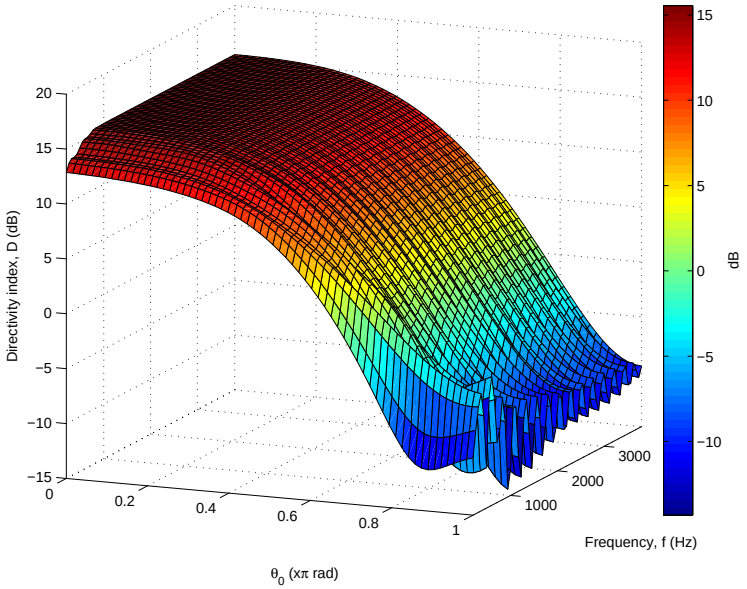

Figure 6.25: DI of proposed design (random microphone configuration) with array rotation of $\theta_r \in [0, \pi]$ and $\phi_1 = 0$.

Chapter 7

Conclusions and Future Work

7.1 Summary

This thesis presents a study on the design of steerable broadband beamformers, where the main-beam of the beamformers can be steered electronically and simply without any mechanical movement of the actual array. By simple steering, it is meant that steering can be achieved without the need to redesign or change the beamformer weight whenever the look direction of the main-beam changes. This allows on-the-fly continuous steering of the main-beam and in conjunction with an appropriate tracking algorithm, can be used to follow moving signal sources in applications such as automatic audio reception, audio surveillance and robotic auditory systems.

Preliminary design decisions on the physical attributes of the beamformers are discussed in Chapter 2. These include the selection of array geometries, signal propagation models and beamformer structures. In general, such design decisions depend heavily on the target applications and there is no single global solution for all applications. Each model and structure has its own merits and drawbacks. Accordingly, care must be exercised when making these choices in order to avoid the known limitations of certain models or structures and to maximise the overall performance of the beamformers.

Chapter 3 presents the design formulations of SBBFs in both the weighted LS and weighted TLS sense. For each formulation, both frequency domain and time

domain designs are also provided. The beamformer structure used for formulating the design of SBBFs is the Farrow filter structure where the free parameter is used to steer the main-beam in the azimuthal plane and the FIR filters are used to achieve frequency invariant responses. The array geometry used is a spiral arm array, which is a type of concentric multi-ring circular array. One of the major benefits of this array geometry is its circular symmetry, which can be exploited to allow the main-beam of the beamformer to cover the whole azimuthal plane by appropriately rotating the beamformer weights.

The design formulations in Chapter 3, which are non-robust, are extended in Chapter 4 to include robustness against errors and perturbations in the design model. A stochastic error model approach is developed and integrated into SBBFs design formulation by modelling the errors in the sensor gain and phase as random variables. This model is capable of capturing the perturbations and mismatches in practical setups. The mean performance of the beamformers in the presence of errors and perturbations are optimised to achieve robustness. This technique effectively embeds the error and perturbation model into the design formulation and thus allows the standard non-robust design technique to be used directly to achieve robust designs.

The SBBFs in Chapter 3, which is formulated with either a nearfield or farfield source (but not their combination), is extended in Chapter 5 to design SBBFs that work for both nearfield and farfield sources. This extension results in beamformers with invariant response over a wide range of source radial distances, covering both nearfield and farfield distances. Hence, regardless of the signal source moving from the farfield region to the nearfield region (moving closer to the sensor array) or vice versa, the resulting beamformers are still operable. Robustness in the beamformer designs can be achieved similarly using the robust design technique discussed in Chapter 4. Essentially, apart from achieving operability for both nearfield and farfield sources, the steerability, broadband capability and robustness properties are maintained in the design formulation.

Chapter 6 discusses a design method for azimuth-elevation steerable broadband beamformers for spherical arrays based on spherical harmonics and the conventional filter-and-sum beamformer structure. The filter-and-sum structure

allows for arbitrary sensor configuration while beam steering through spherical harmonics provides straightforward beam steering with beampatterns that are invariant to the steering direction. Beam steering is achieved by decomposing the outputs of the filter-and-sum beamformer structure into orthogonal components and modulating these components to the desired look direction.

7.2 Future work

1. **Tracking beamformer**

   One of the interesting future directions of the work presented in this thesis is to integrate a source detection and tracking algorithm [23, 24, 108] together with the steerable beamformer for automatic audio reception with source tracking capability [109]. Such integration is depicted in Fig. 7.1 where the output of source tracking system, normally in terms of estimated source location or direction is used to steer the main-beam of the beamformer to the direction of the signal source for audio reception. This automation releases the necessity for a human operator in audio acquisition and recording applications such as smart homes and robots.

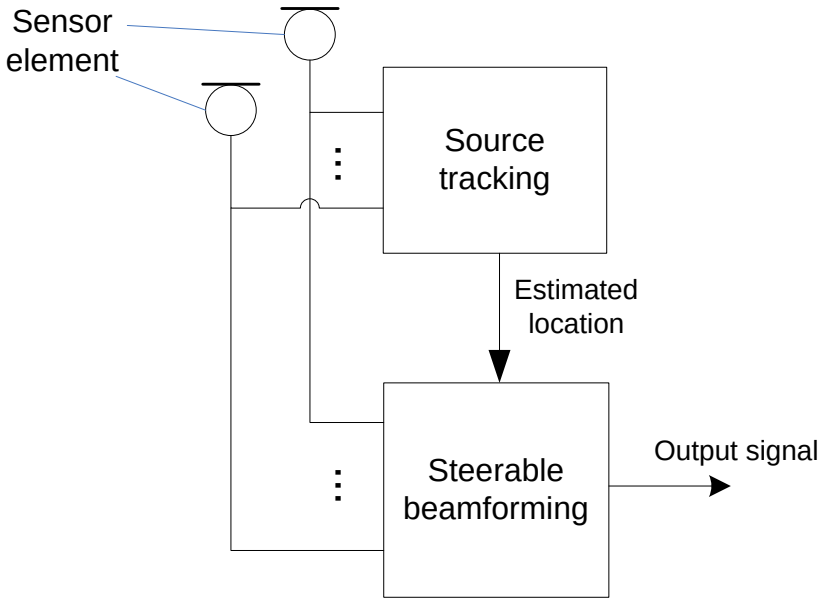

Figure 7.1: Tracking beamformer system.

2. **Adaptive steerable beamformer**

   The design of SBBFs presented in this thesis is non-adaptive, that is, data-independent. If the characteristics of the received signals are known, these information can be used to further improve the reception quality of the desired signal by means of adaptive or data-dependent SBBFs. Ultimately, this leads to steerable optimal broadband beamformers, where the beamformer weights are updated progressively to approach optimality and to track a moving source. One of the major problems in adaptive beamforming is target signal cancellation caused by reverberation or mismatches between the presumed and the actual models [110]. This is an interesting and challenging direction for further research.

3. **Steerable mixed nearfield-farfield azimuth-elevation beamformers**

   The design formulation for the steerable azimuth-elevation beamformers discussed in Chapter 6 applies to farfield sources only. It is an interesting direction for future research to extend the design formulation for nearfield sources following, for example, the works of [90, 91]. This may ultimately lead to the design formulation for mixed nearfield-farfield azimuth-elevation beamformers, which can be achieved by combining the individual design formulations for the nearfield and the farfield sources into a single design formulation.

4. **Selection of the optimal weighting function**

   Although the beamformer design formulations discussed in Chapters 3 to 5 have included a weighting function $V(\cdot)$, its detailed investigation has not been the focus of this thesis. Hence, thorough studies on its selection to further improve the beamformer designs can be an interesting extension to the work presented in this thesis.

5. **Investigation on the performance limits and trade-offs**

   In this thesis, robust beamformer design formulations have been proposed and have been shown to improve beamformers performance in the presence of errors and perturbations. This gives rise to questions, such as:

- How much errors can the design formulations sustain before failing completely?
- How will the design parameters affect the beamformer performances and trade-offs?

Comprehensive studies on the performance limits and trade-offs of the proposed design formulations (which lead to the answers for these questions) can be an interesting addition to this thesis.

6. **Optimum design of sensor array geometry**

   Section 3.2 has shown that the selection of array geometry plays an important role in the overall beamformer design. However, the main focus of this thesis is on the beamformer weights design and not on the array geometry design. Therefore, research on optimal sensor array geometry can be extended from this work in order to further improve the beamformer performances.

7. **Mathematical study on spherical harmonics beamforming blocks**

   In Chapter 6, a new spherical harmonics beamformer structure is proposed. Compared to the existing structure, the spherical decomposition block and filtering block in the proposed structure have been swapped, and yet, its performance does not differ significantly from the existing designs. This begs the question,

   - Are the filtering block, the spherical harmonics decomposition block and the beam steering block linear?

   Mathematical study on these blocks, both individually and corporately, can be an interesting future work.

References

[1] G. W. Elko, "Microphone array systems for hands-free telecommunication," *Speech Communication*, vol. 20, no. 3-4, pp. 229–240, Sep 1996.

[2] ——, "Future directions for microphone arrays," in *Microphone Arrays*, M. Brandstein and D. Ward, Eds. Springer-Verlag Berlin Heidelberg, New York, 2001, ch. 17, pp. 383–387.

[3] S. Nordholm, I. Claeson, and N. Grbic, "Optimal and adaptive microphone arrays for speech input in automobiles," in *Microphone Arrays*, M. Brandstein and D. Ward, Eds. Springer-Verlag Berlin Heidelberg, New York, 2001, ch. 14, pp. 307–330.

[4] N. Grbic and S. Nordholm, "Soft constrained subband beamforming for hands-free speech enhancement," in *Proc. IEEE Int. Conf. Acoust. Speech Signal Process. (ICASSP)*, vol. 1, Orlando, FL, 13-17 May 2002, pp. 885–888.

[5] J. Ryan and R. Goubran, "Application of near-field optimum microphone arrays to hands-free mobile telephony," *IEEE Trans. Veh. Technol.*, vol. 52, no. 2, pp. 390–400, Mar 2003.

[6] S. Boll, "Suppression of acoustic noise in speech using spectral subtraction," *IEEE Trans. Acoust., Speech., Signal Process.*, vol. 27, no. 2, pp. 113–120, Apr 1979.

[7] M. Berouti, R. Schwartz, and J. Makhoul, "Enhancement of speech corrupted by acoustic noise," in *Proc. IEEE Int. Conf. Acoust. Speech Signal Process. (ICASSP)*, vol. 4, Washington, USA, 2-4 Apr 1979, pp. 208–211.

[8] Y. Ephraim and D. Malah, "Speech enhancement using a minimum-mean square error short-time spectral amplitude estimator," *IEEE Trans. Acoust., Speech., Signal Process.*, vol. 32, no. 6, pp. 1109–1121, Dec 1984.

[9] Y. Ephraim and H. Van Trees, "A signal subspace approach for speech enhancement," *IEEE Trans. Speech Audio Process.*, vol. 3, no. 4, pp. 251–266, Jul 1995.

[10] J. Meyer and K. Simmer, "Multi-channel speech enhancement in a car environment using wiener filtering and spectral subtraction," in *Proc. IEEE Int. Conf. Acoust. Speech Signal Process. (ICASSP)*, vol. 2, Munich, Germany, 21-24 Apr 1997, pp. 1167–1170.

[11] R. Martin, "Noise power spectral density estimation based on optimal smoothing and minimum statistics," *IEEE Trans. Speech, Audio Process.*, vol. 9, no. 5, pp. 504–512, Jul 2001.

[12] I. Cohen and B. Berdugo, "Noise estimation by minima controlled recursive averaging for robust speech enhancement," *IEEE Signal Process. Lett.*, vol. 9, no. 1, pp. 12–15, Jan 2002.

[13] I. Cohen, "Noise spectrum estimation in adverse environments: improved minima controlled recursive averaging," *IEEE Trans. Speech, Audio Process.*, vol. 11, no. 5, pp. 466–475, Sep 2003.

[14] S. Y. Low, S. Nordholm, and R. Togneri, "Convolutive blind signal separation with post-processing," *IEEE Trans. Speech Audio Process.*, vol. 12, no. 5, pp. 539–548, Sep 2004.

[15] S. Y. Low and S. Nordholm, "A blind approach to joint noise and acoustic echo cancellation," in *Proc. IEEE Int. Conf. Acoust. Speech Signal Process. (ICASSP)*, vol. 3, Philadelphia, PA, 18-23 Mar 2005, pp. 69–72.

[16] H. H. Dam, S. Nordholm, S. Y. Low, and A. Cantoni, "Blind signal separation using steepest descent method," *IEEE Trans. Signal Process.*, vol. 55, no. 8, pp. 4198–4207, Aug 2007.

[17] B. D. Van Veen and K. M. Buckley, "Beamforming: a versatile approach to spatial filtering," *IEEE Signal Process. Mag.*, vol. 5, no. 2, pp. 4–24, Apr 1988.

[18] H. Krim and M. Viberg, "Two decades of array signal processing research: the parametric approach," *IEEE Signal Process. Mag.*, vol. 13, no. 4, pp. 67–94, Jul 1996.

[19] J. Huang, N. Ohnishi, and N. Sugie, "Sound localization in reverberant environment based on the model of the precedence effect," *IEEE Trans. Instrum. Meas.*, vol. 46, no. 4, pp. 842–846, Aug 1997.

[20] J. Benesty, "Adaptive eigenvalue decomposition algorithm for passive acoustic source localization," *J. Acoust. Soc. Am.*, vol. 107, no. 1, pp. 384–391, 2000.

[21] Y. Huang, J. Benesty, and G. Elko, "Passive acoustic source localization for video camera steering," in *Proc. IEEE Int. Conf. Acoust. Speech Signal Process. (ICASSP)*, vol. 2, Istanbul, Turkey, 5-9 Jun 2000, pp. 909–912.

[22] D. B. Ward, E. A. Lehmann, and R. C. Williamson, "Particle filtering algorithms for tracking an acoustic source in a reverberant environment," *IEEE Trans. Speech, Audio Process.*, vol. 11, no. 6, pp. 826–836, Nov 2003.

[23] E. A. Lehmann, "Particle filtering methods for acoustic source localisation and tracking," Ph.D. dissertation, Department of Telecommunications Engineering, The Australian National University, 2004.

[24] A. M. Johansson, "Acoustic sound source localisation and tracking in indoor environments," Ph.D. dissertation, School of Engineering, Blekinge Institute of Technology, 2008.

[25] M. F. Fallon and S. Godsill, "Acoustic source localization and tracking using track before detect," *IEEE Trans. Audio, Speech, Language Process.*, vol. 18, no. 6, pp. 1228–1242, Aug 2010.

[26] K. Kumatani, J. Mcdonough, and B. Raj, "Microphone array processing for distant speech recognition: From close-talking microphones to far-field sensors," *IEEE Signal Process. Mag.*, vol. 29, no. 6, pp. 127–140, Nov 2012.

[27] J. B. Allen and D. A. Berkley, "Image method for efficiently simulating small-room acoustics," *J. Acoust. Soc. Am.*, vol. 65, no. 4, pp. 943–950, 1979.

[28] H. Kuttruff, *Room acoustics*, 5th ed. Spon Press, 2009.

[29] P. A. Naylor and N. D. Gaubitch, Eds., *Speech dereverberation*. Springer-Verlag London, 2010.

[30] A. Manikas, A. Alexiou, and H. Karimi, "Comparison of the ultimate direction-finding capabilities of a number of planar array geometries," in *Proc. IEE Radar, Sonar and Navigation*, vol. 144, no. 6, Dec 1997, pp. 321–329.

[31] A. Sleiman and A. Manikas, "The impact of sensor positioning on the array manifold," *IEEE Trans. Antennas Propag.*, vol. 51, no. 9, pp. 2227–2237, Sep 2003.

[32] P. T. D. Abhayapala, "Modal analysis and synthesis of broadband nearfield beamforming arrays," Ph.D. dissertation, Telecommunications Engineering Group, The Australian National University, 2008.

[33] E. G. Williams, *Fourier Acoustics: Sound Radiation and Nearfield Acoustical Holography*. Academic Press, New York, 1999.

[34] R. A. Kennedy, T. D. Abhayapala, and D. B. Ward, "Broadband nearfield beamforming using a radial beampattern transformation," *IEEE Trans. Signal Process.*, vol. 46, no. 8, pp. 2147–2156, Aug 1998.

[35] Y. R. Zheng, R. A. Goubran, and M. El-Tanany, "Robust near-field adaptive beamforming with distance discrimination," *IEEE Trans. Speech, Audio Process.*, vol. 12, no. 5, pp. 478–488, Sep 2004.

[36] H. Chen, S. Wee, and Y. Zhu Liang, "Optimal design of nearfield wideband beamformers robust against errors in microphone array characteristics," *IEEE Trans. Circuits Syst. I, Reg. Papers*, vol. 54, no. 9, pp. 1950–1959, Sep 2007.

[37] P. Hacker and H. Schrank, "Range distance requirements for measuring low and ultralow sidelobe antenna patterns," *IEEE Trans. Antennas Propag.*, vol. 30, no. 5, pp. 956–966, Sep 1982.

[38] R. Hansen, "Measurement distance effects on low sidelobe patterns," *IEEE Trans. Antennas Propag.*, vol. 32, no. 6, pp. 591–594, Jun 1984.

[39] L. Ziomek, "Three necessary conditions for the validity of the fresnel phase approximation for the near-field beam pattern of an aperture," *IEEE J. Ocean. Eng.*, vol. 18, no. 1, pp. 73–75, Jan 1993.

[40] J. G. Ryan, "Criterion for the minimum source distance at which plane-wave beamforming can be applied," *J. Acoust. Soc. Am.*, vol. 104, no. 1, pp. 595–598, Jul 1998.

[41] R. Kennedy, D. Ward, and T. Abhayapala, "Nearfield beamforming using radial reciprocity," *IEEE Trans. Signal Process.*, vol. 47, no. 1, pp. 33–40, Jan 1999.

[42] J. Meyer and G. Elko, "A highly scalable spherical microphone array based on an orthonormal decomposition of the soundfield," in *Proc. IEEE Int. Conf. Acoust. Speech Signal Process. (ICASSP)*, vol. 2, Orlando, FL, 13-17 May 2002, pp. 1781–1784.

[43] T. D. Abhayapala and D. B. Ward, "Theory and design of high order sound field microphones using spherical microphone array," in *Proc. IEEE Int. Conf. Acoust. Speech Signal Process. (ICASSP)*, vol. 2, Orlando, FL, 13-17 May 2002, pp. 1949–1952.

[44] C. W. Farrow, "A continuously variable digital delay element," in *IEEE Int. Symp. Circuits Syst. (ISCAS)*, vol. 3, Espoo, Finland, 7-9 Jun 1988, pp. 2641–2645.

[45] M. Kajala and M. Hamalainen, "Filter-and-sum beamformer with adjustable filter characteristics," in *Proc. IEEE Int. Conf. Acoust. Speech Signal Process. (ICASSP)*, vol. 5, Salt Lake City, UT, 7-11 May 2001, pp. 2917–2920.

[46] C. C. Lai, S. Nordholm, and Y. H. Leung, "Design of robust steerable broadband beamformers with spiral arrays and the farrow filter structure," in *Proc. Int. Workshop Acoust., Echo, Noise Control*, Tel Aviv, Israel, 30 Aug-2 Sep 2010.

[47] L. C. Parra, "Steerable frequency-invariant beamforming for arbitrary arrays," *J. Acoustical Society America*, vol. 119, no. 6, pp. 3839–3847, 2006.

[48] S. M. Jaeger, W. C. Horne, and C. S. Allen, "Effect of surface treatment on array microphone self-noise," in *Proc. AIAA/CEAS Aeroacoustics Conference*, Lahaina, HI, 12-14 Jun 2000.

[49] D. Wetzel, F. Liu, B. Rosenberg, and L. Cattafesta, "Acoustic characteristics of a circulation control airfoil," in *Proc. AIAA/CEAS Aeroacoustics Conference*, Miami, FL, 11-13 May 2009.

[50] J. Hald and J. J. Christensen, "A class of optimal broadband phased array geometries designed for easy construction," in *Int. Congress and Exposition on Noise Control Eng.*, Dearborn, MI, 19-21 Aug 2002.

[51] S. C. Chan and H. H. Chen, "Uniform concentric circular arrays with frequency-invariant characteristics - theory, design, adaptive beamforming and doa estimation," *IEEE Trans. Signal Process.*, vol. 55, no. 1, pp. 165–177, Jan 2007.

[52] D. H. Johnson and D. E. Dudgeon, *Array Signal Processing - Concepts and techniques*. Prentice Hall, 1993.

[53] S. C. Pei and C. C. Tseng, "A new eigenfilter based on total least squares error criterion," *IEEE Trans. Circuits Syst. I, Fundam. Theory Appl.*, vol. 48, no. 6, pp. 699–709, Jun 2001.

[54] S. Doclo and M. Moonen, "Design of broadband beamformers robust against gain and phase errors in the microphone array characteristics," *IEEE Trans. Signal Process.*, vol. 51, no. 10, pp. 2511–2526, Oct 2003.

[55] I. Markovsky and S. Van Huffel, "Overview of total least-squares methods," *Signal Process.*, vol. 87, no. 10, pp. 2283–2302, Oct 2007.

[56] S. Doclo and M. Moonen, "Design of far-field and near-field broadband beamformers using eigenfilters," *Signal Process.*, vol. 83, no. 12, pp. 2641–2673, Dec 2003.

[57] S. V. Huffel and J. Vandewalle, *The total least squares problem: Computational aspects and analysis.* Society for Industrial and Applied Mathematics, 1991.

[58] A. H. Sayed, *Adaptive filters.* John Wiley & Sons, Inc, 2008.

[59] J. Bitzer and K. U. Simmer, "Superdirective microphone arrays," in *Microphone Arrays*, M. Brandstein and D. Ward, Eds. Springer-Verlag Berlin Heidelberg, New York, 2001, ch. 2, pp. 19–38.

[60] H. Cox, R. Zeskind, and T. Kooij, "Practical supergain," *IEEE Trans. Acoustics, Speech, Signal Process.*, vol. 34, no. 3, pp. 393–398, Jun 1986.

[61] S. Yan and Y. Ma, "Robust supergain beamforming for circular array via second-order cone programming," *Applied Acoustics*, vol. 66, no. 9, pp. 1018–1032, Sep 2005.

[62] S. Doclo and M. Moonen, "Superdirective beamforming robust against microphone mismatch," *IEEE Trans. Audio, Speech, Language Process.*, vol. 15, no. 2, pp. 617–631, Feb 2007.

[63] E. Mabande, A. Schad, and W. Kellermann, "Design of robust superdirective beamformers as a convex optimization problem," in *Proc. IEEE Int. Conf. Acoust. Speech Signal Process. (ICASSP)*, Taipei, Taiwan, 19-24 Apr 2009, pp. 77–80.

[64] J. Sachar, H. Silverman, and W. Patterson, "Microphone position and gain calibration for a large-aperture microphone array," *IEEE Trans. Speech, Audio Process.*, vol. 13, no. 1, pp. 42–52, Jan 2005.

[65] S. Doclo and M. Moonen, "Design of broadband beamformers robust against microphone position errors," in *Proc. Int. Workshop Acoust., Echo, Noise Control*, Kyoto, Japan, 8-11 Sep 2003, pp. 267–270.

[66] J. Ringelstein, A. Gershman, and J. Bohme, "Direction finding in random inhomogeneous media in the presence of multiplicative noise," *IEEE Signal Process. Lett.*, vol. 7, no. 10, pp. 269–272, Oct 2000.

[67] Y. J. Hong, C. C. Yeh, and D. R. Ucci, "The effect of a finite-distance signal source on a far-field steering Applebaum array-two dimensional array case," *IEEE Trans. Antennas Propag.*, vol. 36, no. 4, pp. 468–475, Apr 1988.

[68] R. Goossens, I. Bogaert, and H. Rogier, "Phase-mode processing for spherical antenna arrays with a finite number of antenna elements and including mutual coupling," *IEEE Trans. Antennas Propag.*, vol. 57, no. 12, pp. 3783–3790, Dec 2009.

[69] J. Meyer, "Microphone array for hearing aids taking into account the scattering of the head," in *IEEE Workshop Appl. Signal Process. Audio, Acoust.*, New Platz, NY, 21-24 Oct 2001, pp. 27–30.

[70] J. Goldberg and H. Messer, "Inherent limitations in the localization of a coherently scattered source," *IEEE Trans. Signal Process.*, vol. 46, no. 12, pp. 3441–3444, Dec 1998.

[71] O. Besson and P. Stoica, "Decoupled estimation of DOA and angular spread for a spatially distributed source," *IEEE Trans. Signal Process.*, vol. 48, no. 7, pp. 1872–1882, Jul 2000.

[72] D. Astely and B. Ottersten, "The effects of local scattering on direction of arrival estimation with MUSIC," *IEEE Trans. Signal Process.*, vol. 47, no. 12, pp. 3220–3234, Dec 1999.

[73] W. Liu, D. McLernon, and M. Ghogho, "Design of frequency invariant beamformer without temporal filtering," *IEEE Trans. Signal Process.*, vol. 57, no. 2, pp. 798–802, Feb 2009.

[74] E. N. Gilbert and S. P. Morgan, "Optimum design of directive antenna arrays subject to random deviations," *Bell Syst. Technol. J.*, vol. 34, pp. 637–663, May 1955.

[75] A. Elnashar, S. Elnoubi, and H. El-Mikati, "Further study on robust adaptive beamforming with optimum diagonal loading," *IEEE Trans. Antennas Propag.*, vol. 54, no. 12, pp. 3647–3658, Dec 2006.

[76] S. A. Vorobyov, A. B. Gershman, and L. Zhi-Quan, "Robust adaptive beamforming using worst-case performance optimization: a solution to the signal mismatch problem," *IEEE Trans. Signal. Process.*, vol. 51, no. 2, pp. 313–324, Feb 2003.

[77] S. Vorobyov, H. Chen, and A. Gershman, "On the relationship between robust minimum variance beamformers with probabilistic and worst-case distortionless response constraints," *IEEE Trans. Signal. Process.*, vol. 56, no. 11, pp. 5719–5724, Nov 2008.

[78] Z. L. Yu, W. Ser, M. H. Er, Z. Gu, and Y. Li, "Robust adaptive beamformers based on worst-case optimization and constraints on magnitude response," *IEEE Trans. Signal. Process.*, vol. 57, no. 7, pp. 2615–2628, Jul 2009.

[79] C. C. Lai, S. Nordholm, and Y. H. Leung, "Design of robust steerable broadband beamformers incorporating microphone gain and phase error characteristics," in *Proc. IEEE Int. Conf. Acoust. Speech Signal Process. (ICASSP)*, Prague, Czech Rep., 22-27 May 2011, pp. 101–104.

[80] D. Astely and B. Ottersten, "The effects of local scattering on direction of arrival estimation with music," *IEEE Trans. Signal Process.*, vol. 47, no. 12, pp. 3220–3234, 1999.

[81] D. B. Ward and G. W. Elko, "Mixed nearfield/farfield beamforming: a new technique for speech acquisition in a reverberant environment," in *Proc.*

IEEE Workshop Appl. Signal Process. Audio, Acoust., New Paltz, NY, 19-22 Oct 1997, pp. 4–7.

[82] D. Ward, Z. Ding, and R. Kennedy, "Broadband doa estimation using frequency invariant beamforming," *IEEE Trans. Signal Process.*, vol. 46, no. 5, pp. 1463–1469, May 1998.

[83] T.-B. Deng and W.-S. Lu, "Weighted least-squares method for designing variable fractional delay 2-D fir digital filters," *IEEE Trans. Circuits Syst. II, Analog Digit. Signal Process.*, vol. 47, no. 2, pp. 114–124, Feb 2000.

[84] J.-J. Shyu, S.-C. Pei, and Y.-D. Huang, "Two-dimensional Farrow structure and the design of variable fractional-delay 2-D fir digital filters," *IEEE Trans. Circuits Syst. I, Reg. Papers*, vol. 56, no. 2, pp. 395–404, Feb 2009.

[85] B. K. Lau and Y. H. Leung, "A Dolph-Chebyshev approach to the synthesis of array patterns for uniform circular arrays," in *IEEE Int. Symp. Circuits Syst. (ISCAS)*, vol. 1, Geneva, Switzerland, May 28-31 2000, pp. 124–127.

[86] B. Rafaely, "Phase-mode versus delay-and-sum spherical microphone array processing," *IEEE Signal Process. Letters*, vol. 12, no. 10, pp. 713–716, Oct 2005.

[87] ——, "Spherical microphone array with multiple nulls for analysis of directional room impulse responses," in *Proc. IEEE Int. Conf. Acoust. Speech Signal Process. (ICASSP)*, Las Vegas, NV, 31 Mar-4 Apr 2008, pp. 281–284.

[88] H. Sun, S. Yan, and U. Peter Svensson, "Robust spherical microphone array beamforming with multi-beam-multi-null steering, and sidelobe control," in *Proc. IEEE Workshop Appl. Signal Process. Audio, Acoust.*, New Paltz, NY, 18-21 Oct 2009, pp. 113–116.

[89] A. Koretz and B. Rafaely, "Dolph-Chebyshev beampattern design for spherical arrays," *IEEE Trans. Signal Process.*, vol. 57, no. 6, pp. 2417–2420, Jun 2009.

[90] J. Meyer and G. W. Elko, "Position independent close-talking microphone," *Signal Process.*, vol. 86, no. 6, pp. 1254–1259, Jun 2006.

[91] E. Fisher and B. Rafaely, "Near-field spherical microphone array processing with radial filtering," *IEEE Trans. Audio, Speech, Language Process.*, vol. 19, no. 2, pp. 256–265, Feb 2011.

[92] J. Meyer and G. Elko, "Spherical microphone arrays for 3d sound recording," in *Audio Signal Processing for Next-Generation Multimedia Communication Systems*, Y. Huang and J. Benesty, Eds. Springer US, 2004, pp. 67–89.

[93] S. Yan, H. Sun, U. Svensson, X. Ma, and J. Hovem, "Optimal modal beamforming for spherical microphone arrays," *IEEE Trans. Audio, Speech, Language Process.*, vol. 19, no. 2, pp. 361–371, Feb 2011.

[94] Z. Li and R. Duraiswami, "Flexible and optimal design of spherical microphone arrays for beamforming," *IEEE Trans. Audio, Speech, Language Process.*, vol. 15, no. 2, pp. 702–714, Feb 2007.

[95] T. R. Chandrupatla and A. D. Belegundu, *Introduction to Finite Elements in Engineering*, 3rd ed. Prentice Hall, 2002.

[96] B. Rafaely, B. Weiss, and E. Bachmat, "Spatial aliasing in spherical microphone arrays," *IEEE Trans. Signal Process.*, vol. 55, no. 3, pp. 1003–1010, Mar 2007.

[97] S. Yan, H. Sun, X. Ma, U. Svensson, and C. Hou, "Time-domain implementation of broadband beamformer in spherical harmonics domain," *IEEE Trans. Audio, Speech, Language Process.*, vol. 19, no. 5, pp. 1221–1230, Jul 2011.

[98] B. Rafaely, "Analysis and design of spherical microphone arrays," *IEEE Trans. Speech, Audio Process.*, vol. 13, no. 1, pp. 135–143, Jan 2005.

[99] J. R. Driscoll and D. M. Healy, "Computing fourier transforms and convolutions on the 2-sphere," *Advances in Applied Mathematics*, vol. 15, no. 2, pp. 202–250, Jun 1994.

[100] G. Arfken and H. Weber, *Mathematical Methods for Physicists*, 5th ed. San Diego, Academic Press, 2001.

[101] M. J. Mohlenkamp, "A fast transform for spherical harmonics," *Journal of Fourier Analysis and Applications*, vol. 5, no. 2-3, pp. 159–184, Mar 1999.

[102] J. Fliege and U. Maier, "The distribution of points on the sphere and corresponding cubature formulae," *IMA Journal of Numerical Analysis*, vol. 19, no. 2, pp. 317–334, Apr 1999.

[103] A. Katanforoush and M. Shahshahani, "Distributing points on the sphere, I," *Experimental Mathematics*, vol. 12, no. 2, pp. 199–209, 2003.

[104] M. Atiyah and P. Sutcliffe, "Polyhedra in physics, chemistry and geometry," *Milan Journal of Mathematics*, vol. 71, no. 1, pp. 33–58, May 2003.

[105] R. H. Hardin and N. J. A. Sloane, "McLaren's improved snub cube and other new spherical designs in three dimensions," *ArXiv Mathematics*, Jul 2002.

[106] J. F. Sturm, "Using sedumi 1.02, a matlab toolbox for optimization over symmetric cones," *Optimization Methods and Software*, vol. 11, no. 1-4, pp. 625–653, 1999.

[107] W. Feller, *An Introduction to Probability Theory and Its Applications*, ser. 3rd ed. John Wiley & Sons, Inc, New York, 1971, vol. 2.

[108] E. A. Lehmann and A. M. Johansson, "Particle filter with integrated voice activity detection for acoustic source tracking," *EURASIP Journal on Advances in Signal Processing*, vol. 2007, no. 1, pp. 28–38, Jan 2007.

[109] S. Timofeev, A. R. S. Bahai, and P. Varaiya, "Adaptive acoustic beamformer with source tracking capabilities," *IEEE Trans. Signal Process.*, vol. 56, no. 7, pp. 2812–2820, Jul 2008.

[110] O. Hoshuyama and A. Sugiyama, "Robust adaptive baemforming," in *Microphone Arrays*, M. Brandstein and D. Ward, Eds. Springer-Verlag Berlin Heidelberg, New York, 2001, ch. 5, pp. 87–110.

[111] D. Astely, B. Ottersten, and A. Swindlehurst, "A generalized array manifold model for local scattering in wireless communications," in *Proc. IEEE Int. Conf. Acoust. Speech Signal Process. (ICASSP)*, vol. 5, Munich, Germany, 21-24 Apr 1997, pp. 4021–4024.